Extratropical Storm Tracks and the Mean State of the Atmosphere

by

Charles Garrison Gertler

A.B. Harvard College (2013)
M.Phil. University of Cambridge (2014)

Submitted to the Department of Earth, Atmospheric, and Planetary Sciences
in partial fulfillment of the requirements for the degree of

Doctor of Philosophy

at the

MASSACHUSETTS INSTITUTE OF TECHNOLOGY

September 2020

Author .....
Department of Earth, Atmospheric, and Planetary Sciences
August 31, 2020

Certified by .....
Ronald G. Prinn
TEPCO Professor of Atmospheric Science
Thesis Supervisor

Certified by .....
Paul A. O'Gorman
Professor of Atmospheric Science
Thesis Supervisor

Accepted by .....
Robert van der Hilst
Schlumberger Professor of Earth Sciences
Head of Department of Earth, Atmospheric, and Planetary Sciences

Extratropical Storm Tracks and the Mean State of the Atmosphere

by

Charles Garrison Gertler

Submitted to the Department of Earth, Atmospheric, and Planetary Sciences
on August 31, 2020, in partial fulfillment of the
requirements for the degree of
Doctor of Philosophy

Abstract

The exact impacts of changes in the mean state of the atmosphere on the high-frequency phenomena that form the extratropical atmospheric circulation are uncertain. The extratropical storm tracks, regions of frequent extratropical cyclones, dominate weather in the extratropics, affecting the lives and livelihoods of billions of people. The results presented in this thesis connect changes in the mean state of the atmosphere to changes in the extratropical storm tracks.

The Northern Hemisphere summer extratropical storm track has weakened in observations over the satellite era, while evidence indicates convective precipitation in the extratropics has concurrently increased. Using the concept of mean available potential energy (MAPE) partitioned into nonconvective and convective components, the second chapter of this thesis demonstrates that the changes in storm track strength and convection are consistent with changes in the temperature and humidity structure of the atmosphere. Further, experiments with idealized atmospheres indicate how characteristic changes in surface temperatures over this period lead to diverging changes in the energy available to extratropical cyclones and their associated convection.

In the third chapter of this thesis, the storm track strength is examined in solar geoengineering scenarios using results from climate models. The Northern Hemisphere extratropical storm track weakens in response to increased CO_2 by similar magnitudes regardless of whether solar geoengineering is used. In the Southern Hemisphere, the storm track strengthens in global warming scenarios, but weakens with solar geoengineering. Storm track intensity changes are shown to be consistent with changes in the structure of temperature and humidity using MAPE.

In the fourth chapter of this thesis, a new method to calculate MAPE is introduced and used to perform the first exact MAPE calculations in a three-dimensional domain. Further, an eddy-size restriction on the MAPE calculation is developed and introduced, which provides a measure of available energy that could be accessed locally by an extratropical cyclone. This approach is also used to identify the thermodynamic potential for ascent on the eddy lengthscale, which is shown to relate

strongly to the frequency of warm conveyor belts (WCBs), dynamic components of extratropical cyclones with large impacts on weather.

Thesis Supervisor: Ronald G. Prinn
Title: TEPCO Professor of Atmospheric Science

Thesis Supervisor: Paul A. O'Gorman
Title: Professor of Atmospheric Science

Acknowledgments

I am deeply indebted to Ron Prinn for accepting me as his final graduate student, for not only tolerating but encouraging my wandering eye as I chose a research focus, for always putting my development and experience above bureaucratic requirements, for supporting my ideas, and for creating the platform of exploration that has underpinned these formative years. I will miss our conversations about research directions, science, and the state of the world around his big conference table overlooking the Charles River. I owe another large debt of gratitude to my second advisor, Paul O'Gorman, for his close scientific collaboration and guidance over the last five years, always dedicated and generous. I have learned many things from Paul, beyond the analysis of climate data and atmospheric physics: a deep faith that the physical world is self-consistent, that one can make sense of complex problems by simply thinking a little longer and harder, and, perhaps most importantly, I've learned by example how to give straightforward feedback while still being kind.

I am also deeply appreciative of the mentorship and guidance of the other two members of my thesis committee. Thank you to David McGee for nurturing my interest in paleoclimate and staying on to mentor my thesis, and for consistently asking the most insightful questions about my research. Many thanks to Stephan Pfahl for sharing data and expertise on warm conveyor belts, and for so generously hosting me in Berlin during its best season (summer). I have benefitted immeasurably from the many mentors, advisors, and collaborators that my time in Cambridge has permitted me before and during my PhD. Sheila Jasanoff, Jerry Mitrovica, Peter Huybers, Mike McElroy, Arnico Panday, and Alicia Harley helped send me on this journey, and have all contributed along the way. I have benefitted from interactions with every faculty member in PAOC in some way or another, for which I am deeply grateful. Finally, I owe a large debt of gratitude to my 8^{th} grade Earth Science teacher, John Stasik, for inspiring this path.

Deep thanks are owed as well to the EAPS staff, for support and friendship. To my office mates in 54-1320: thank you for keeping our view a secret and making life

in EAPS as fun as it was. Thanks in particular to Michael McClellan for our special bond as the final Prinn Group members, and to Martin Wolf for our unshakable pairing from day one. I am deeply grateful to the rest of my cohort and all the students in EAPS, with whom many conversations have improved my scientific and personal life. I am particularly indebted to the students from other countries and underrepresented minorities who braved obstacles in the culture of science and a hostile national environment over the last 5 years to be in this country and its scientific community; you have immeasurably enriched the lives of those around you, including my own.

I acknowledge financial support by the Industry and Foundation sponsors of the MIT Joint Program on the Science and Policy of Global Change, NASA grant NNX16AC98G to MIT, and the National Science Foundation Graduate Research Fellowship Program under NSF Grant 1122374. I am also grateful for certain institutions that have improved my life during the past five years: Southwest Airlines, Clover, the Koch Cafe, HMart, Woodberry Kitchen, MIT Recreation, and the Muddy Charles.

No words of thanks would ever be enough to my friends and family. To my close friends, thank you for supporting me through this process, in ways small and large. To my Schwiegerfamilie, thank you for your constant faith in my abilities (not often deserved) and frequent peaceful refuge in Berlin. To my parents: I took on this challenge because of the values you instilled in me, and I was able to complete it because of your love and support. To Chessin, William, and Henny: thank you for keeping me sane, happy, and focused. Finally, to my niece, Jhie: I do this work for you, so that you may inherit a just and healthy world.

Thanks above all to Caroline, my most ardent cheerleader and most reliable proofreader. The last five years have seen us both become scientists and frequent fliers, and I am ecstatic for us to lose the second title and keep the first. You inspired me every day of this process; it truly would not have been possible without you.

Contents

List of Figures

List of Tables

Chapter 1

Introduction

In Earth's extratropics (regions poleward of roughly 30 degrees latitude), much of what we think of as weather is dominated by large storm systems known as extratropical cyclones [11]. When a cold front moves through over a park in Berlin, or a farm in Kentucky, an extratropical cyclone is to blame. When a Nor'easter whips up Buzzards Bay and enough snow falls in Cambridge to make a snowman, an extratropical cyclone is to thank. Hot summer days in Saskatoon and Baltimore, winter storms in Corsica and Beijing, the swells that Scott and Shackleton braved in the Southern Ocean, Odysseus's wine-dark seas - they are all likely manifestations of extratropical cyclones, the results of a specific hydrodynamic instability prevalent in the Earth's middle latitudes. This is not to say that only extratropical cyclones cause weather – tropical cyclones, or hurricanes, form in the tropics due to a different instability and often travel further polewards, and while convection, or thunderstorm activity, is often associated with extratropical cyclones, it also occurs in isolated air mass thunderstorms or in mesoscale convective systems. Furthermore, anti-cyclones can also influence extreme weather. Still, for billions of people, on most days, when the weather outside changes it is because an extratropical cyclone has changed position or intensity.

It is natural to ask how extratropical cyclones will be affected as our planet continues to warm due to anthropogenic greenhouse gas emissions. The question itself is interesting and important, because extratropical storm tracks, the regions of most

frequent extratropical cyclones, play a large role in key functions of the climate system by, for example, transporting energy poleward to maintain a habitable climate and driving ocean circulation and carbon uptake [71]. Moreover, an understanding of the ways in which extratropical storm tracks change in a warming climate should enhance our understanding of how the associated phenomena – local extremes in winds, precipitation, and temperature – might change as well, affecting human lives and livelihood. Significant work has been done to date to address this question, but in short, climate change imposes multiple influences of varying magnitude and direction on the intensity, frequency, and position of extratropical storm tracks [71]. This thesis attempts to make further progress on this question by turning to perhaps a more general question: how to connect the mean state of the climate to the high frequency phenomena, like extratropical cyclones and their associated convection, that form the extratropical atmospheric circulation.

1.1 Extratropical Storm Tracks and their Response to Climate Changes

Extratropical cyclones are large-scale systems, typically defined around a local minimum in sea level pressure, that dominate the extratropical atmospheric circulation. They result from baroclinic instability, a hydrodynamic instability that occurs in rotating stratified fluids [88]. Baroclinic instability is common in extratropical regions due to the horizontal temperature gradients maintained by differential solar radiation and planetary rotation, and is also affected by static stability. Extratropical storm tracks act to reduce temperature gradients through their generation. However, the extratropical storm tracks also act to help maintain the very baroclinicity that causes them by inducing diabatic heating and ocean circulations that enhance temperature gradients [28].

Precipitation, wind, and temperature extremes have all been shown to be significantly associated with extratropical cyclones [71]. The majority of precipitation

extremes in the extratropics occur in extratropical cyclones, or their associated fronts and warm conveyor belts (WCBs) [55, 9]. WCBs, which are strongly ascending air streams that originate in the atmospheric boundary layer in the warm sector of extratropical cyclones, play a large role in cloud formation and are responsible for a large portion of extreme precipitation events over the ocean [7]. Some of the strongest near-surface winds are also associated with WCBs [10]. Temperature extremes are often the result of advection by strong cyclones, especially cold extremes in winter, and the vast majority of warm temperature extremes over both land and ocean are related to atmospheric blocking, a persistent configuration of extratropical cyclones and anticyclones [56].

Experiments with earth system models of varying complexity have been the primary tool with which to assess the impact of thermodynamic changes in climate on storm track dynamics, and demonstrate a range of competing influences [71]. For example, idealized simulations with increased CO_2 indicate a competition between arctic and tropical warming at different levels, affecting temperature gradients and the location and intensity of baroclinic regions in different ways [8]. Atmospheric general circulation models indicate that increased CO_2 leads to amplified summer stationary eddies through direct radiative forcing which shift the Pacific storm track poleward. However, the indirect effect of warming due to increased CO_2 serves to weaken the stationary eddies and shift the storm track equatorward [72]. Given the various competing influences on the storm tracks, their fate in a warming climate, or climate changed in any way, is far from clear.

Indeed, the potential future response of extratropical cyclones is uncertain, as demonstrated by complex modeling of the earth system. Projections of extratropical cyclone activity from the Coupled Model Intercomparison Project 3 (CMIP3) for a global warming scenario demonstrate overall stronger Southern Hemisphere storm tracks by the end of the century in the ensemble mean, and generally weaker Northern Hemisphere storm tracks, with significant intermodel variation in both hemispheres [48]. Projections of extratropical cyclone activity from the Coupled Model Intercomparison Project 5 (CMIP5) for a global warming scenario similarly demonstrate

weakening of the ensemble mean for Northern Hemisphere summer with large inter-model variation [12]. These projections can provide useful bulk metrics for storm track strength, but often require more involved analysis to comment on specific effects, such as discerning whether changes in cyclone frequency or intensity are leading to changes in storm track strength, or how associated components of extratropical cyclones, like WCBs, may be affected.

Even where the storm track response to a specific climate change is consistent, its physical reasons are not always clear. Storm tracks consistently weaken in both hemispheres in modeling experiments of solar geoengineering with stratospheric aerosol injection, the policy proposal to inject aerosols or their precursors into the stratosphere in order to reflect incoming shortwave radiation from the sun to offset longwave radiative forcing due to increasing greenhouse gas concentrations [76]. Various hypotheses for the drivers of this weakening have been proposed, such as stratospheric heating from aerosols, changes in moisture, and changes in radiative cooling in extratropical cyclones due to increased CO_2 concentrations [76]. Stratospheric heating was ruled out using idealized experiments, and Chapter 3 of this thesis proposes and supports a new explanation.

An accidental experiment has already been performed to help assess the influence of a warming climate on the extratropical circulation in our own atmosphere: anthropogenic global warming due to increased greenhouse gas concentrations. In the Northern Hemisphere summer, the only season and region in which the signal-to-noise ratio is strong enough to detect a trend in the observational record, the number of strong cyclones decreased at roughly 4% per decade since 1979, when reliable satellite observations of the atmosphere began [12]. This decrease falls at the extreme end of decreases among CMIP5 simulations. Decreases were also observed in the local 24-hour variance of sea level pressure, a useful proxy for extratropical cyclone activity, as well as eddy kinetic energy (EKE), the kinetic energy of wind fields filtered to the characteristic timescales of extratropical cyclones [12, 15]. However, not all reanalyses agree on the sign and magnitude of these changes. Furthermore, while these changes are consistent in sign with decreasing meridional temperature gradi-

ents in the atmosphere, the changes in meridional temperature gradient have not been shown to explain the magnitude of the changes in storm track intensity, and changes in moisture and static stability also affect the strength of the storm track.

The same accidental experiment provides us with information about how convection at the midlatitudes might change in a warming climate, as well. Station observations in extratropical regions indicate large increases in the fraction of precipitation that is convective in nature since the 1960s [93]. While there is evidence that convective available potential energy (CAPE) has increased in some regions as the climate has warmed [61], CAPE is also a high-frequency quantity, calculated from instantaneous vertical profiles of temperature and humidity, and is thus not directly related to the mean temperature and moisture. Unlike the tropics, where theory exists to connect observations of increasing convective potential and convective activity with a warming mean climate [77, 78, 70], the link between mean climate and convective activity in the extratropics is less clear.

Unifying the physical bases of the these observed changes to the extratropical circulation and linking them to changes in the mean state of the climate is a major objective of this thesis, in order to better understand changes that have already occurred in our climate as well as potential changes that may come. By developing a stronger understanding of how the mean state of the climate affects shorter-timescale phenomena, like extratropical cyclones and associated convection, the overall intent of this work is to reinforce the scientific frameworks that connect climate and weather, so that we may more fully understand changes to our planet that take place on longer timescales through the lens of our daily experience of our environment.

1.2 Mean Available Potential Energy

Throughout this thesis, I use the concept of mean available potential energy (MAPE) to accomplish these goals. In essence, MAPE represents the magnitude of the reservoir of energy from which large-scale circulations, like extratropical cyclones, can draw. Like a traditional reservoir of water, MAPE is extracted as it is replenished, and

the amount of MAPE that is extracted often changes in tandem with changes in the overall MAPE. The mean state of the atmosphere has a complex structure, with low entropy fluid sometimes occurring at higher levels than comparatively higher entropy fluid in other regions. Just as water poured over oil sinks to the bottom of a glass, gravity and buoyancy forces in the atmosphere strive towards a natural state where the heaviest fluid (or lowest entropy for the atmosphere) is on the bottom, and the lightest on the top, releasing kinetic energy in the process.

First introduced by Lorenz [38], the concept of MAPE rests on the observation that in a closed system, only total potential energy (the sum of potential and internal energy) is a source for kinetic energy, and thus, the maximum amount of kinetic energy that can be extracted from the system is the maximum amount of total potential energy releasable under adiabatic and reversible redistribution of mass. Not all total potential energy is available because of mass conservation in the closed system. Therefore, there exists some theoretical minimum potential energy state, referred to here as the reference state, and the MAPE is the difference in total potential energy between the original state and the reference state. Determining the reference state forms the bulk of the MAPE calculation. With the introduction of moisture [39], the calculation of the reference state became more difficult, as two variables are conserved, water content and entropy, and the latent heat of phase changes of water must be accounted for. Only recently have fast, exact methods to calculate MAPE been developed [79, 80], and I introduce a new method in Chapter 4 of this thesis.

MAPE has been shown to scale with the strength of the storm tracks over a suite of forced climate changes, in climate models of varying complexity and in reanalysis datasets [68, 50, 48, 49]. This empirical relation is useful, as it is able to capture the competing effects of horizontal temperature gradients, moisture, and static stability on the energy available for extratropical cyclones. This makes MAPE a valuable tool in the pursuit of understanding the response of extratropical circulation to climate changes. Indeed, intermodel differences in MAPE were shown to account for the intermodel differences in storm track strength among CMIP3 models in response to a global warming scenario [48].

Dynamic restrictions on MAPE are a further technique to gain insight into extratropical circulation. A nonconvective condition, introduced in [48], restricts moist convective motion in the mass rearrangement, allowing for the separation between non-convective and convective ascent in the release of available potential energy. An eddy-size restriction, introduced in an ocean context in [80] and developed for the atmosphere in Chapter 4 of this thesis, restricts mass rearrangement to within the characteristic length scale of eddies, thereby defining a local MAPE quantity. By examining the potential motion of air from the mean state to the reference state under different conditions, the thermodynamic potential for certain atmospheric motion is illuminated. This thesis is thus able to identify simple thermodynamic drivers of complex dynamics, in pursuit of understanding how the mean climate state and changes therein affect atmospheric circulation in the extratropics.

1.3 Thesis Structure

In each of the three main chapters of this thesis, I set out to answer major questions about how and why changes in the climate are reflected in the high frequency weather events comprising extratropical circulation. The reader may find a brief roadmap of the main findings of the thesis useful, which I describe here.

Chapter 2 asks and answers how the observed weakening of the extratropical storm tracks and a strengthening of extratropical convection in Northern Hemisphere summer are connected to the changes in the mean climate. Chapter 3 builds on Chapter 2 by considering the case of a potential intervention to global warming: solar geoengineering. In Chapter 3, I demonstrate that solar geoengineering would do little to avert changes in storm track intensity in the Northern Hemisphere, and has the potential to overcompensate in the Southern Hemisphere. Despite small changes in temperature, the changes in storm track strength are shown to be the result of changes to the mean structure of temperature and humidity, and highlight the differences between a baseline climate and a solar-geoengineered climate. Finally, in Chapter 4 of this thesis I make algorithmic progress in the calculation of MAPE and perform the first exact

three-dimensional calculation of MAPE and the first three-dimensional calculation of moist MAPE for the climatological atmosphere. This approach is then used to show thermodynamic potential for specific dynamic components of the extratropical circulation like convection and WCBs. Chapter 5 offers a summary of the key results from the work presented, and discusses various potential avenues for further research.

Chapter 2

Changing Available Energy for Extratropical Cyclones and Associated Convection in Northern Hemisphere Summer

This chapter has been adapted from a previously published paper [22]: C. G. Gertler and P. A. O'Gorman. Changing available energy for extratropical cyclones and associated convection in northern hemisphere summer. Proceedings of the National Academy of Sciences, 116(10):4105-4110, 2019.

Abstract:

The circulation of the Northern Hemisphere extratropical troposphere has changed over recent decades, with marked decreases in extratropical cyclone activity and eddy kinetic energy (EKE) in summer and increases in the fraction of precipitation that is convective in all seasons. Decreasing EKE in summer is partly explained by a weakening meridional temperature gradient, but changes in vertical temperature gradients and increasing moisture also affect the mean available potential energy (MAPE), which is the energetic reservoir from which extratropical cyclones draw. Further-

more, the relation of changes in mean thermal structure and moisture to changes in convection associated with extratropical cyclones is poorly understood. Here trends in MAPE for the Northern extratropics in summer are calculated over the years 1979-2017, and MAPE is decomposed into both convective and nonconvective components. Nonconvective MAPE decreased over this period, consistent with decreases in EKE and extratropical cyclone activity, but convective MAPE increased, implying an increase in the energy available to convection. Calculations with idealized atmospheres indicate that nonconvective and convective MAPE both increase with increasing mean surface temperature and decrease with decreasing meridional surface temperature gradient, but convective MAPE is relatively more sensitive to the increase in mean surface temperature. These results connect changes in the atmospheric mean state with changes in both large-scale and convective circulations, and they suggest that extratropical cyclones can weaken even as their associated convection becomes more energetic.

2.1 Introduction

Distinct patterns of change have emerged in the thermal structure and moisture content of the Northern Hemisphere extratropical troposphere [69, 43, 74, 16], as seen from homogenized radiosonde data (see Section 2.6) for the summer season in Figure 2-1. Notably, the meridional temperature gradient has weakened in the lower- and middle-troposphere (Figure 2-1a), and the troposphere has experienced a general moistening (Figure 2-1b). The weakening of the meridional temperature gradient is thought to contribute to the observed weakening of EKE and cyclone activity levels [15, 12], with implications for regional climate and air quality [37]. However, not all reanalysis products agree on the specific structure or intensity of temperature change (Appendix, Section 2.7, Figure 2-6). Furthermore, eddy behavior is also affected by changes in moisture content and static stability. For example, amplified low-level warming (Figure 2-1a), which is more clearly evident in reanalysis trends that extend to the surface (Appendix, Section 2.7, Figure 2-7a), implies decreased static stability

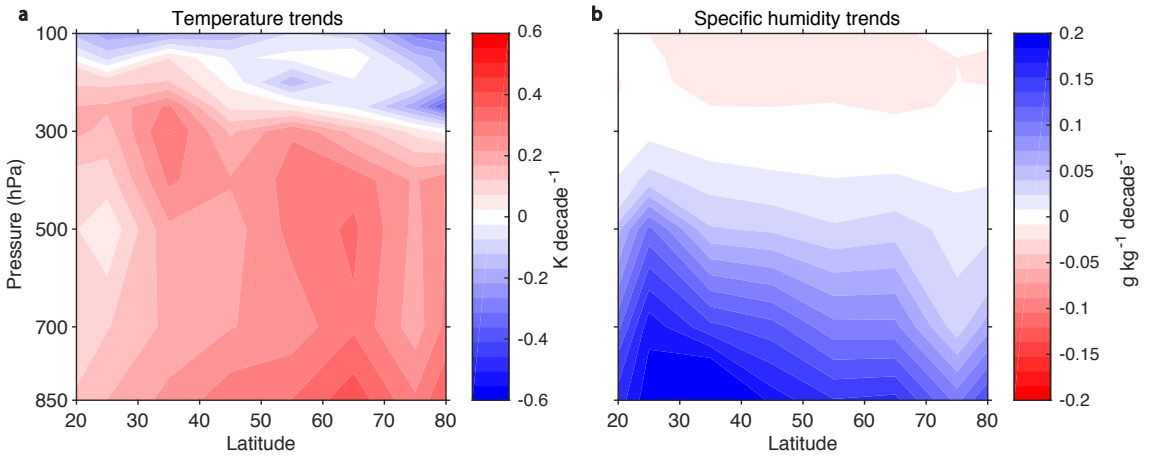

Figure 2-1: Observed changes in summer (JJA) temperature and moisture of the Northern extratropics. (a) Median JJA temperature trend in 10-degree latitude bands from the IUKv2 radiosonde dataset [74] (1979-2015), and (b) median JJA specific humidity trend in 10-degree latitude bands from the homoRS92 radiosonde dataset [16] (1979-2010). See Section 2.6 for datasets and calculation details.

in the lower troposphere, which together with increasing specific humidity (Figure 2-1b) would tend to increase the growth rates of eddies, opposing the weakening effect from the meridional temperature gradients. Projections of 21^{st} century climate change with coupled climate models also show a decrease in EKE in the Northern Hemisphere in summer that has been linked to weakening lower-tropospheric meridional temperature gradients [26] and increases in extratropical static stability that occurs in the projections in this season [48]. The changes in mean thermal structure and moisture could also cause changes in the energy available to convection; large increases in the convective fraction of precipitation have been observed for all seasons over Eurasia [93], and there is some evidence for increases in convective available potential energy (CAPE) as the climate has warmed [61]. However, CAPE is calculated from instantaneous vertical profiles of temperature and humidity and cannot be directly related to changes in mean temperature and moisture in the extratropics.

Mean available potential energy (MAPE) provides a useful framework with which to connect the mean thermal structure (including both meridional temperature gradients and static stability) and moisture content of the extratropical atmosphere to EKE and, as discussed below, to available energy for convection. MAPE is defined

as the difference in enthalpy between an atmosphere's mean state and the minimum-enthalpy state possible from reversible, adiabatic parcel rearrangements [38]. MAPE may be calculated neglecting latent heating (dry MAPE) [38] or taking it into account (moist MAPE) [40, 79]. EKE scales linearly with dry and moist MAPE in extratropical, baroclinic environments in a wide range of idealized climate model experiments [68, 50, 49]. A recent study [94] that imposed isolated thermal forcings at different latitudes and levels found that the scaling of EKE with MAPE can break down in some cases, but that it generally performs better than considering the change in meridional temperature gradient or static stability alone. Importantly, EKE also scales linearly with MAPE over the seasonal cycle in the extratropics in both hemispheres based on reanalysis data, and under climate change in coupled model projections, including for intermodel differences [48].

Here, changes in moist MAPE over recent decades are calculated and the results are used to better understand observed changes in the circulation. Some recent studies suggest an increasing trend in global eddy energy, but these changes are dominated by the Southern Hemisphere and their magnitude is dataset-dependent [52, 32]. The focus is on the Northern Hemisphere extratropics in June-July-August (JJA), given the clear reported trends in cyclonic activity [15, 12] and convective precipitation fraction [93] in that season and hemisphere. Using moist rather than dry MAPE allows for consideration of the role of latent heating and the implications for moist convection.

2.2 Mean Available Potential Energy (MAPE)

Zonal- and seasonal-mean temperatures and humidities from the ERA-Interim Reanalysis [17] are used to calculate MAPE for JJA and the latitude band 20-80N over the years 1979-2017. ERA-Interim provides complete spatial and temporal coverage, and trends in mean temperature from ERA-Interim are similar to those from homogenized radiosonde data when subsampled to that data (compare Figure 2-1a and Appendix, Section 2.7, Figure 2-8a). However, the subsampled humidity trends do

not agree well with a homogenized radiosonde humidity data (compare Figure 2-1b and Figure 2-9b), and this issue with ERA-Interim relative humidity trends could partly relate to the use of unhomogenized radiosonde humidities as input to the reanalysis [16]. To avoid this bias in humidity trends, relative humidity is held constant in time using its climatological values from ERA-Interim. This gives mean specific humidity trends that are more consistent with the radiosonde data (Figure 2-8b; see Section 2.6 for details).

The air-parcel rearrangement in the calculation of moist MAPE for JJA is illustrated in Figure 2-2a based on climatological temperatures and humidities. The general pattern is of rising air originating at lower latitudes and sinking air originating at higher latitudes, corresponding to large-scale slantwise motion in baroclinic eddies in the atmosphere. In addition, there is a substantial air mass (highlighted in blue in Figure 2-2a) that moves from the boundary layer to the upper troposphere and which is bounded by a discontinuity in the mapping of the parcel rearrangement. The ascent of this air mass to the upper troposphere results in a vertical reordering of air parcels originating at low latitudes which is interpreted as corresponding to deep convection in the atmosphere. While the air mass originates at low latitudes, its ascent can occur in the midlatitudes, since extratropical cyclones advect air poleward before deep ascent occurs [42, 59]. The parcel rearrangement for winter (Figure 2-10a) also shows deep ascent but with a weaker signature of convection and no discontinuity, consistent with deep ascent in winter predominantly occurring as slow ascent in warm conveyor belts rather than rapid deep convection, as seen in recent high-resolution simulations [59].

Following previous work [48], nonconvective MAPE is also calculated, which allows for latent heating but does not allow for release of convective instability as represented by vertical reordering of air originating at a given latitude (Figure 2-2b; see Section 2.6). EKE is expected to scale with nonconvective MAPE rather than the full moist MAPE because release of convective instability involves local dissipation of kinetic energy without necessarily contributing to large-scale EKE, and because convection is associated with mixing and diffusion of water vapor which acts as a sink of moist

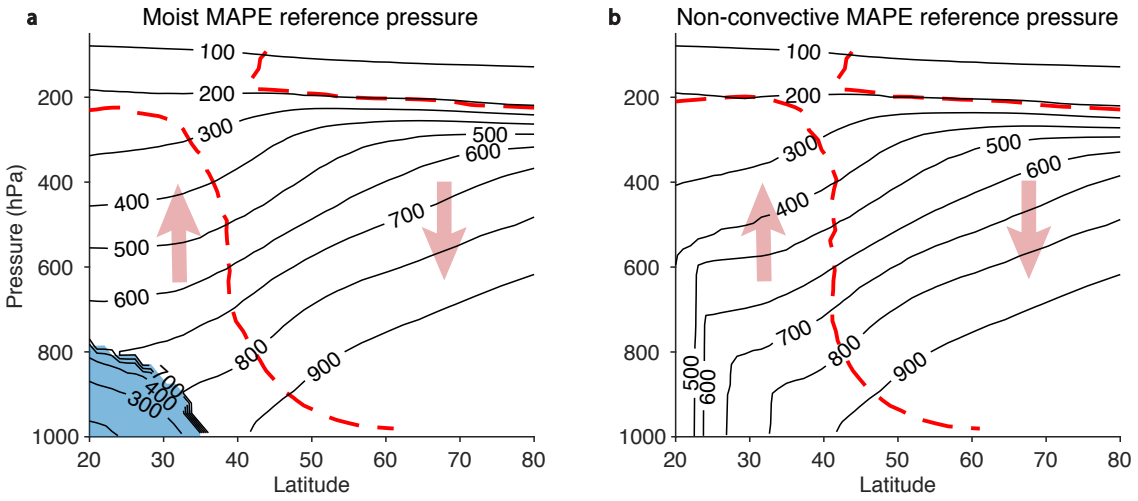

Figure 2-2: Visualization of MAPE calculations. Parcel rearrangements in the calculation of (a) moist MAPE and (b) nonconvective MAPE based on climatological JJA zonal-mean temperatures and relative humidities from the ERA-Interim reanalysis (1979-2017). Black contours (contour interval 100 hPa) show the pressure of a given air parcel in the minimum-enthalpy state, referred to as the reference pressure. Arrows schematically indicate vertical motion of parcels. The red lines show where the reference pressure is equal to the pressure. Blue shading in (a) indicates a region of lower-tropospheric air bounded by a discontinuity in the reference pressure distribution, whose ascent to the upper troposphere corresponds to the release of convective instability.

MAPE [53].

Nonconvective MAPE is always less than or equal to moist MAPE [48], and here the concept of convective MAPE is introduced, defined as the moist MAPE minus nonconvective MAPE. Convective MAPE provides a link between convection and the mean state of the atmosphere, in contrast to CAPE which must be calculated from instantaneous soundings. Conditional instability of the mean state of the atmosphere is limited to low latitudes and does not contribute strongly to convective MAPE (see Section 2.6), and thus convective MAPE must be primarily generated by the large-scale circulation driven by the meridional temperature gradient. The weak conditional instability of the mean state of the atmosphere also implies that the alternative approach of calculating moist MAPE at each latitude in isolation (without allowing meridional movement) and then averaging in latitude would give a much smaller value than the convective MAPE.

Convective MAPE is calculated using adiabatic rearrangements, and therefore it does not account for convective instability driven by surface fluxes or radiative cooling. One can interpret convective MAPE as the energy available for moist convection driven by large-scale ascent in extratropical cyclones, and this study of changes in convective MAPE is complementary to previous studies that have investigated the physical basis of changes in tropical CAPE [70, 77, 78] and changes in midlatitude extreme CAPE driven by surface fluxes over land [1]. A summary of the four major categories of MAPE calculated in this chapter are presented in Table 2.1.

2.3 Changing Energetic Reservoirs

Time series and trends in MAPE for JJA over 20-80N and 1979-2017 are shown in Figure 2-3. Nonconvective MAPE demonstrates a downward trend of -1.5% per decade, with a 90% confidence interval of [-2.8, -0.3] % per decade, consistent in terms of percentage change with the downward trend in EKE (also calculated from ERA-Interim data) of -1.3% per decade, as seen in Figure 2-3a. Therefore, changes in mean temperature and humidity, combined into nonconvective MAPE, are sufficient

Table 2.1: Summary of all forms of atmospheric MAPE calculated in this chapter.

MAPE type	Description
Moist MAPE	Difference in enthalpy between the mean state and minimum enthalpy state possible through reversible parcel rearrangements.
Dry MAPE	As moist MAPE, but assuming constant relative humidity of 0%.
Nonconvective MAPE	As moist MAPE, but not permitting vertical reordering of parcels originating in the same column.
Convective MAPE	The difference between moist MAPE and nonconvective MAPE.

to explain the sign and magnitude of the change in EKE. The trends in dry and moist MAPE are also downward and the trend of dry MAPE is similar in magnitude to that of nonconvective MAPE (Appendix, Section 2.7, Figure 2-11b and Figure 2-11e).

Interestingly, EKE and nonconvective MAPE are not positively correlated for year-to-year variability when the timeseries in Figure 2-3a are detrended. This different behavior for year-to-year variability as compared to longer-term trends is likely because EKE and MAPE have a different relationship for unforced variability as compared to forced variability. For forced variability, such as the seasonal cycle of the storm tracks or the response of the storm tracks to climate change, an increase in EKE is associated with an increase in MAPE [48]. For unforced variability of the storm tracks, an increase in EKE is associated with amplified heat fluxes which lead to a subsequent decrease in baroclinicity and MAPE [84, 2, 83].

In contrast to the decreasing trend in nonconvective MAPE, convective MAPE demonstrates an upward trend of 1.1 J kg^{-1} per decade, with a 90% confidence interval of [0.7, 1.7] J kg^{-1} per decade (Figure 2-3b). This increase in the energy available to moist convection associated with extratropical cyclones implies a tendency toward more convective precipitation in summer in midlatitudes. Observations show a robust increase in the convective fraction of precipitation over Northern Eurasia [93], and it would be interesting to study changes in the convective fraction of precipitation in

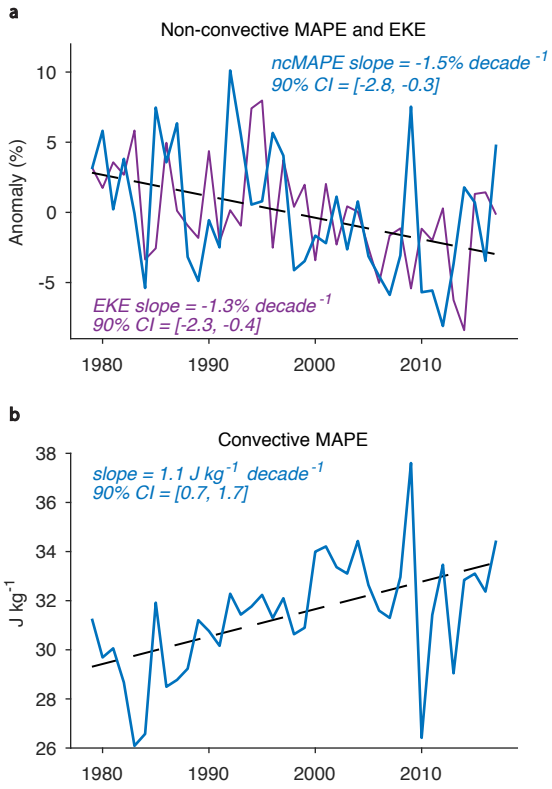

Figure 2-3: Time series and trends of energetic reservoirs for summer in the Northern extratropics. (a) Percent anomaly from climatological (1979-2017) mean for nonconvective MAPE (blue line) and eddy kinetic energy (purple line), and (b) convective MAPE, which is defined as the difference between moist MAPE and nonconvective MAPE. All results shown are for JJA over 20-80N based on ERA-Interim reanalysis. Trends and associated 90% confidence intervals are given in each panel. The dashed black lines show the linear best-fit trends for (a) nonconvective MAPE and (b) convective MAPE.

other midlatitude regions.

The signs and magnitudes of the trends in nonconvective and convective MAPE and in EKE are similar for narrower (30-70N) and wider (10-90N) latitude bands (Appendix, Section 2.7, Figure 2-11). The absolute rather than percentage changes are reported in convective MAPE because the absolute changes are less sensitive to the latitude band chosen. Absolute values for all types of MAPE are shown in Appendix, Section 2.7, Figure 2-12.

2.4 Relation to Surface Temperatures in Idealized Atmospheres

To better understand how climate change can cause changes of opposite sign in nonconvective MAPE and convective MAPE, we next consider how changes in mean surface temperature and meridional surface temperature gradient affect these energetic reservoirs in idealized atmospheres that are representative of Northern Hemisphere summer. Simple meridional profiles of surface temperature are prescribed and the mean surface temperature and meridional surface temperature gradient are varied independently. Given that the middle and lower troposphere are frequently close to neutral to moist convection in summer in the Northern extratropics [33], vertical temperature profiles are constructed in idealized atmospheres with prescribed relative humidity such that the virtual temperatures in the troposphere match the virtual temperatures in a reversible moist adiabat of a parcel lifted from the surface (see Section 2.6 for details). By this construction each individual column in isolation is not conditionally unstable and has no available potential energy, and thus non-zero convective MAPE must arise because of the meridional temperature gradient and the resulting lateral and vertical motion.

Figure 2-4 shows the variations in MAPE as a function of mean surface temperature and the mean meridional surface temperature gradient over 20-80N in the idealized atmospheres. The ranges shown are roughly centered on the ERA-Interim

mean temperatures and temperature gradients for Northern Hemisphere JJA of 292 K and 0.44 K degree^{-1}. Based on the ERA-Interim trends for JJA, surface temperature increased by roughly 1 K and the surface meridional temperature gradient decreased by roughly 0.02 K degree^{-1} over the whole period (Figure 2-5), and the observed changes in this time period are indicated by the red arrows in Figure 2-4. Nonconvective MAPE increases with the meridional temperature gradient as would be expected given that it behaves similarly to dry MAPE, which increases as the meridional temperature gradient squared with some compensation from increases in static stability [67]. Nonconvective MAPE also increases with mean surface temperature which likely reflects both increases in latent heating and induced changes in meridional temperature gradients aloft. On the other hand, convective MAPE has two different behavior regimes. For very weak meridional temperature gradients and thus weak large-scale overturning circulation, convective MAPE primarily increases with the meridional temperature gradient because the amount of air that reaches saturation increases with the strength of ascent at lower latitudes. For stronger meridional temperature gradients and thus stronger large-scale overturning, convective MAPE is more strongly a function of mean temperature, and this is the regime in which the observed JJA parameters fall. To understand why convective MAPE is sensitive to mean temperature, we first note that the vertical gradient in potential temperature along a moist adiabat increases with surface temperature [6], which implies that the ability of a given amount of large-scale ascent to cool the free troposphere and destabilize the column will also increase with temperature. The additional dependence on meridional temperature gradient reflects the ability of stronger temperature gradients to drive more ascent. The idealized atmosphere results show that convective MAPE is relatively more sensitive to mean surface temperature as compared to nonconvective MAPE, and this helps explain why convective MAPE can increase in response to mean warming and a weakening meridional temperature gradient even though nonconvective MAPE decreases.

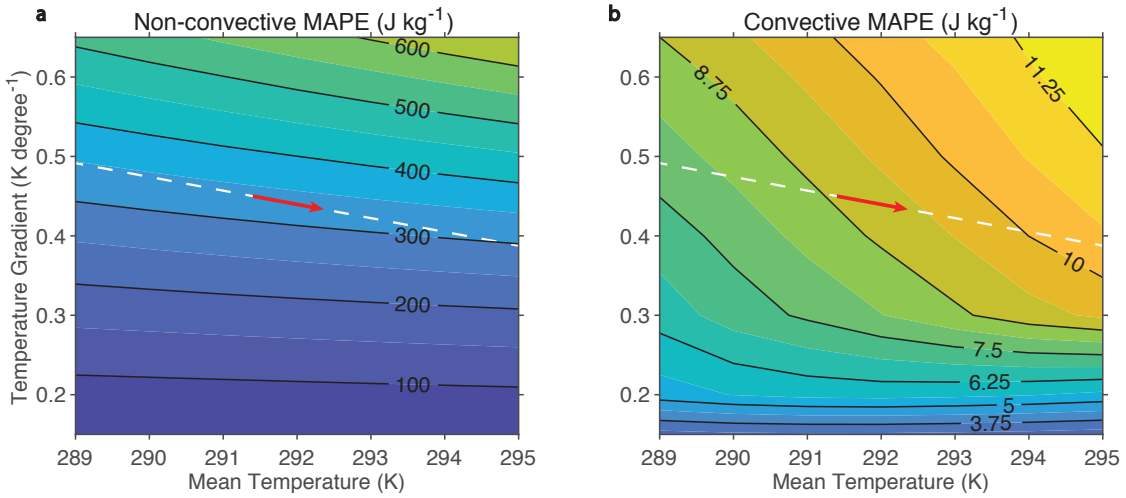

Figure 2-4: Energetic reservoirs of idealized atmospheres. (a) Nonconvective MAPE and (b) convective MAPE in idealized atmospheres over the latitude band 20-80N as a function of mean surface temperature and mean surface meridional temperature gradient in that latitude band. The idealized atmospheres are representative of Northern Hemisphere summer (see Section 2.6 for details). Contour intervals are 100 J kg^{-1} in (a) and 1.25 J kg^{-1} in (b). Red arrows indicate changes in the JJA atmosphere based on ERA-Interim trends over 1979-2017 (see Figure 2-5 and Section 2.6 for details), and white dashed line extends these changes along the same slope for clarity.

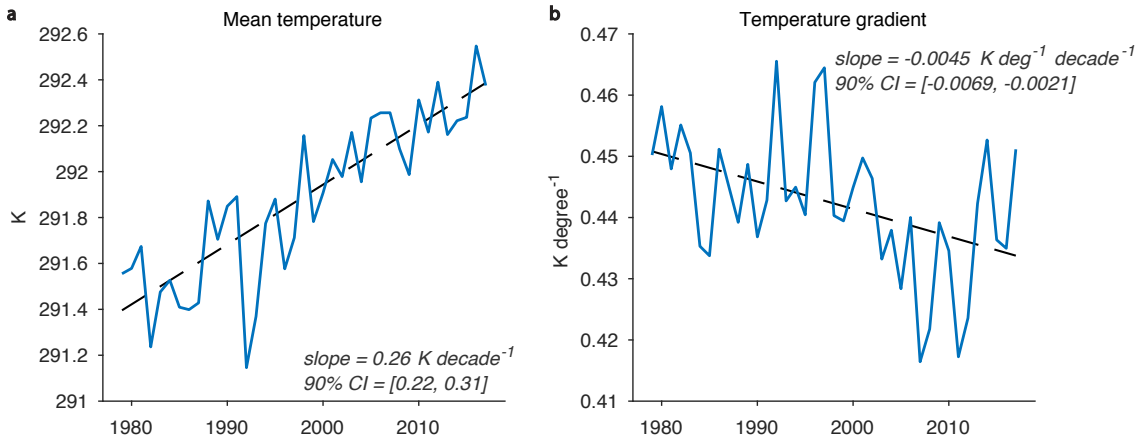

Figure 2-5: Time series and trends of 1000 hPa temperatures and meridional temperature gradients for the northern extratropics in JJA based on ERA-Interim reanalysis. (a) Mean 1000 hPa temperature over 20-80N and (b) mean meridional temperature gradient at 1000 hPa over 20-80N. See Section 2.6 for details of calculation.

2.5 Discussion

The results show that there have been opposite-signed changes in the energy available to the large-scale circulations and associated moist convection in recent decades in Northern extratropical summer, and that these changes are consistent with decreases in eddy kinetic energy and also consistent in sign with observed increases in the convective precipitation fraction. The changes in MAPE thus serve as a bridge between changes in the mean temperature and moisture of the atmosphere and changes in extratropical circulations. The MAPE framework may also be useful for considering past climate states based on surface temperature proxies to the extent that one can assume a vertical stratification in Northern midlatitude summer that is close to moist adiabatic.

While the link between changes in MAPE and EKE has been extensively studied in previous studies [68, 50, 49, 94], the results suggest a need for more investigation into connections between the mean state of the extratropical atmosphere (including both mean temperature and temperature gradients) and its convective behavior. For example, future work could compare convective MAPE with other measures of convection, such as instantaneous CAPE and the convective fraction of precipitation, across the seasonal cycle, in idealized simulations, and in warming scenarios. It is also important to investigate the contribution of zonal asymmetries to trends in nonconvective and convective MAPE since these asymmetries are not included in the zonal-mean MAPE considered here.

Decreasing nonconvective MAPE and increasing convective MAPE are consistent with model projections for Northern midlatitude summer over the 21^{st} century [48]. However, the large decrease of roughly 6% in nonconvective MAPE found here over recent decades is of similar magnitude to the multimodel-mean projected decrease in nonconvective MAPE over the whole 21^{st} century - a finding consistent with the observed decrease in cyclone activity being near the extreme end of what different climate models simulate for recent decades [12]. Substantial components of regional Arctic amplification may result from unforced variability, for example as a result of

the Atlantic Multi-decadal Oscillation [13] or via teleconnection to tropical Pacific variability [18], and future work could also investigate the contributions of anthropogenic forcing versus unforced variability to trends in MAPE.

2.6 Methods

2.6.1 Trends

All trends of time series are calculated using the Theil-Sen estimator, and 90% confidence intervals are calculated using the bootstrapping percentile method. Zonal-average trends in temperature and humidity from radiosonde datasets, and reanalysis products subsampled to radiosonde locations, are calculated as follows: stations are binned in 10° latitude bands, and the trend for each pressure level and latitude band is determined as the median trend of the seasonal average at that pressure level among the stations in that latitude band. The use of the median trend in latitude bands limits the influence of outlier trends in the radiosonde data [74].

2.6.2 Temperature and Humidity Data

For the calculation of MAPE, monthly mean temperature and humidity data from 1979-2017 with a grid resolution of 2.5° × 2.5° are taken from the ERA-Interim dataset, a global atmospheric reanalysis produced by the European Centre for Medium-Range Weather Forecasts (ECMWF) [17]. Seasonal-mean temperature and humidity are first calculated at each gridpoint. The zonal mean is then taken for a given year excluding any gridpoints at which the monthly pressure is greater than the monthly surface pressure at that point by more than 25 hPa (the pressure spacing near the surface) for any of the months in the season. The mean surface temperatures and surface meridional temperature gradients shown in Figure 2-5 are calculated from the zonal and seasonal mean of the 1000 hPa temperatures at each latitude as calculated above, and then meridionally averaged with area weighting.

Observational temperature data are taken from IUKv2 [74], a radiosonde dataset

homogenized by Iterative Universal Kriging to correct for time-varying instrument biases. For direct comparison with IUKv2, ERA-Interim data are subsampled in space and time to the coordinates closest to the station data in the IUKv2 dataset and trends are calculated as described above. This study uses ERA-Interim because of its relatively good agreement with the radiosonde data in terms of temperature trends when subsampled to the station locations (compare Figure 2-1a with Appendix, Section 2.7, Figure 2-8a), whereas other reanalysis products were found to have less good agreement, resulting in MAPE trends different to those presented here, including differences of sign in some cases.

Observational specific humidity data are taken from the homoRS92 dataset, a homogenized global, twice-daily humidity dataset that consists of the dataset described in Dai et al. [16], supplemented with dry-bias corrected data from Vaisala RS92 soundings [90]. In reporting relative humidity and specific humidity, this dataset employs a separate homogenized air temperature radiosonde product [24] combined with the homogenized dewpoint depression. Due to missing data in this dataset (which unlike IUKv2 is not iteratively filled), the following processing procedure is applied when determining trends: (1) at individual stations and pressure levels, only days with two measurements are considered, (2) only months with at least 70% of days are considered, (3) only JJA averages with all three months present are considered, and (4) only trends based on at least 70% of years are considered. The zonal-median trend following this procedure is shown in Figure 2-1b. Trends in ERA-Interim specific humidity data are compared to the observations by subsampling to the homoRS92 dataset station locations. Comparing the radiosonde humidity trends (Figure 2-1b) to the subsampled ERA-Interim humidity trends (Figure 2-9b) reveals a large discrepancy with much too weak moistening in ERA-Interim. To avoid this bias, the climatological JJA-mean relative humidity from ERA-Interim is used instead (averaged over 1979-2017) as the humidity input to the JJA MAPE calculation for a given year. This approach is consistent with expectations of small trends in relative humidity in the troposphere [73], and it implies trends in specific humidity that are more consistent with the homogenized radiosonde trends in specific humidity (compare Figure 2-1b

and Appendix, Section 2.7, Figure 2-8b). In calculating the JJA specific humidities for Figure 2-8b and in these calculations of MAPE, the saturation vapor pressure formulae over ice and liquid described in Simmons et al. [75] is used but with the ice and liquid phases merged using the method described in Wang and Randall [89]. The same saturation vapor pressure formulation is also used in calculating the moist adiabats in the idealized atmospheres (see below).

2.6.3 MAPE Calculations

The moist MAPE and its components are calculated for each year using the zonal- and JJA-mean temperatures and relative humidities from ERA-Interim. The temperature for a given year is the JJA-mean temperature for that year. As discussed above, the relative humidity is the climatological (1979-2017) JJA-mean relative humidity. Performing MAPE calculations using time-varying relative humidity (instead of climatological values) from ERA-Interim results in qualitatively similar results (Appendix, Section 2.7, Figure 2-13), but the increase in convective MAPE is 0.6 J kg^{-1} per decade (Appendix, Section 2.7, Figure 2-13b), which is roughly half the rate of increase that constant relative humidity implies. The zonal-mean temperatures and relative humidities for each JJA are first interpolated to a 40 by 40 equal-area staggered grid [40] in order to convert a two-dimensional problem in pressure and latitude coordinates into a one-dimensional problem in pressure coordinates only, although the original latitude for each parcel is stored for use in the calculation of nonconvective MAPE.

To calculate moist MAPE, the divide-and-conquer algorithm is used [79], which is a recursive algorithm that builds a low-enthalpy reference state by dividing the atmospheric domain into smaller subdomains. At each division, the pressure-derivative of enthalpy is evaluated at the mid-pressure of the subdomain and used to order the parcels from top to bottom of the subdomain; the top and bottom halves are then assigned to new subdomains. The divide-and-conquer algorithm has been found to work well in practice [79, 25], and in particular it gives a moist MAPE that is almost identical to that calculated using the exact Munkres algorithm for a similar case to

the one considered here [79]. Divide and conquer is used rather than Munkres because divide and conquer is faster and more straightforward to adapt to calculate convective and nonconvective MAPE.

To calculate nonconvective MAPE [48], the divide-and-conquer algorithm is modified such that when sorting parcels from top to bottom in a subdomain, parcels from a given initial latitude may not change their vertical ordering (i.e. whether one parcel is above the other). This condition that parcels cannot "leapfrog"Ăİ in pressure over other parcels from the same initial latitude leads to the continuous remapping of parcel pressure shown in Figure 2-2b, in which the reference pressure (the pressure in the minimum-enthalpy state) is a monotonic function of pressure at a given latitude.

To calculate convective MAPE, the nonconvective MAPE is subtracted from the moist MAPE. The magnitude of convective MAPE is reported per unit mass of the entire atmosphere in the specified latitude band (rather than the mass of a lifted parcel as is the case for CAPE), and as a result the reported values are much smaller than typical CAPE values in convective conditions. For JJA and 20-80N, the mass of the lifted air in the moist MAPE calculation (the blue shaded region in Figure 2-2a) is roughly 6% of the mass of the atmosphere over 20-80N, and the value of convective MAPE of roughly 32 J kg^{-1} becomes 530 J kg^{-1} when normalized by the mass of lifted air, which is comparable to typical CAPE values. Convective MAPE should not be confused with generalized CAPE (GCAPE) which is the moist available potential energy of a column of air in isolation [89, 58]. The moist available potential energy of the climatological and zonal mean at each latitude in isolation is only non-zero equatorward of 30N, and its meridional average with area weighting over 20-80N is only 1.3 J kg^{-1} as compared to convective MAPE of 32 J kg^{-1} for the same latitude band. Thus, conditional instability of the mean state does not contribute strongly to convective MAPE.

To calculate dry MAPE, the divide-and-conquer algorithm is used as for the moist MAPE calculation but with the input relative humidity set to zero.

2.6.4 EKE Calculations

To calculate EKE, a 2.5-6 day Butterworth bandpass filter is applied to 4-times daily horizontal winds on a 2.5° by 2.5° grid from ERA-Interim reanalysis over 1979-2017. Data below the surface pressure are removed (the approach describe above is not used for the monthly temperature and humidity because here we are using instantaneous data). A mass-weighted vertical integral of kinetic energy of the filtered wind time series is calculated at each latitude-longitude grid point to give the local vertically integrated EKE. A JJA- and area-weighted mean of the EKE is then calculated to give the time and spatial mean EKE over the specified latitude band for a given year.

2.6.5 Idealized Atmospheres

Idealized atmospheres are constructed by first imposing profiles of surface air temperature, T_s, as a function of latitude, ϕ:

$$T_s(\phi) = T_{eq} - \Delta_T \sin^2(\phi) \tag{2.1}$$

where T_{eq} is the surface temperature at the equator and Δ_T is a parameter controlling the meridional surface temperature gradient. Vertical temperature profiles in the atmosphere based on the surface temperatures are then determined as follows. First, reversible moist adiabatic parcel ascents with an assumed initial surface relative humidity of 85% are constructed in which the temperature profile follows a dry adiabat until saturation, after which it follows a saturated moist adiabat. A stratosphere with a constant temperature of 240K is imposed above the tropopause, with the tropopause defined as the level at which the parcel ascents reach 240K. While warmer than the real tropopause, this choice limits the extent to which upper-level meridional temperature gradients become much steeper than in the real atmosphere, inflating MAPE values. Next, vertical relative humidity profiles are imposed with boundary-layer relative humidity of 85% from the surface up to 900 hPa, free-tropospheric relative humidity of 45% between 900 hPa and the tropopause, and stratospheric relative humidity of 0.01%. Using one value of free-tropospheric relative humidity at all latitudes

is a simplification, and a value is chosen close to the climatological value at lower latitudes where ascending air originates. Lastly, temperature profiles are constructed such that the virtual temperature profile with the imposed relative humidity values matches the virtual temperature profile of the moist adiabat. This procedure allows for the production of a sub-saturated atmosphere that is neutral to moist convective instability. As a result, the convective MAPE is driven by the large-scale pattern of ascent and descent rather than having a contribution from conditional instability in the initial condition at a given latitude. In particular, the moist available potential energy of a column of air at a given latitude in isolation, the GCAPE [58], is zero.

T_{eq} and Δ_T are solved for, to produce an evenly spaced grid of mean surface temperatures and surface temperature gradients averaged with area weighting over the latitude band 20-80N. The mean surface temperatures are 289-295 K at increments of 0.5 K, and the mean meridional surface temperature gradients are 0.15-0.65 K degree^{-1} at increments of 0.05 K degree^{-1}. The moist MAPE and nonconvective and convective components are calculated for each of these idealized atmospheres over 20-80N. The resulting values of moist MAPE and its convective and nonconvective components are shown in Figure 2-4.

Based on ERA-Interim over JJA and 20-80N, the mean surface temperature is 292 K and the mean meridional surface temperature gradient is 0.44 K degree^{-1} (Figure 2-5). At these values, the nonconvective MAPE for the idealized atmosphere is 325 J kg^{-1} as compared to 185 J kg^{-1} from ERA-Interim, and the convective MAPE for the idealized atmosphere is 9 J kg^{-1} as compared to 32 J kg^{-1} from ERA-Interim. The larger nonconvective MAPE in the idealized atmosphere likely relates to the meridional temperature gradients aloft being too steep because the idealization of moist-adiabatic lapse rates becomes less accurate at higher latitudes. The smaller convective MAPE in the idealized atmosphere may relate to inaccuracy in the idealized relative humidity structure since convective MAPE only receives a small contribution from conditional instability of the mean state in ERA-Interim. However, these discrepancies in absolute values are not problematic because the aim in using the idealized atmosphere is to better understand the relative changes in convective

and nonconvective MAPE as a function of the surface parameters.

2.7 Appendix: Supplementary Figures

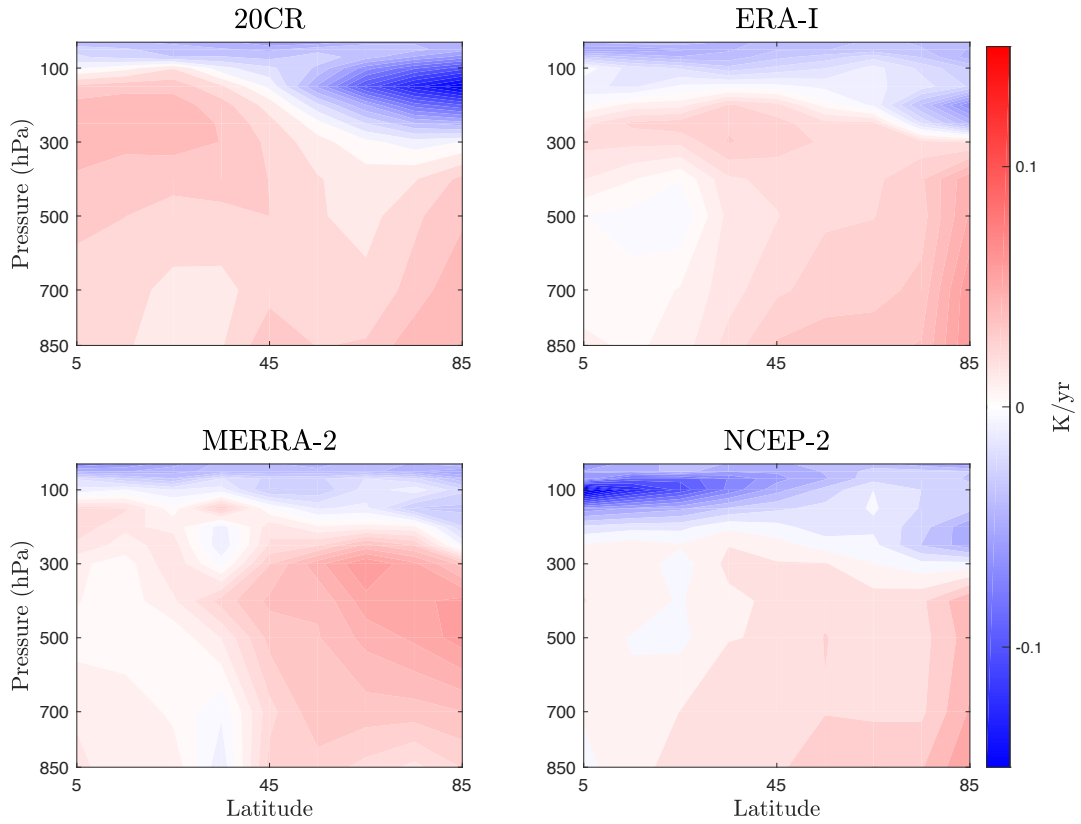

Figure 2-6: Changes in JJA temperature, 1979-2017, for four separate reanalysis products. Trends in 20th Century Reanalysis (20CR), ERA-Interim Reanalysis (ERA-I), MERRA-2 Reanalysis (MERRA-2), and NCEP-2 Reanalysis (NCEP-2).

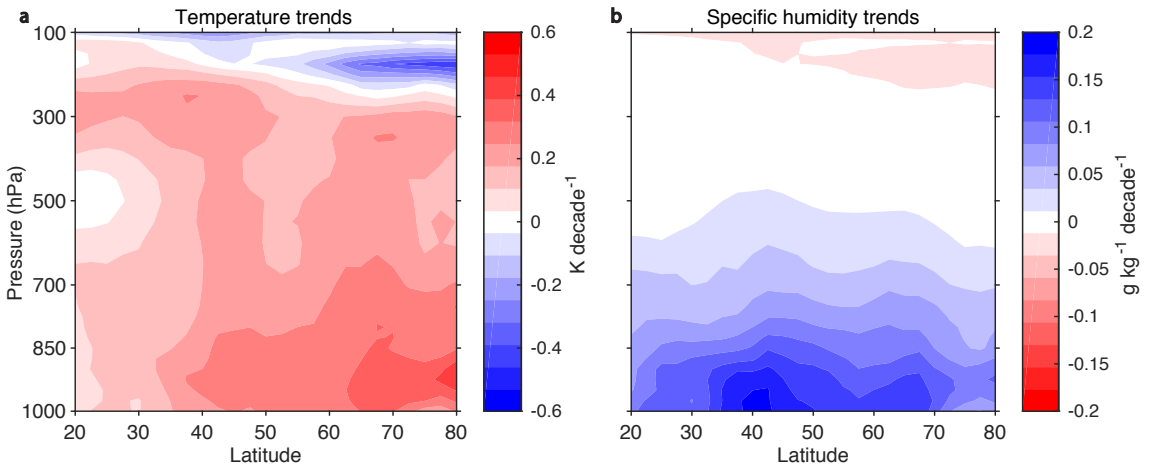

Figure 2-7: ERA-interim changes in JJA temperature and moisture, 1979-2017. Trends in (a) zonal mean JJA temperature and (b) zonal mean JJA specific humidity, assuming constant JJA relative humidity.

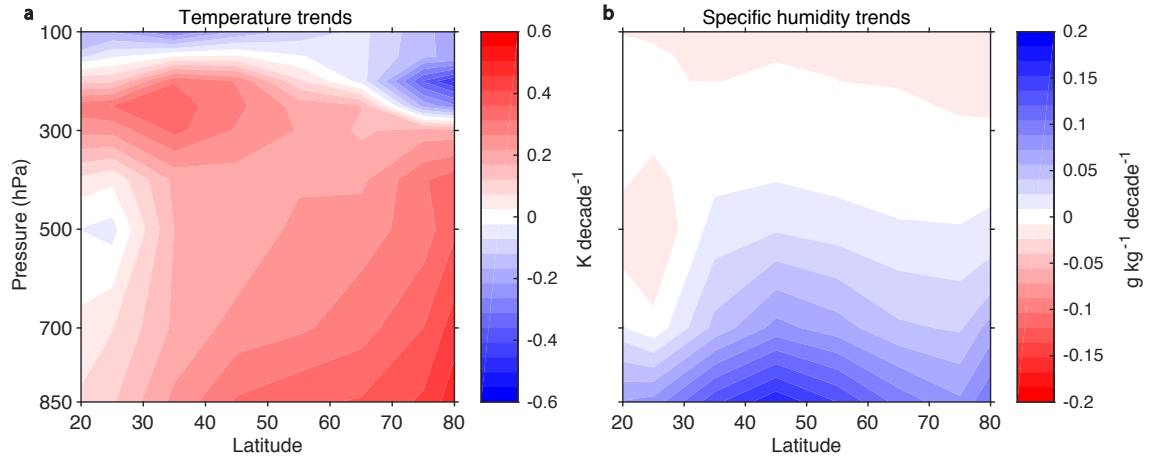

Figure 2-8: Subsampled ERA-Interim changes in JJA temperature and moisture. (a) Median JJA temperature trends in 10-degree latitude bands from ERA-Interim, subsampled to IUKv2 locations (1979-2015), and (b) median JJA specific humidity trends in 10-degree latitude bands from ERA-Interim assuming constant relative humidity and subsampled to HomoRS92 locations (1979-2010).

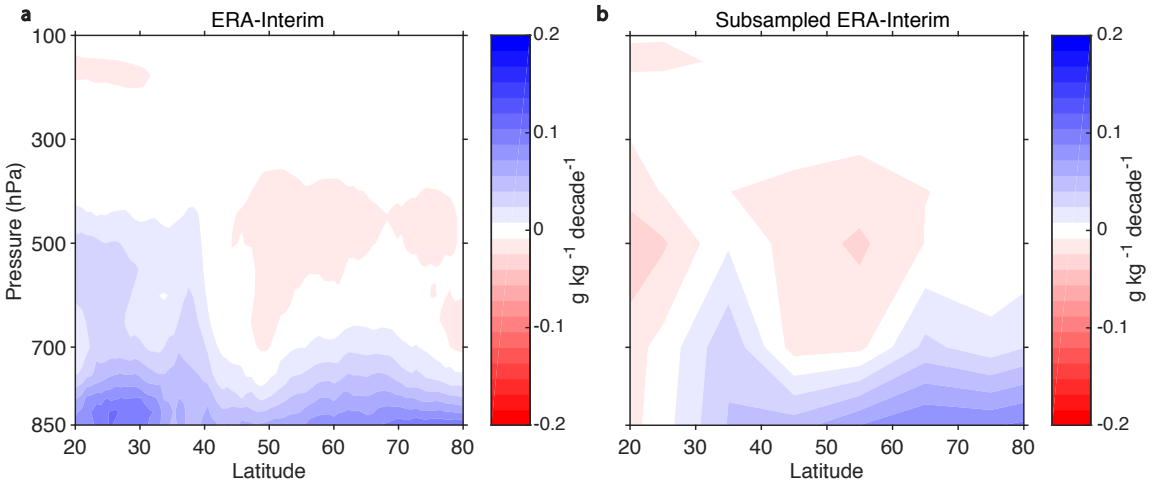

Figure 2-9: ERA-Interim changes in JJA specific humidity with time-varying relative humidity. (a) Trends in zonal mean JJA specific humidity from ERA-Interim with time-varying relative humidity (1979-2017) and (b) median JJA specific humidity trend in 10-degree latitude bands from ERA-Interim with time-varying relative humidity and subsampled to HomoRS92 locations (1979-2010).

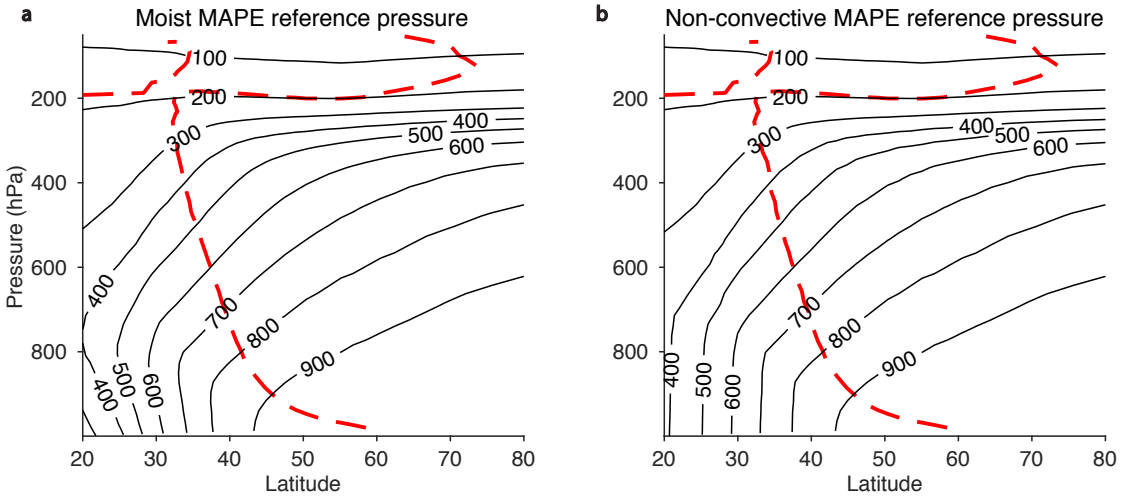

Figure 2-10: As in Figure 2-2 but for DJF. There is no discontinuity in the reference pressure distribution for the DJF rearrangement shown in panel a. Based on climatological temperatures and humidities, the convective MAPE as a percentage of moist MAPE is roughly 1% for DJF as compared to 16% for JJA.

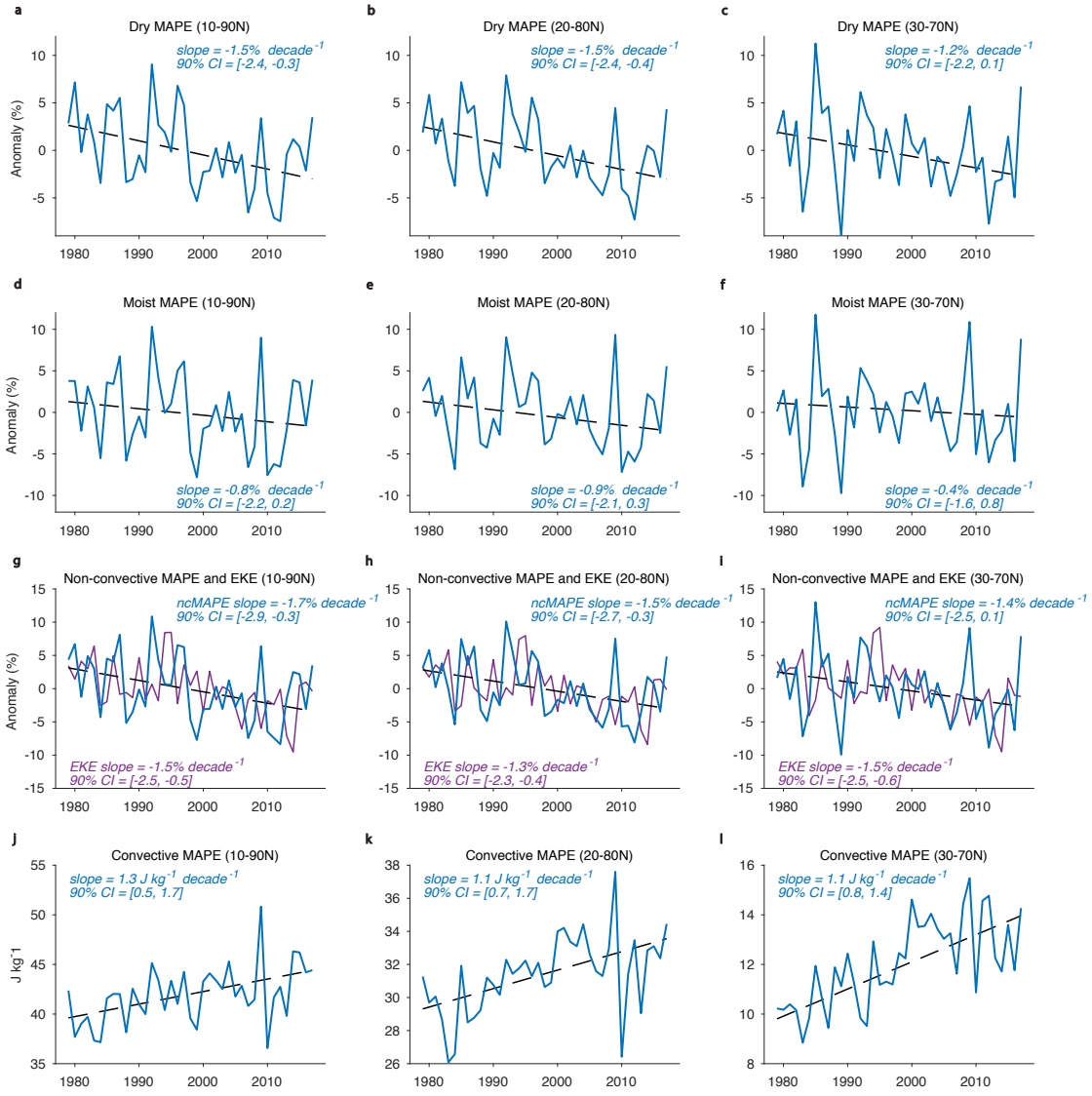

Figure 2-11: Time series and trends of energetic reservoirs for JJA in the Northern extratropics for different latitude bands. (a-c) Dry MAPE, (d-f) moist MAPE, (g-i) non-convective MAPE and EKE, and (j-l) convective MAPE over (a,d,g,j) 10-90N, (b,e,h,k) 20-80N, and (c,f,i,l) 30-70N. All results are based on ERA-Interim reanalysis. Trends and associated 90% confidence intervals are given in each panel. The dashed black lines show the linear best-fits for (a-c) dry MAPE, (d-f) moist MAPE, (g-i) non-convective MAPE, and (j-l) convective MAPE.

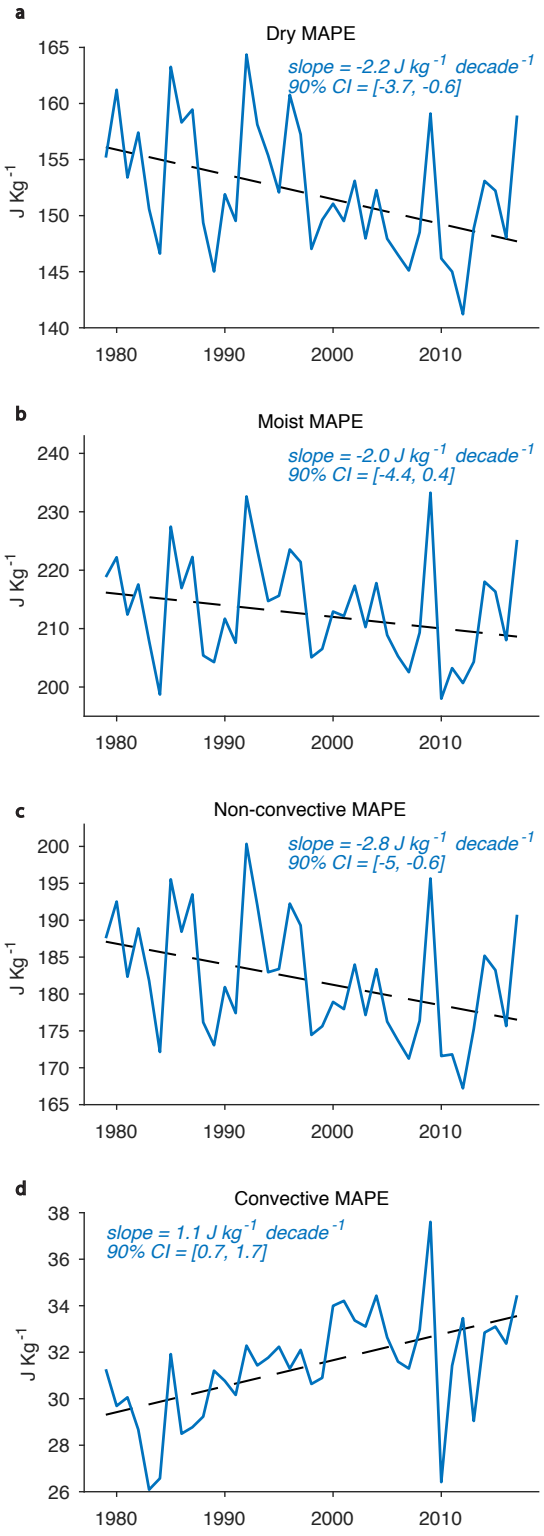

Figure 2-12: Time series and trends of energetic reservoirs for summer in the Northern extratropics showing absolute values rather than percentage anomalies. (a) Dry MAPE, (b) moist MAPE, (c) non-convective MAPE, and (d) convective MAPE. All results are for JJA over 20-80N based on ERA-Interim reanalysis. Trends and associated 90% confidence intervals are given in each panel, and the dashed black lines show linear best fits.

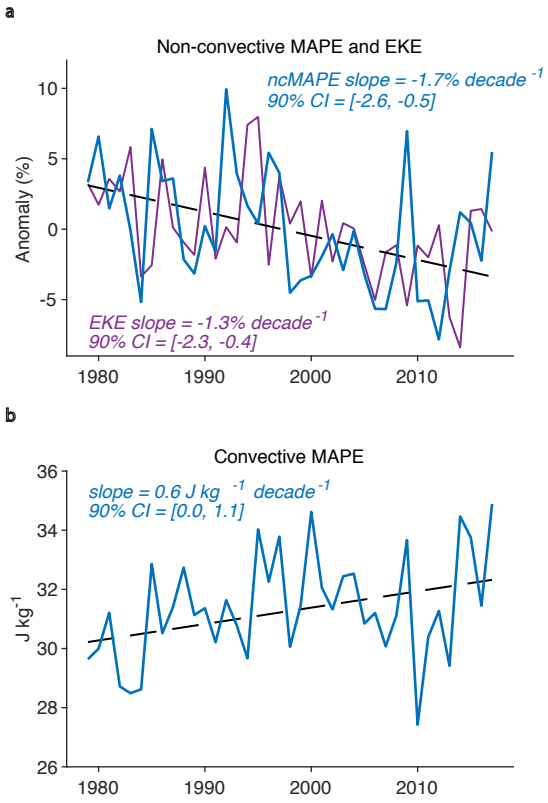

Figure 2-13: As in Figure 2-3 , but MAPE is calculated using time-varying relative humidity from ERA-Interim.

Chapter 3

Weakening of the Extratropical Storm Tracks in Solar Geoengineering Scenarios

This chapter has been adapted from a previously published paper [23]: C. G. Gertler, P. A. O'Gorman, B. Kravitz, J.C. Moore, S. J. Phipps, and S. Watanabe. Weakening of the extratropical storm tracks in idealized solar geoengineering scenarios. Geophysical Research Letters, 47(e2020GL087348), 2020.

Abstract: Solar geoengineering that aims to offset global warming could nonetheless alter atmospheric temperature gradients and humidity and thus affect the extratropical storm tracks. Here, climate model simulations are first analyzed from experiment G1 of the Geoengineering Model Intercomparison Project (GeoMIP), in which a reduction in incoming solar radiation balances a quadrupling of CO_2. The Northern Hemisphere extratropical storm track weakens by a comparable amount in G1 as it does for increased CO_2 only. The Southern Hemisphere storm track also weakens in G1, in contrast to a strengthening and poleward shift for increased CO_2. Using mean available potential energy, the changes in zonal-mean temperature and humidity are shown to be sufficient to explain the different responses of storm track intensity. Similar weakening is demonstrated in a more complex geoengineering scenario. Results

offer insight into how geoengineering affects storm tracks, highlighting the potential for geoengineering to induce novel climate changes.

3.1 Introduction

Active management of the Earth's climate through solar geoengineering, in which incoming shortwave radiation is reflected to counteract the longwave radiative forcing from greenhouse gasses, is one proposed mechanism to avert dangerous global warming due to anthropogenic greenhouse gas emissions, although this approach also brings a novel set of climate changes and unknowns [30, 62]. Among the most widely discussed proposals is stratospheric aerosol injection, in which particles or their precursors injected into the stratosphere reduce overall planetary albedo. Simulations with sulfate aerosol geoengineering demonstrate successful stabilization of global mean surface temperature despite increasing greenhouse gas concentrations [3]. Because many climate models do not include the relevant processes to reliably simulate more realistic approaches, an idealized scenario with reduced solar constant, known as sunshade geoengineering, is often studied in climate models as a simpler proxy for stratospheric aerosol injection [34]. Reducing the solar constant does not offset the radiative forcing of increased CO_2 at each latitude separately, and thus there are residual changes in temperature at different latitudes [34, 45, 66] which have the potential to affect the general circulation.

The extratropical storm tracks, regions of heightened extratropical cyclone activity, are an important feature of the general circulation that nonetheless remains understudied in the geoengineering literature. Extratropical cyclones are strongly associated with wind, temperature, and precipitation extremes [71], and the storm tracks are the dominant contributor to poleward transport of energy in midlatitudes [87]. Furthermore, momentum convergence resulting from the storm tracks maintains surface westerlies [54] which help drive the ocean circulation and thus affect carbon and heat uptake. Variations in the storm tracks have also been shown to modulate ventilation of the boundary layer and thus affect air quality [37].

Here the response of the extratropical storm tracks is analyzed in solar geoengineering scenarios. A simple metric of temporal variance in sea level pressure change, referred to here as extratropical cyclone activity (ECA), is used to measure the general intensity of the storm tracks, although it does not distinguish between strength and frequency of individual storms. ECA is chosen based on data availability, but it has been shown to behave similarly to other metrics of cyclone activity based on winds and feature tracking for the climatological mean and the response to climate change [12].

First, analysis is presented of experiment G1 of the Geoengineering Model Intercomparison Project (GeoMIP) [36], an idealized sunshade geoengineering experiment in which the solar constant is reduced to balance an instantaneous quadrupling of CO_2 relative to preindustrial concentrations. The changes in the storm tracks are also briefly considered in two alternate experiments: the recently proposed Half G1 experiment in which the solar constant is reduced by less than in G1 to avoid overcompensating effects on the climate system, and the Geoengineering Large Ensemble (GLENS). GLENS is an ensemble of simulations with CO_2 levels following Representative Concentration Pathway 8.5 (RCP8.5) and SO_2 injections at four locations using a feedback-control algorithm [85]. The aim of the feedback-control algorithm is to stabilize the meridional surface temperature gradient and interhemispheric surface temperature gradient in addition to global mean surface temperature [35]. In GLENS, the northern and southern extratropical storm tracks weaken and the southern storm track shifts poleward compared to present day [60, 76]. Idealized experiments demonstrate that the poleward shift is due to stratospheric heating induced by the aerosols, but the general weakening is not well understood and cannot be attributed to stratospheric heating alone [76]. The GLENS simulations were designed to limit changes in the surface meridional temperature gradient at the planetary scale among other targets, but there are nonetheless substantial changes in meridional temperature gradients at midlatitudes [85], which could affect storm track intensity. All model experiments considered in this Chapter, and their main attributes, are listed in Table 3.1.

To connect factors such as meridional temperature gradients to storm track intensity, the concept of mean available potential energy (MAPE) [38] is used. MAPE is the energy reservoir from which extratropical cyclones draw, and it is defined as the difference in integrated enthalpy between an atmosphere's mean state and the minimum-enthalpy state possible from reversible adiabatic parcel rearrangements [38, 40]. MAPE has been shown to scale linearly with the intensity of extratropical storm tracks as measured by eddy kinetic energy (EKE) [22, 48, 49, 50, 68]. MAPE can also be separated into nonconvective and convective components [22, 48]. Focus is placed on nonconvective MAPE, which is similar to MAPE but does not permit the release of convective instability through vertical reordering of air originating at a given latitude, because it has previously been found to scale more closely with storm track intensity under forced changes to climate such as the seasonal cycle and global warming [22, 48]. In general, MAPE increases with increasing meridional temperature gradients, decreasing dry static stability, and increasing specific humidity [38, 40], and this permits reasoning about the effects of changes in these factors on storm-track intensity.

The paper proceeds as follows. In Section 3.2 the model output and main analytical methods used in the paper are introduced. Section 3.3 details the changes in mean state and extratropical storm track intensity in G1 and links them through MAPE. Section 3.4 gives an analysis of the storm track response in GLENS and Half G1. Section 3.5 presents a discussion of the results and conclusions.

3.2 Simulations and Storm Track Measures

3.2.1 Climate Models and Simulations

This study uses output from six climate models that performed the GeoMIP G1 experiment, the CMIP5 PI experiment, and the CMIP5 4xCO_2 experiment. Grid size and references for each of the six models can be found in Appendix B, Section 3.7, Table 3.2. While more than six models performed the G1 experiment, the models

used here represent those with publicly available output necessary for the analyses described below. In the G1 experiment, CO_2 concentrations are instantaneously quadrupled compared to pre-industrial levels, and the solar constant is simultaneously reduced to counteract the resulting radiative imbalance at the top of atmosphere [36]. The models are run for 50 years under these conditions, and to avoid transient effects in the first 10 years of the simulation, all results presented here are based on time averages for the years 11-50, as is typical for the GeoMIP experiments [34]. The CMIP5 PI experiment keeps CO_2 at pre-industrial levels, and the 4xCO_2 experiment instantaneously quadruples CO_2 [82], making these experiments natural comparisons to G1, as they represent a baseline and a global warming scenario, respectively. For purposes of comparison, 40-year averages are used from these experiments as well, based on years 11-50 of PI and 4xCO_2. For the 4xCO_2 experiment, equilibration would occur on much longer timescales than considered here, but the climate changes compared to PI are already large in years 11-50. Responses are reported for G1 and 4xCO_2 relative to PI in all cases. The approach used to calculate changes under Half-G1 is described in Section 3.4.

This study also uses output from ensembles of simulations using the Community Earth System Model Version 1 (CESM1) with the Whole Atmosphere Community Climate Model (WACCM) as its atmospheric component (CESM1-WACCM), described in detail in Tilmes et al. [85]. The simulations have a latitudinal resolution of 0.9°, a longitudinal resolution of 1.25°, and 70 layers in the vertical, and they explicitly simulate the formation of sulfate aerosols from SO_2 injection. An ensemble of 19 simulations run from 2010 to 2030 with forcings following RCP8.5 is used as the control simulation (referred to as BASE). In GLENS, 19 simulations are run from year 2010 to 2099 with forcings following RCP8.5 and additional stratospheric SO_2 injections at four locations controlled by a feedback algorithm. Three of the BASE simulations were extended to 2095, and this smaller ensemble is used here as a global warming scenario for comparison (referred to as RCP8.5). Ensemble- and time-mean values over the 20-year period from 2076 to 2095 of the GLENS and RCP8.5 simulations are compared to ensemble- and time-mean values over the first 20 years of the BASE

simulation in order to compare potential future climates to present day. See Table 3.1 for a summary of all simulations considered in this chapter.

Table 3.1: Model simulations employed in this chapter and their main attributes.

Experiment	Description	Years
PI	Preindustrial control	11-50
4xCO_2	Instantaneous quadrupling of CO_2 relative to preindustrial concentrations.	11-50
G1	Instantaneous quadrupling of CO_2 relative to preindustrial concentrations and simultaneous reduction in solar constant to balance radiative forcing at top-of-atmosphere.	11-50
Half G1	Pseudo-experiment representing a smaller reduction in solar constant, in which values are linearly interpolated between the time-mean values for G1 and 4xCO_2 at each grid cell.	11-50
BASE	Greenhouse gas forcings following RCP8.5.	2010-2030
RCP8.5	Greenhouse gas forcings following RCP8.5.	2076-2095
GLENS	Greenhouse gas forcings following RCP8.5 and additional stratospheric SO_2 injections at four locations controlled by a feedback algorithm.	2076-2095

3.2.2 Extratropical Cyclone Activity

To estimate extratropical cyclone activity (ECA), instantaneous daily sea level pressure (psl) is used for the GeoMIP experiments and 6-hourly mean psl is used for the GLENS experiments to calculate the temporal variance of 24-hour psl change at each location [12],

$$ECA = \overline{[psl(t + 24h) - psl(t)]^2}, \tag{3.1}$$

where the overbar represents a time average over the period of interest, and $psl(t+24h)$ is the sea level pressure 24 hours after a given time t. ECA is usually calculated using instantaneous 6-hourly psl but these data were not available for most of the simulations used here. However, the results were very similar when instantaneous 6-

hourly psl was used in a model for which it was available (IPSL-CM5A-LR). An area weighted mean of ECA is also calculated over the extratropical latitude band 30°-70° in each hemisphere to give estimates of the overall extratropical cyclone activity.

3.2.3 Calculation of MAPE

For the G1, PI and 4xCO_2 experiments, zonal-mean temperature and humidity averaged over the 40-year periods described above are used to calculate MAPE and its nonconvective and convective components for each model individually. For the GLENS and BASE experiments, ensemble- and zonal-mean temperature and humidity averaged over the time periods described above are used. The zonal-mean temperatures and relative humidities in the 30°-70° latitude band in each hemisphere are interpolated to a 40×40 equal-area grid in latitude and pressure to create parcels of equal mass. The conclusions are not sensitive to this exact choice of latitude band. The divide-and-conquer algorithm [79] is used to find the minimum enthalpy state, and MAPE is then calculated as the difference between the enthalpy of the original state and that of the minimum-enthalpy state. The divide-and-conquer algorithm, while not exact, has been shown to be accurate for similar calculations to the ones performed here [79], and it can be adapted easily to calculate the nonconvective component of MAPE. To calculate nonconvective MAPE, a minimum-enthalpy state is found with the constraint that parcels originating from the same latitude cannot change their pressure ordering (see [22] and Chapter 2 of this thesis for further discussion). Convective MAPE is defined as the difference between MAPE and nonconvective MAPE.

3.3 Results for the G1 Experiment

3.3.1 Changes in Temperature and Humidity

The responses of temperature and meridional temperature gradient in G1 and 4xCO_2 relative to PI are shown in the model- and zonal-mean in Figure 3-1. Zonal-mean

temperatures were interpolated onto a common grid (with grid spacings of 4° in latitude and 20 hPa in pressure) before meridional temperature gradients were calculated and the mean across models was taken. Stippling indicates regions where fewer than five of six models agree on the sign of the response.

For G1, at high latitudes there is warming in the lower troposphere with weaker cooling above roughly 650hPa, and at low latitudes there is cooling throughout the troposphere that is strongest in the upper troposphere consistent with a moist-adiabatic tropical stratification (Figure 3-1a,). As a result, there is weakening of the meridional temperature gradient throughout the depth of the troposphere in the midlatitudes of both hemispheres (Figure 3-1c) which would tend to decrease MAPE and thus weaken the storm tracks. On the other hand, the dry static stability decreases in most regions (as can be inferred from Figure 3-1a) which would tend to increase MAPE and strengthen the storm tracks. The transition region from warming to cooling both at the surface and within the atmospheric column is somewhat uncertain, with different models transitioning in different areas (see Appendix C, Section 3.8, Figure 3-6 for individual models. Figures 3-6 to 3-17 are found in Appendix C, Section 3.8).

For 4xCO_2, the meridional temperature gradient in the Northern Hemisphere weakens in the lower troposphere but strengthens above roughly 500hPa (Figure 3-1d), and thus the changes in meridional temperature gradient in the lower and upper troposphere would tend to have opposing effects on storm track intensity. The Southern Hemisphere demonstrates changes of both signs in the meridional temperature gradient in the lower troposphere and stronger strengthening above 500hPa (Figure 3-1d). The dry static stability decreases in the polar regions but increases at lower latitudes (as can be inferred from Figure 3-1b). The exact structure does again differ among individual models but the general pattern is fairly robust (see Figure 3-7).

The magnitudes of temperature changes for 4xCO_2 are generally larger than those for G1 by a factor of 5. However, the changes in meridional temperature gradients are closer in magnitude between 4xCO_2 and G1, and for the Northern Hemisphere the inconsistent sign of the change in meridional temperature gradient at different

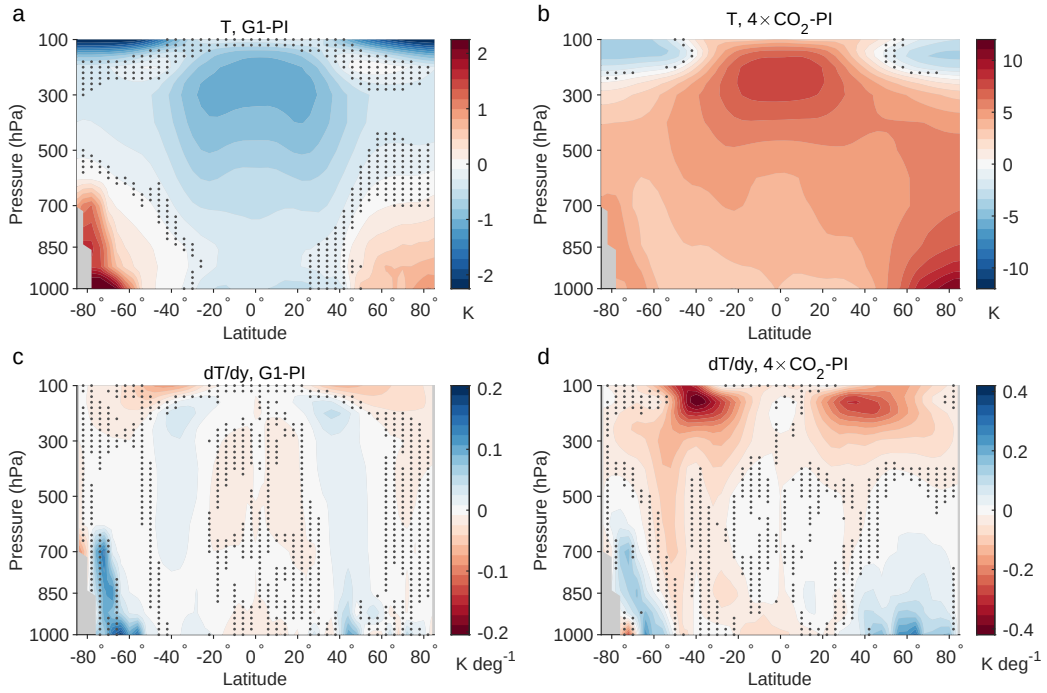

Figure 3-1: Model- and zonal-mean temperature and temperature gradient responses expressed as anomalies relative to PI. Shown are (a) temperature response for G1, (b) temperature response for 4xCO$_2$, (c) meridional temperature gradient response for G1, and (d) meridional temperature gradient response for 4xCO$_2$. Each panel has a different colorbar, and stippling indicates regions where fewer than five of six models agree on sign of change. Temperature gradients are calculated in the equatorward direction in each hemisphere and are in units of K per degree latitude.

levels for 4xCO_2 tends to reduce the magnitude of the overall effect on storm track intensity. As a result, we will see later that the storm-track responses are of similar magnitude in the Northern Hemisphere for these two idealized scenarios.

The signs of the specific humidity responses are mostly as expected from the patterns of temperature change assuming small change in relative humidity (Figure 3-8). For G1, there are increases in specific humidity at lower latitudes and decreases at high latitudes in the lower troposphere with some inter-model differences in the pattern of changes (Figure 3-9). For 4xCO_2, there are widespread increases in specific humidity consistently across models which would tend to increase MAPE and storm track intensity (Figure 3-10).

3.3.2 Changes in Extratropical Storm Tracks

As expected given the changes in mean temperature structure and specific humidity, extratropical storm track activity also changes in both the G1 and 4xCO_2 experiments. Figure 3-2 shows results for model-mean ECA versus latitude and longitude. ECA from each model was first interpolated onto a common grid (3° × 3° in latitude and longitude) before taking the mean across models. The extratropical storm tracks weaken in both hemispheres for G1 (Figure 3-2a), while the Northern Hemisphere storm track mostly weakens and the Southern Hemisphere storm track strengthens and shifts poleward for 4xCO_2 (Figure 3-2b). For model-mean ECA, the strongest decrease in G1 is roughly four times smaller in magnitude compared to the strongest increase in 4xCO_2.

Figure 3-2d shows the model- and zonal-mean changes in ECA interpolated to a common grid with 0.1° resolution in latitude, making clear that decreases in ECA in the Northern Hemisphere are of similar magnitude in G1 and 4xCO_2. For the Southern Hemisphere under 4xCO_2, ECA increases are greater for latitudes poleward of the peak latitude of zonal-mean ECA in PI (Figure 3-2d), and this leads to a poleward shift in peak latitude of zonal-mean ECA by 3°. By contrast the shifts in this peak latitude are small (<0.5°) in the Northern Hemisphere under 4xCO_2 and in both hemispheres under G1.

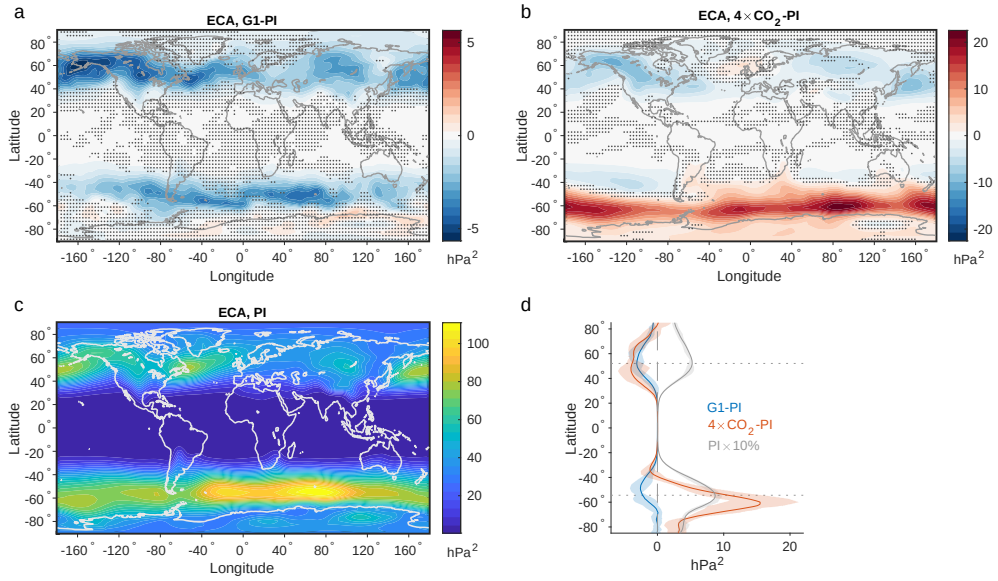

Figure 3-2: Model-mean storm track intensity as measured by ECA. Shown are (a) response (expressed as anomalies relative to PI) for G1, (b) response for 4xCO_2, (c) PI climatology, and (d) zonal-mean responses for G1 (blue) and 4xCO_2 (red), and 10% of the PI climatological value (gray). Panels (a) and (b) have different colorbars, and stippling in these panels indicates regions where fewer than five of six models agree on the sign of the response. Shading in (d) indicates range of inner 4 models (the second to the fifth sextiles), and horizontal dotted gray lines in (d) indicate latitudes of peak ECA in PI.

Some individual models demonstrate more heterogeneous storm-track changes (see Figure 3-11 and Figure 3-12). For instance, in IPSL-CM5A and HadGEM2-ES, ECA increases in some regions of both the northern and southern storm tracks for G1. However, the average change over the extratropical latitude bands for G1 is always negative except for the Southern Hemisphere of HadGEM2-ES (see Figure 3-3a).

Storm track changes in individual seasons are also more heterogeneous than changes in the annual mean (see Figure 3-13 and Figure 3-14). Local seasonal variability in storm track activity is important when considering the impacts of storm track changes. Regions of ECA increases in G1 in winter and spring at high northern latitudes are generally consistent with the findings of Moore et al. [45], which demonstrate increased cyclonic activity entering the Barents Sea in spring, affecting sea ice distribution. Nonetheless, in G1, the storm tracks always weaken on average in the extratropical latitude band in each hemisphere regardless of the season.

There are various possible metrics for storm track activity, and ECA was chosen for this study based on data availability. ECA and EKE give broadly similar results in one model with sufficient data to compare, IPSL-CM5A (see Section 3.6).

3.3.3 Changes in MAPE

Extratropical storm track intensity weakens in both hemispheres under G1 and this seems consistent in sign with decreases in mean meridional temperature gradients in both hemispheres. However, the static stability and specific humidity also change, and the storm track intensity in geoengineering scenarios could be affected by other factors such as changes in atmospheric longwave radiative cooling in response to increased CO_2 [76]. Therefore, it is important to address the question of whether the changes in storm track intensity are quantitatively consistent with the changes in mean temperature and moisture. To address this question, the linear scaling of storm track intensity with non-convective MAPE that has been found in previous studies is used [22, 48].

Consistent with linear scaling, the fractional changes in nonconvective MAPE and ECA are broadly similar to each other in individual models and in the model-mean,

and within each hemisphere and idealized scenario (Figure 3-3). In the model-mean of the northern extratropics, nonconvective MAPE decreases by 4.5% in G1 and by 7.9% in 4xCO_2, consistent with an ECA decrease by 5.2% in G1 and 8.2% in 4xCO_2. In the model-mean of the southern extratropics, nonconvective MAPE decreases by 2.5% in G1 and increases by 8.7% in 4xCO_2, consistent with an ECA decrease by 2.6% in G1 and increase by 9.8% in 4xCO_2. These values are summarized in Table 3.3. The inner four of six models (second to fifth sextile) examined here are always consistent with the model-mean changes of sign in both ECA and non-convective MAPE (Figure 3-3b).

Overall the comparison of changes in ECA and non-convective MAPE suggests that changes in ECA in these idealized scenarios can be explained by changes in mean temperature and humidity. Replacing nonconvective MAPE with dry MAPE by specifying zero specific humidity gives qualitatively similar results, suggesting that temperature changes are the primary driver of changes in non-convective MAPE and thus ECA. The convective component of MAPE increases by less under G1 as compared to 4xCO_2 for most models (Figure 3-15), which may imply less of an increase in the energy available for convection driven by ascent in extratropical cyclones.

3.4 Results for GLENS and Half G1

For the more complex GLENS simulations with stratospheric SO_2 injection, we again consider average ECA over 30°-70° and nonconvective MAPE calculated over 30°-70° but now for GLENS and RCP8.5 compared to BASE. In GLENS, nonconvective MAPE decreases by 14.9% and ECA decreases by 16.1% in the Northern Hemisphere, and nonconvective MAPE decreases by 6.7% and ECA decreases by 7.8% in the Southern Hemisphere. These decreases in nonconvective MAPE and ECA are consistent with decreases in the tropospheric meridional temperature gradient in both hemispheres (Figure 3-16). Ensemble-mean results for changes in ECA versus latitude and longitude are similar to the storm track response reported in Simpson et al. [76], with widespread weakening in both hemispheres (Figure 3-4). Thus, even in

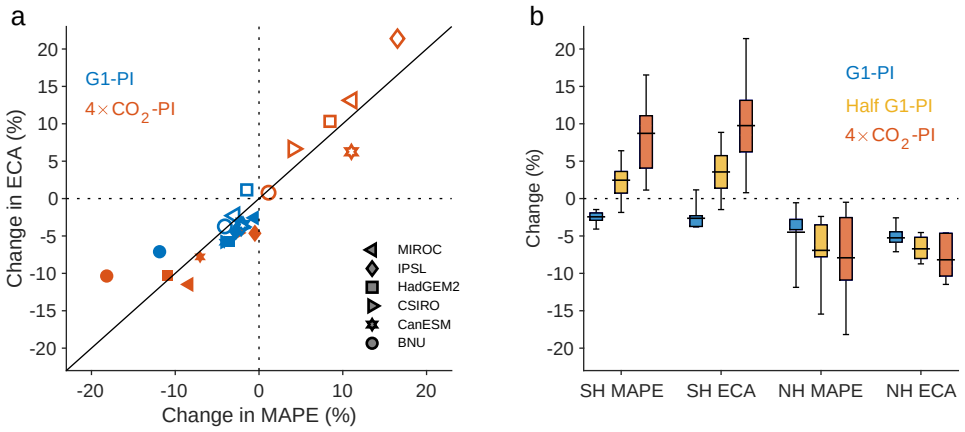

Figure 3-3: Extratropical storm track intensity and nonconvective MAPE responses relative to PI for different scenarios and hemispheres. (a) Fractional changes in ECA versus fractional changes in nonconvective MAPE for G1 (blue) and 4xCO_2 (red) for the Northern Hemisphere (filled symbols) and Southern Hemisphere (open symbols) of individual models. The solid line is the one-to-one line. (b) Fractional changes for Southern Hemisphere (SH) and Northern Hemisphere (NH) nonconvective MAPE and ECA for G1 (blue), Half G1 (yellow), and 4xCO_2 (red). Boxes indicate range of inner 4 models (second to fifth sextiles), whiskers indicate maximum and minimum values, and mid-lines indicate model-mean values. All ECA values shown are averaged over 30°-70° latitude, and all nonconvective MAPE values shown are calculated over 30°-70° latitude.

the more complex solar geoengineering simulations with feedback control and stratospheric SO_2 injection, a consistent weakening of the storm tracks occurs, and the changes in mean temperature and humidity alone are enough to explain the changes in storm track strength. In contrast to the multi-model mean for $4xCO_2$, there is no overall strengthening of the storm track in the Southern Hemisphere in RCP8.5 for this ensemble and model (see Table 3.3), but the changes in ECA are still more negative in both hemispheres in GLENS as compared to RCP8.5.

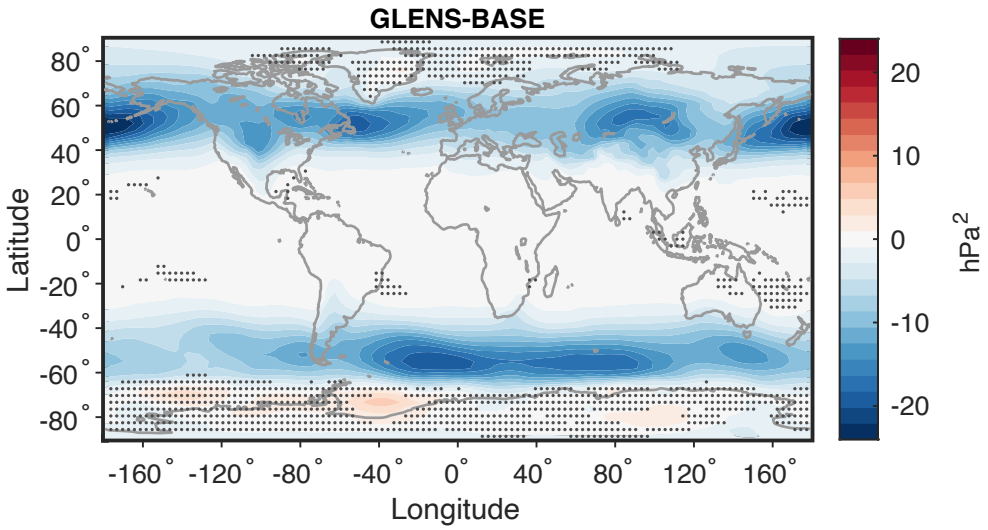

Figure 3-4: Ensemble-mean storm track intensity response for GLENS relative to BASE, as measured by ECA. Stippling indicates regions where fewer than five-sixths of ensemble members agree on the sign of the response.

We also consider the changes in ECA and nonconvective MAPE in a Half G1 scenario [29], in which temperatures and relative humidities are linearly interpolated between the time-mean values for G1 and $4xCO_2$ at each grid cell such that global mean temperature is half-way between $4xCO_2$ and G1. These temperatures and relative humidities are used to calculate nonconvective MAPE. ECA values are similarly interpolated at each grid cell, and results for ECA versus latitude and longitude in Half G1 can be seen in Figure 3-5. The results for changes in non-convective MAPE and average ECA calculated over the 30°-70° latitude bands under Half G1 are shown in Figure 3-3b. In the Northern Hemisphere, nonconvective MAPE weakens by 6.9% and ECA weakens by 6.7% compared to PI in a Half G1 scenario, weakening that is

of similar magnitude to the weakening under 4xCO_2. In the Southern Hemisphere, nonconvective MAPE strengthens by 2.5% and ECA strengthens by 3.6% under a Half G1 scenario, which is smaller than the strengthening under 4xCO_2. Unlike for some other aspects of the climate system, Half G1 fails to substantially reduce the change in storm track intensity in the Northern Hemisphere, and this is because the Northern Hemisphere storm track weakens by similar amounts in G1 and 4xCO_2. Thus a half-geoengineering scenario would not substantially reduce the magnitude of storm track changes in the Northern Hemisphere but would reduce them in the Southern Hemisphere.

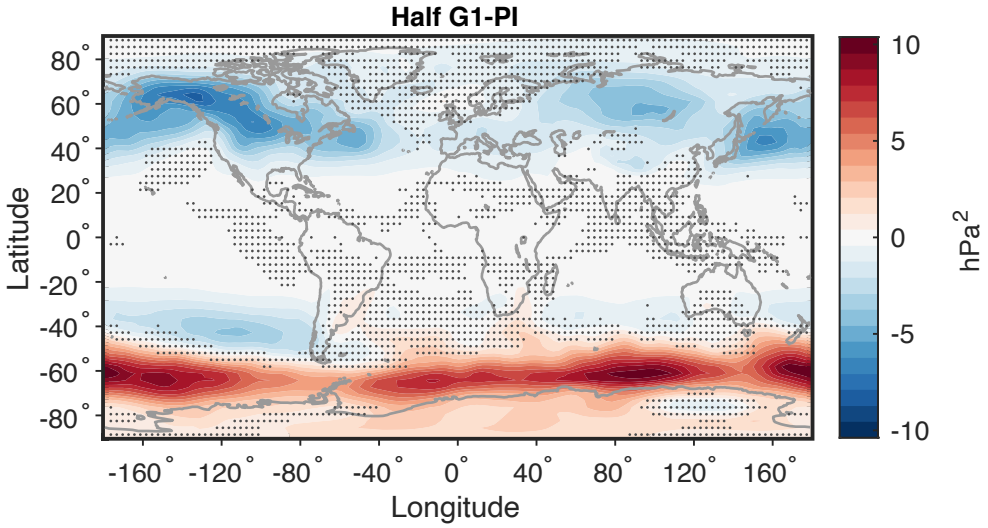

Figure 3-5: Model-mean storm track intensity response for Half G1 relative to PI, as measured by ECA. Stippling indicates regions where fewer than five of six models agree on the sign of the response.

3.5 Conclusions and Discussion

Changes to the mean temperature and humidity structure of the atmosphere under the G1 idealized geoengineering scenario reduce available potential energy in the northern and southern extratropics, leading to weakened extratropical storm tracks in both hemispheres with little change in their latitudinal position in the zonal mean. In the Northern Hemisphere, the storm track weakens by a comparable amount in G1

and 4xCO_2, despite the smaller changes in temperature in G1, in part because the meridional temperature gradient weakens at all levels in G1 but has offsetting changes of opposite sign in the upper and lower troposphere in 4xCO_2. In the Southern Hemisphere, the changes in storm track intensity are smaller in magnitude in G1 than in 4xCO_2, but of opposite sign, and there is no poleward shift of the storm track in G1 unlike under 4xCO_2. Given the importance of the extratropical storm tracks for both weather and climate [71], their possible weakening should be considered when trying to explain the physical basis of changes in climate and their impacts under geoengineering. Weakening of the extratropical storm tracks would be expected to, for example, reduce wind extremes in midlatitudes but also possibly lead to less efficient ventilation of air pollution from the boundary layer [37]. A weakening of the storm tracks may also contribute to the decrease in low cloud fraction over the storm track regions [66] and weakened poleward energy transport [65] identified previously in the G1 experiment.

It is reasonable to ask whether idealized sunshade geoengineering experiments are realistic or useful proxies for the type of solar geoengineering that is proposed as a possible intervention to global warming. However, even experiments with stratospheric SO_2 injection demonstrate changes in temperature gradients and humidity that reduce available potential energy and weaken the storm tracks. There are nonetheless differences between the sunshade and stratospheric aerosol experiments analyzed in this paper, such as that stratospheric heating drives a poleward shift of the mean jet in the Southern Hemisphere in GLENS [76] and to a lesser extent a poleward shift of the Southern Hemisphere storm track (Figure 3-4). Changes in both mean winds and the storm track intensity near the coast of Antarctica in GLENS can affect mean surface wind stress and thus lead to changes in the wind-driven ocean circulation. Such changes in ocean circulation under geoengineering may in turn affect ice sheet stability as discussed in McCusker et al. [44]. However, there is little agreement among models on the sign of changes in storm track strength in the Amundsen Sea sector, the region most crucial to West Antarctic ice sheet stability.

It is also reasonable to ask whether a geoengineering scenario in which the long-

wave radiative forcing from greenhouse gases is completely offset by engineered shortwave radiative forcing is the most reasonable or likely approach. In an idealized scenario representing roughly half of the reduction of solar radiation as compared to G1, changes in temperature and humidity still lead to a weakened storm track in the Northern Hemisphere of similar magnitude to the weakening in G1 and 4xCO_2. In the Southern Hemisphere, the storm track intensity increases by less in the Southern Hemisphere than under 4xCO_2, consistent with a smaller increase in MAPE. Further study of the storm track response in less aggressive geoengineering scenarios would be of interest.

The newfound understanding of changes to storm track strength found in this study is complementary to previous understanding of changes to the intensity of the hydrological cycle under solar geoengineering scenarios. In observations after the eruption of Mount Pinatubo, seen as a natural analog to geoengineering, a weakening of the hydrological cycle was observed, with decreases in precipitation over land and river discharge into the ocean [86]. Inspired by this observation, Bala et al. [5] demonstrate in equilibrium climate simulations of solar geoengineering that reductions in solar forcing drive reductions in evaporation more effectively than positive CO_2 forcing of similar magnitude drives increases in evaporation, reducing global mean precipitation. In G1, Kravitz et al. [34] use an energetic perspective to similarly demonstrate a greater reduction in evaporation than in 4xCO_2, leading to reductions in overall intensity of the hydrological cycle. For the more complex GLENS simulations, Simpson et al. [76] also use an energetic perspective to demonstrate a 3.06% reduction in overall precipitation predominantly due to the the same mechanism. While circulation changes are not the dominant factor in decreased precipitation and evaporation in the global mean, the reduced storm track intensity may contribute to decreases in precipitation minus evaporation in the extratropics.

The study of solar geoengineering presents a unique scientific and social challenge for climate science: characterizing one unprecedented climate state, deliberate geoengineering, as a potential alternative to another unprecedented climate state, global warming incidental to anthropogenic activity. While there likely exist other

consequences of solar geoengineering that the simulations studied here are unable to simulate, the results for the storm tracks give examples of unintended consequences where solar geoengineering can fail to mitigate an aspect of climate change (in the Northern Hemisphere) or overcompensate for it (in the Southern Hemisphere).

3.6 Appendix A: Different Storm Track Measures in One Model

Vertically integrated eddy kinetic energy (EKE) has been used as a metric for storm track intensity in most studies that compare mean available potential energy (MAPE) and storm track intensity (e.g. [48]), but this requires wind data at a minimum of daily resolution throughout the atmospheric column, and these data were only available for one model (IPSL-CM5A) for the G1, PI, and 4xCO2 experiments. Therefore, in this study a metric of storm track intensity is used, extratropical cyclone activity (ECA), that instead requires surface pressure (psl) data, which were available for a wider range of models. ECA also has the advantage that as a surface metric it is more relevant for some impacts of extratropical cyclones.

Here the changes in the extratropical storm track intensity as measured by ECA and EKE in IPSL-CM5A are compared. To calculate EKE, a 2.5-6-day Butterworth bandpass filter is applied to daily horizontal winds from IPSL-CM5A. At each location, a mass-weighted vertical integral of kinetic energy is calculated to give the local vertically integrated EKE, and an area-weighted mean of EKE is then calculated over the extratropical latitude bands as an estimate of extratropical storm track intensity. Averages over the 30-70° latitude band are considered, and PI is used as the baseline when calculating the response to climate change.

Figure 3-17 shows that the changes in ECA and EKE are similar in the Southern Hemisphere, with large increases for 4xCO2 and smaller decreases for G1, and in the Northern Hemisphere, with small decreases for both 4xCO2 and G1. It would be of interest to compare the behavior of ECA and EKE across a range of models and

scenarios in future work.

3.7 Appendix B: Supplementary Tables

Table 3.2: Climate models used for G1, 4xCO_2, and PI, their standard references, and the grid sizes of model output.

Model	Reference	Grid Size (lon × lat × pressure)
BNU-ESM	Ji et al. [31]	128 × 64 × 17
CanESM-2	Arora et al. [4]	128 × 64 × 22
CSIRO-Mk3L-1-2	Phipps et al. [57]	64 × 56 × 18
HadGEM2-ES	Collins et al. [14]	192 × 144 × 17
IPSL-CM5A-LR	Dufresne et al. [19]	96 × 96 × 17
MIROC-ESM	Watanabe et al. [91]	128 × 64 × 35

Table 3.3: Ensemble-average changes in ECA and nonconvective MAPE for all experiments compared to appropriate control experiments. For G1, 4xCO_2, and Half G1, the control experiment is PI. For GLENS and RCP8.5, the control experiment is BASE.

Experiment	NH ECA Change	NH MAPE Change	SH ECA Change	SH MAPE Change
G1	-5.2%	-4.5%	-2.6%	-2.5%
Half G1	-6.7%	-6.9%	3.6%	2.5%
4xCO2	-8.2%	-7.9%	9.8%	8.7%
GLENS	-16.1%	-14.9%	-7.8%	-6.7%
RCP8.5	-13.5%	-5.8%	-0.4%	3.5%

3.8 Appendix C: Supplementary Figures

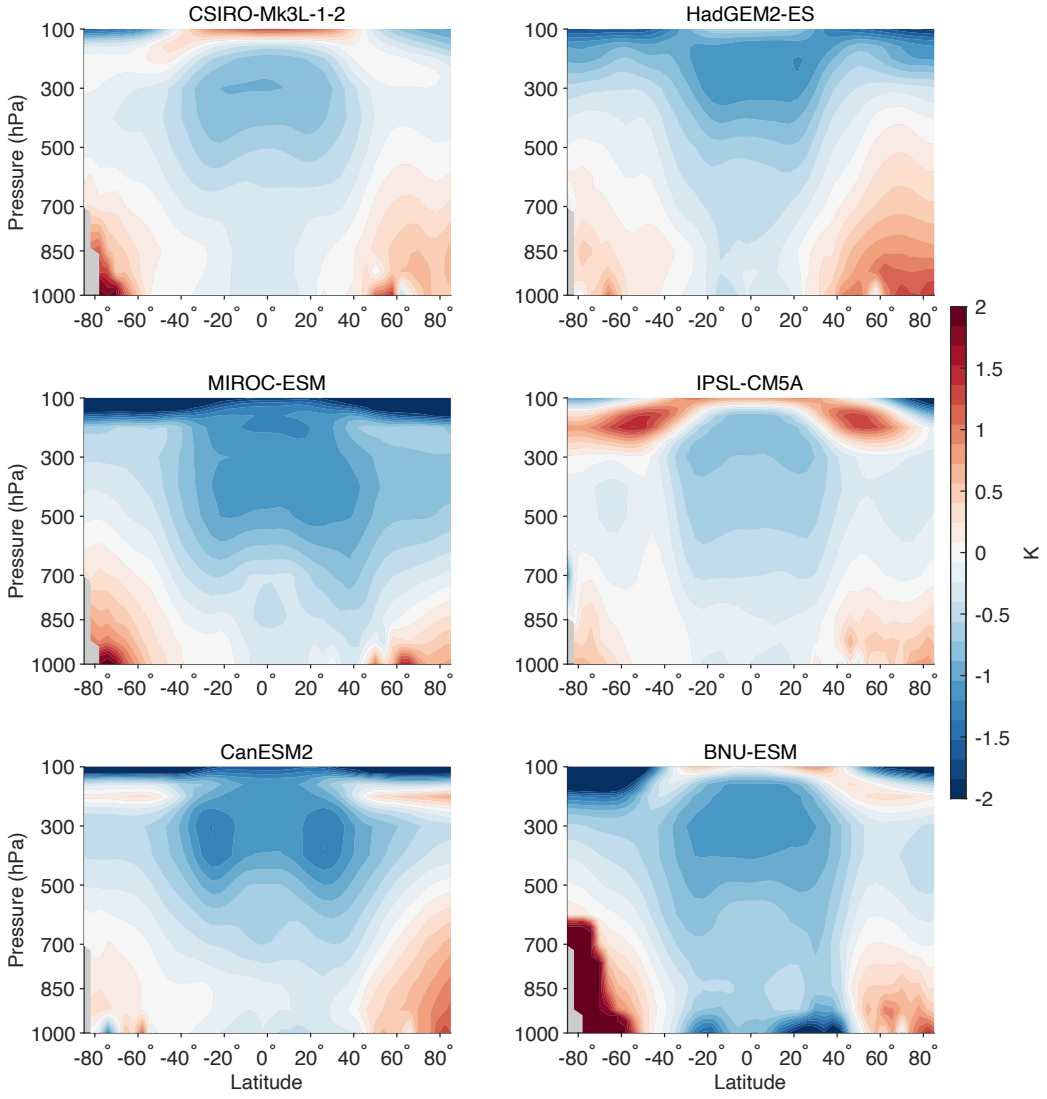

Figure 3-6: Zonal-mean temperature responses for G1 relative to PI in individual models. The colorbar is saturated in some regions.

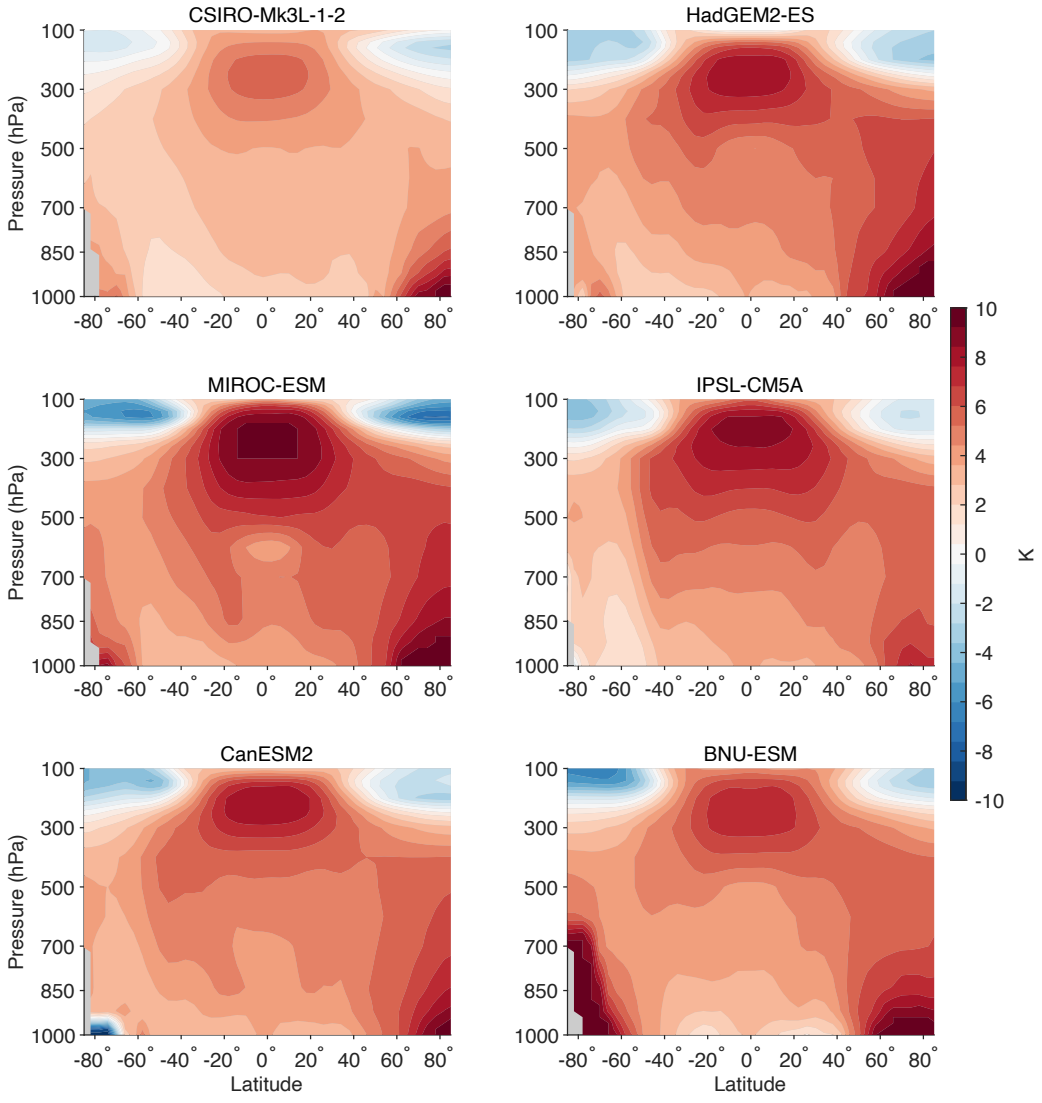

Figure 3-7: Zonal-mean temperature responses for 4xCO_2 relative to PI in individual models. The colorbar is saturated in some regions.

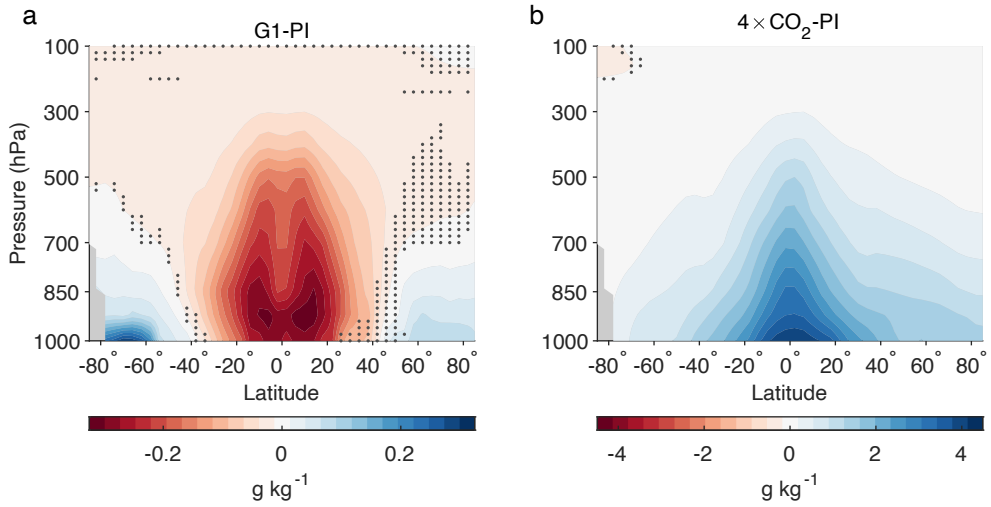

Figure 3-8: Model- and zonal-mean specific humidity responses relative to PI for (a) G1 and (b) 4xCO_2. Stippling indicates regions where fewer than five of six models agree on sign of change.

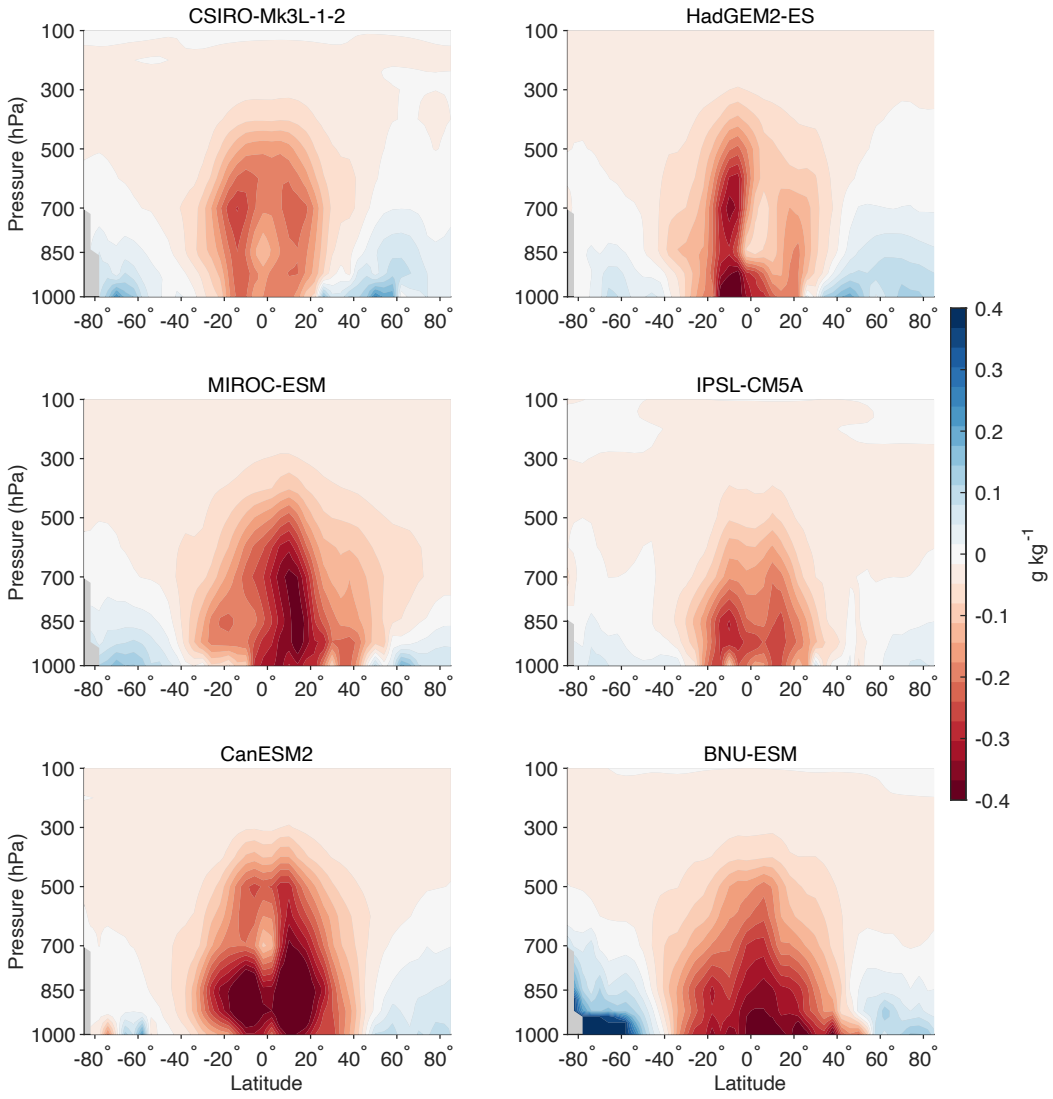

Figure 3-9: Zonal-mean specific humidity responses relative to PI for G1 in individual models. The colorbar is saturated in some regions.

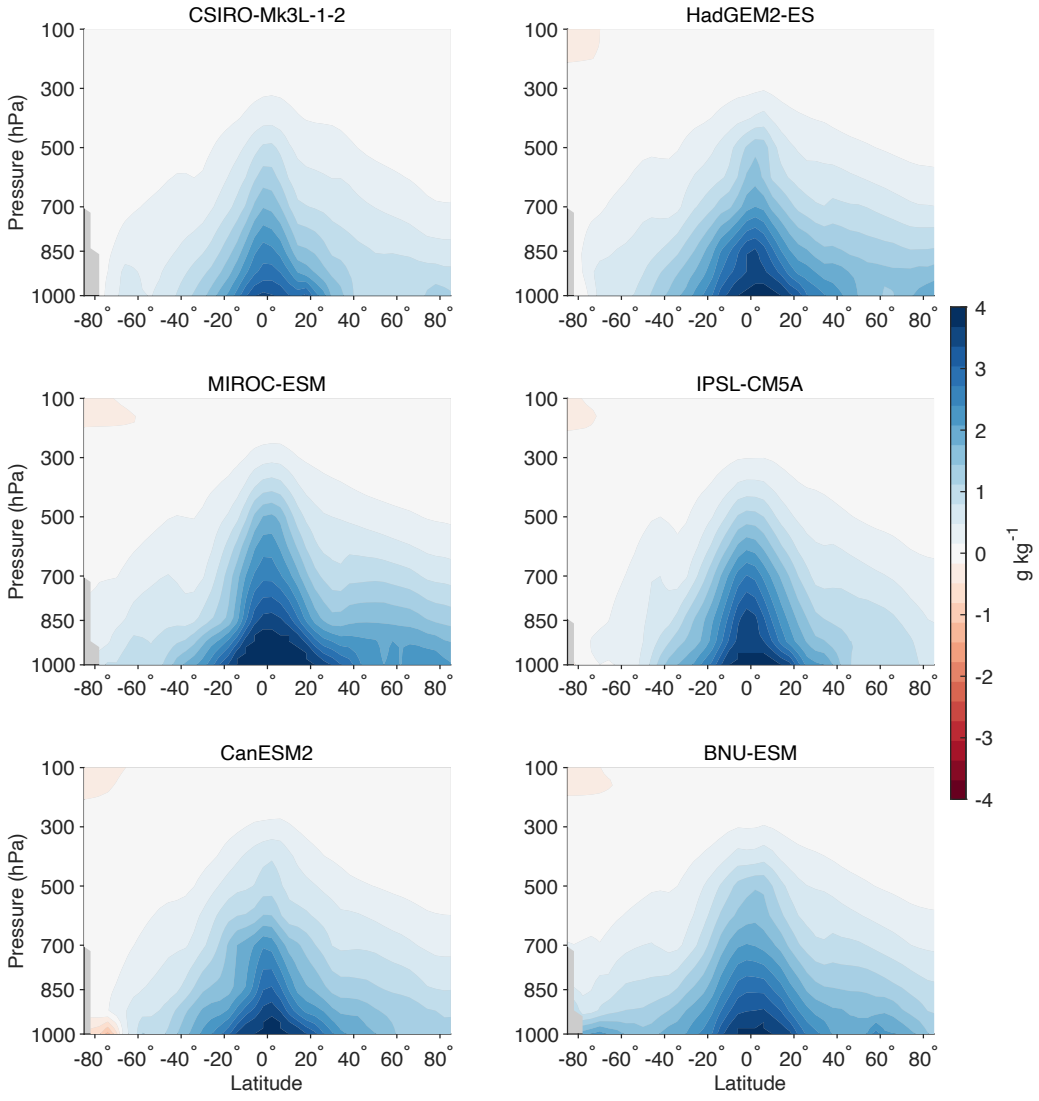

Figure 3-10: Zonal-mean specific humidity responses relative to PI for 4xCO_2 in individual models.

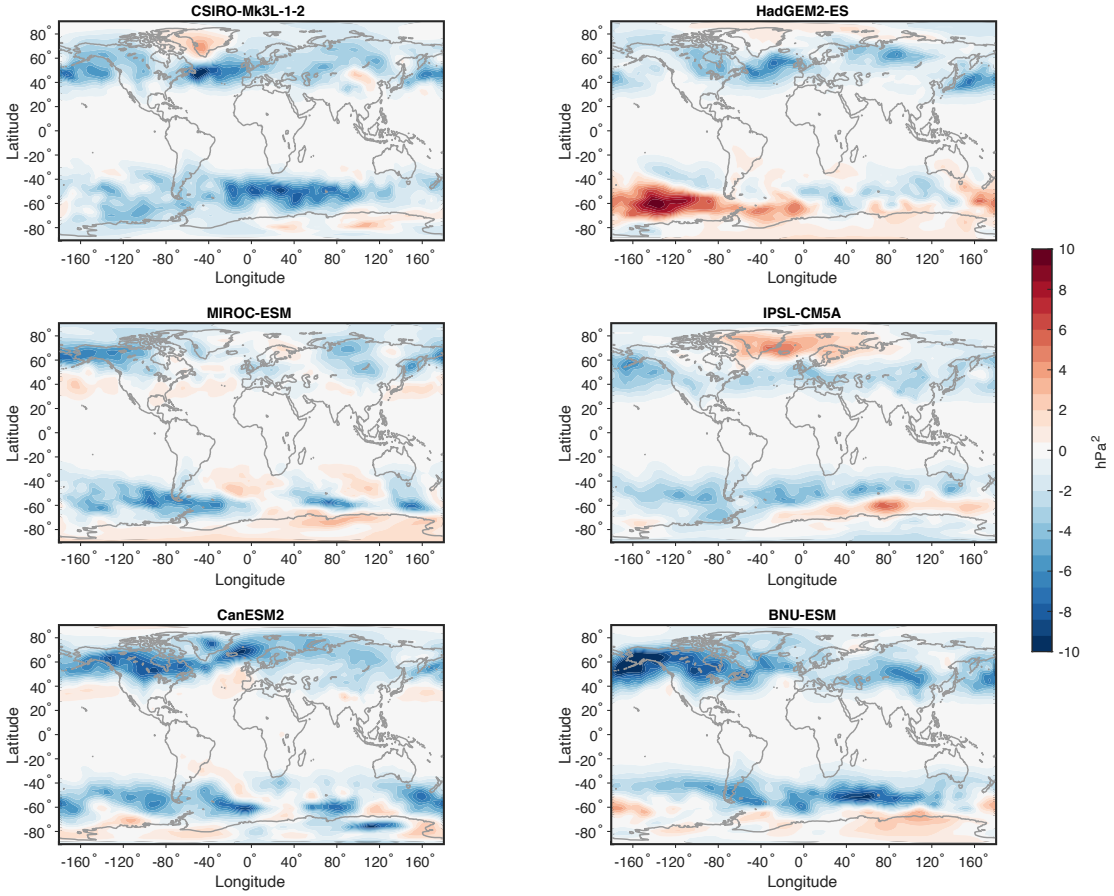

Figure 3-11: ECA responses for G1 relative to PI in individual models.

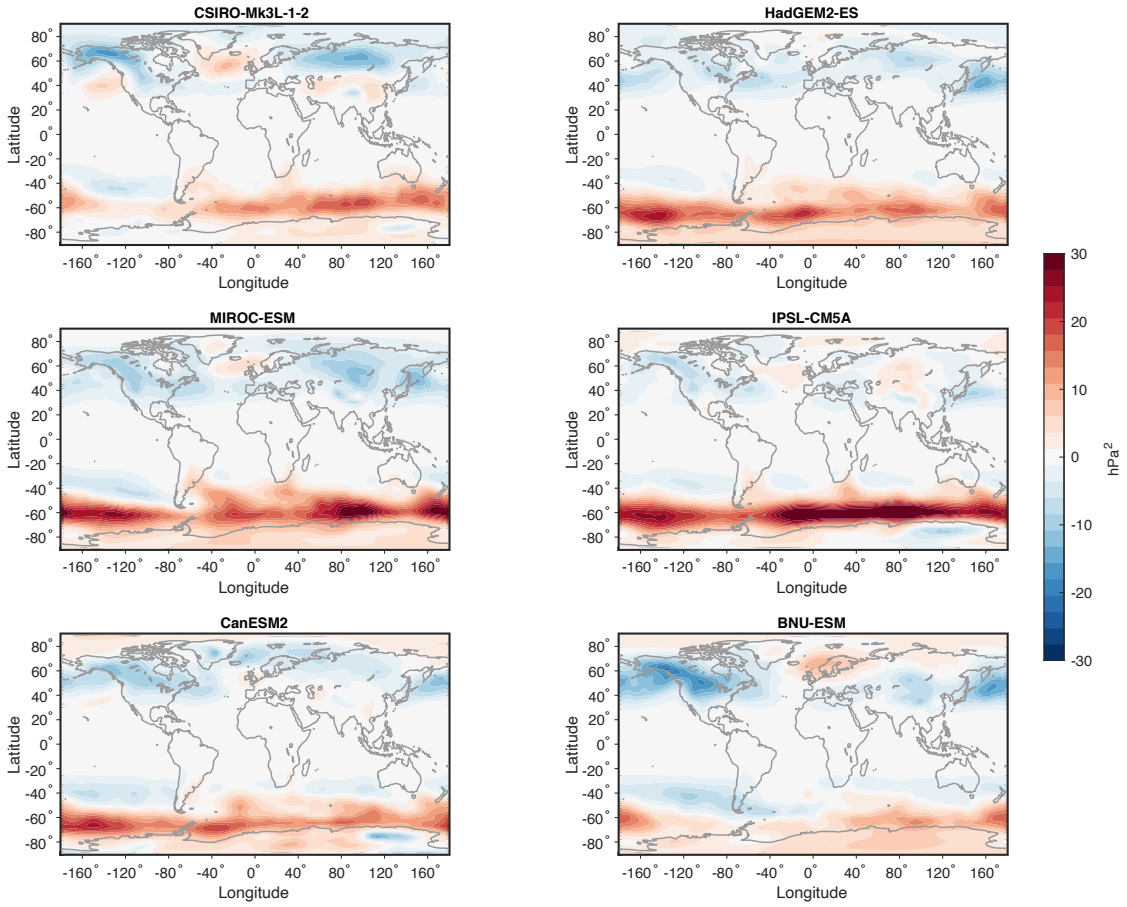

Figure 3-12: ECA responses for $4xCO_2$ relative to PI in individual models. The colorbar is saturated in some regions.

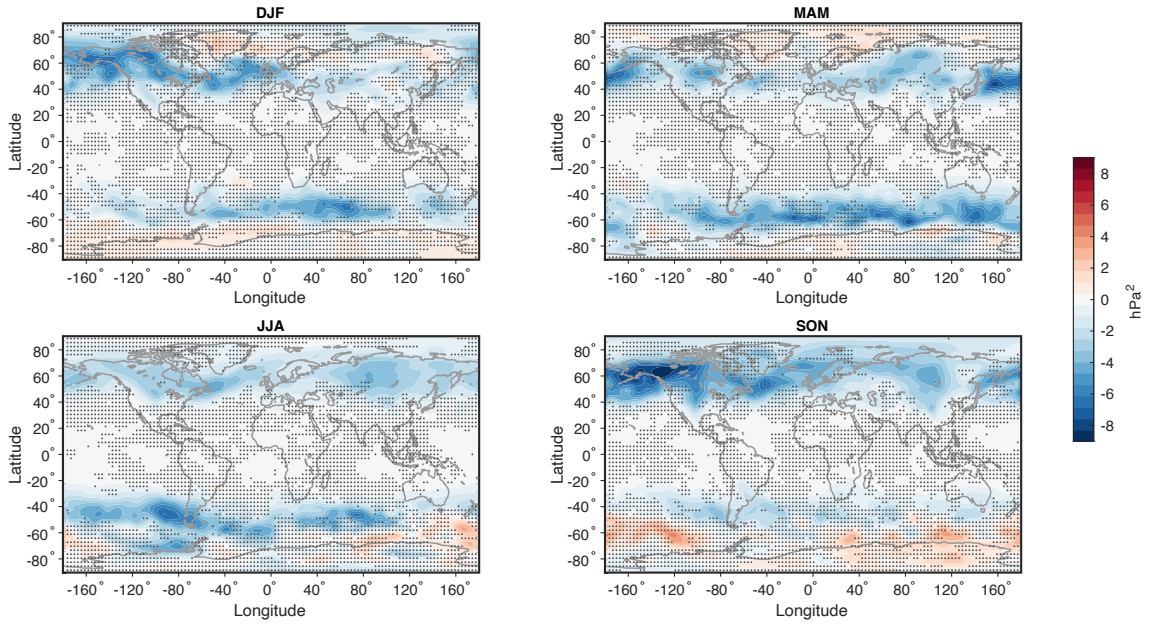

Figure 3-13: Model-mean ECA response for G1 relative to PI in December-January-February (DJF), March-April-May (MAM), June-July-August (JJA), and September-October-November (SON). Stippling indicates regions where fewer than five of six models agree on the sign of the response.

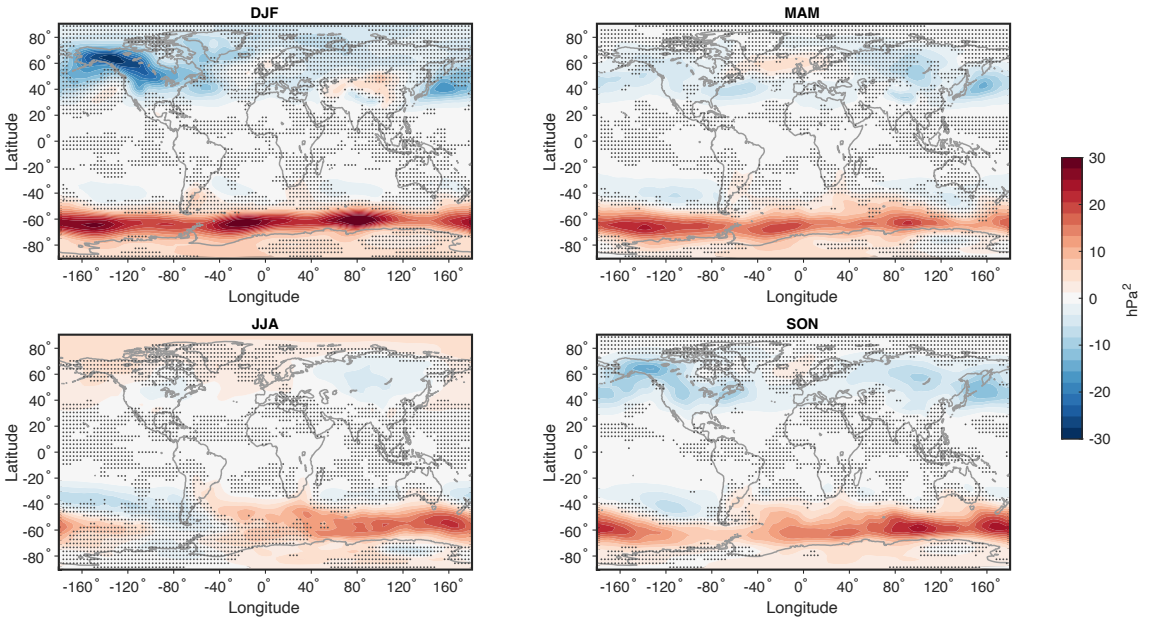

Figure 3-14: Model-mean ECA response for 4xCO$_2$ relative to PI in December-January-February (DJF), March-April-May (MAM), June-July-August (JJA), and September-October-November (SON). Stippling indicates regions where fewer than five of six models agree on the sign of the response.

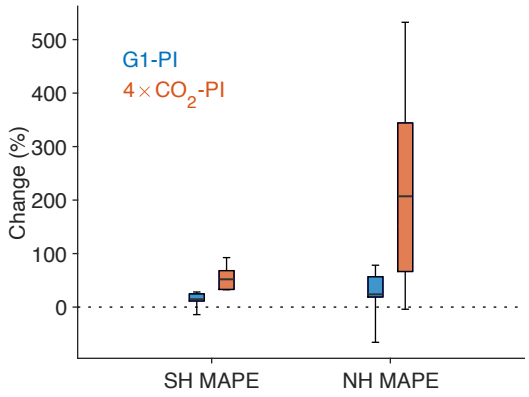

Figure 3-15: Fractional changes in convective MAPE for G1 (blue) and 4xCO$_2$ (red) relative to PI in the Southern Hemisphere (SH) and Northern Hemisphere (NH). Box indicates range of inner 4 models (second and fifth sextiles), whiskers indicate maximum and minimum values, and mid-lines indicate model mean values. All MAPE values shown are calculated over 30-70° latitude.

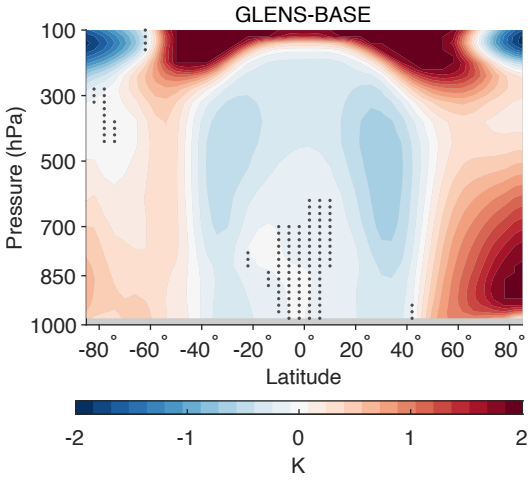

Figure 3-16: Ensemble- and zonal-mean temperature response for GLENS relative to BASE. Stippling indicates regions where fewer than five-sixths of ensemble members agree on the sign of the response. The colorbar is saturated in the lower stratosphere.

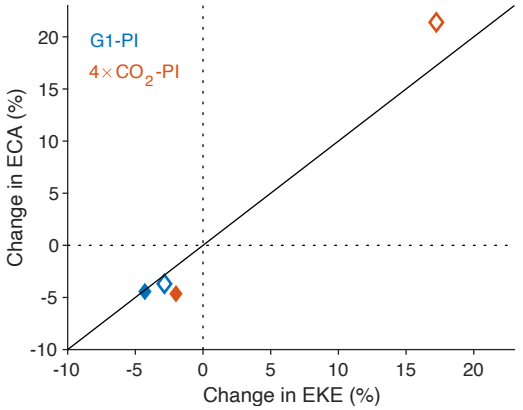

Figure 3-17: Changes in the IPSL-CM5A climate model for two different measures of extratropical storm track intensity. Shown are the fractional changes in ECA and EKE in experiment G1 (blue) and 4xCO2 (red) relative to PI for the Northern Hemisphere (filled symbols) and Southern Hemisphere (open symbols).

Chapter 4

Available potential energy of the three-dimensional mean state of the atmosphere and the thermodynamic potential for warm conveyor belts

Abstract: The impacts of changes in the mean state of the atmosphere on the high frequency weather events that dominate extratropical atmospheric circulation are uncertain. Here, I develop and employ a new method to calculate the mean available potential energy (MAPE) of the atmosphere and perform the first exact MAPE calculations in a three dimensional domain. A newly-developed eddy-size restriction, in conjunction with a partitioning of MAPE into convective and nonconvective components, allows for the identification of the thermodynamic potential for convective activity driven by large-scale overturning and ascent on the eddy length scale. I show that the maximum potential ascent relates strongly to the frequency of warm conveyor belts (WCBs), dynamic components of extratropical cyclones with large impacts on weather. This approach is also used to skillfully identify necessary thermodynamic

conditions for individual instances of WCB activity on shorter timescales. These advances are expected to be helpful to connect changes in the mean state of the climate, such as global warming, to important extratropical atmospheric dynamics.

4.1 Introduction

The extratropical atmospheric circulation is dominated by extratropical cyclones, baroclinic eddies that draw their energy from the mean available potential energy (MAPE) of the atmosphere. MAPE is the maximum amount of kinetic energy that could be released by reversible adiabatic motion, and is defined as the difference between the integrated enthalpy of the atmosphere's mean state and its reference state, the minimum-enthalpy state possible through reversible adiabatic rearrangements. A useful framework to connect the mean thermal structure of the atmosphere to the extratropical circulation, MAPE accounts for the competing effects of the static stability, meridional temperature gradients, and moisture content on the energy available to circulations including extratropical cyclones [38, 39]. Here, I also show that examination of the reference state provides insight into the thermodynamic potential for important components of extratropical circulation, like convection and warm conveyor belts (WCBs), that are associated with extratropical cyclones and influence weather in the midlatitudes.

In a variety of simulations of varying complexity, MAPE has been shown to scale linearly with the strength of the extratropical storm tracks, regions of enhanced incidence of extratropical cyclones. Schneider and Walker [68] and O'Gorman and Schneider [50] show that the strength of the extratropical storm track in a wide range of idealized simulations, as measured by eddy kinetic energy (EKE), scales linearly with dry MAPE, which neglects latent heating by assuming a specific humidity of zero. O'Gorman [49] demonstrates that EKE scales with moist MAPE, which accounts for latent heating, in a series of idealized global warming simulations. In more complex simulations, MAPE scales with the strength of the extratropical storm tracks over the forced climate changes of the seasonal cycle and global warming [48], as well as solar

geoengineering experiments [23]. In reanalysis and observational data, MAPE scales with Northern Hemisphere summertime EKE over observed global warming [22]. In targeted experiments with isolated thermal forcings, the relation between storm track strength and MAPE can break down, but it still performs better than considering changes in meridional temperature gradient or static stability alone [94]. This relation does not hold over all modes of unforced climate variability, and a baroclinic annular mode has been identified in the Southern Hemisphere in which EKE and baroclinic instability participate in a coupled oscillation and are anticorrelated on a 20-30 day timescale [83].

Lorenz [38] derives an approximate formulation of the available potential energy that uses global mean static stability, valid under an assumption of small isentropic slope. Oort et al. [51] use this formulation to calculate the approximate zonal-mean and eddy components of available potential energy, and find that the zonal-mean component dominates. This result is often used to justify the calculation of MAPE using only the zonal mean atmosphere. The introduction of moist MAPE [39] complicates the calculation of the reference state by including water content, a second conserved variable in addition to entropy, and including the effect of latent heating from phase change. Lorenz [40] introduces a parcel swapping algorithm to calculate the reference state of a moist atmosphere, in which a zonal-mean domain is divided into parcels along a staggered grid, reducing the problem to one dimension in pressure. This algorithm finds a low-enthalpy configuration of the moist atmospheric mean state, but does not always solve for the exact minimum-enthalpy state [58]. Randall and Wang [58] present a different algorithm for solving for a low-enthalpy state that succeeds in certain cases where Lorenz [40] fails, but similarly does not always solve for the exact minimum-enthalpy case [79]. Stansifer et al. [79] apply the Munkres algorithm to solve for the exact minimum enthalpy state, and also present a faster, albeit inexact divide-and-conquer algorithm, which performs well in most situations. In this chapter, I introduce another method to calculate exact MAPE that is faster than the Munkres algorithm.

MAPE can also be applied to ocean systems, in which the reference state is the

global minimum potential energy state. Hieronymus and Nycander [27] solve the ocean reference state exactly in three dimensions by framing the problem in such a way that it may be solved using the linear assignment algorithm. Su and Ingersoll [80] expand on this framework for the ocean to solve the same problem more quickly using the minimum cost flow algorithm. This chapter adopts the Su and Ingersoll [80] framing of the MAPE problem, and solves it for the atmosphere, presenting for the first time the exact three-dimensional reference state for the climatological atmosphere[1]. Further restrictions are also placed on the calculation to gain insight into the local thermodynamic drivers of convection and other deep ascent.

Dynamic restrictions may also be imposed on the reference state in a MAPE calculation. For instance, in the atmosphere, a "nonconvective" MAPE has been proposed which does not permit vertical reordering of air originating at a given latitude, thereby limiting the release of convective instability [48]. Both the parcel-swapping algorithm of Lorenz [40] and the divide-and-conquer algorithm of Stansifer et al. [79] have been successfully adapted to calculate nonconvective MAPE [48, 22]. Nonconvective MAPE is expected to scale more closely with EKE because it removes the generation of kinetic energy associated with convective instability that may not contribute to EKE on a coarse grid [48, 22, 23]. A corollary to nonconvective MAPE, convective MAPE has been defined as the difference between MAPE and nonconvective MAPE, and is interpreted as the energy available for moist convection driven by large-scale circulations [22].

In the ocean, an eddy-size restricted MAPE has been proposed in which no parcel may be displaced by a horizontal distance larger than the local eddy size [80], meaning the parcel rearrangements to determine the minimum potential energy state may not exceed the local eddy size. Unlike the domain-wide optimization of the full MAPE calculation, the proposed eddy-size restricted MAPE identifies baroclinically unstable regions; baroclinic eddies are generated by local parcel movement at the eddy length scale. The spatial patterns of EKE in the ocean are similar to patterns of eddy-size

[1]The three-dimensional reference state for the climatological atmosphere is exact up to approximations in the moist thermodynamics, such as the treatment of ice.

restricted available potential energy density, the positive definite work done against buoyancy forces when displacing parcels from the reference state to the mean state [81]. In this chapter I will introduce a new eddy-size restricted scheme to calculate MAPE for the atmosphere.

One further application of an eddy-size restricted atmospheric MAPE is to provide insight into the dynamics of baroclinic instability. Here, I also investigate the predicted ascent of the parcel rearrangements for the eddy-size restricted MAPE calculations of the atmosphere, and compare it to WCBs, regions of actually observed ascent associated with extratropical cyclones. WCBs are strongly ascending air streams that originate in the atmospheric boundary layer in the warm sector of an extratropical cyclone and typically move polewards while ascending to levels near the tropopause. They play a large role in cloud and precipitation formation [7], transport sensible and latent heat poleward [7], and are responsible for a large portion of extreme precipitation events in certain regions [55]. WCBs are identified through a Lagrangian approach based on trajectory calculations and a selection criteria, described in detail in Madonna et al. [42], in which trajectories in the vicinity of an extratropical cyclone exhibiting ascent exceeding 600 hPa within 2 days are considered WCBs. I demonstrate below that the regions of large ascent between the reference state and the mean state correspond to areas of WCB ascent found in previous climatologies.

The chapter proceeds as follows. In Section 4.2, I describe the methods used to calculate the three-dimensional MAPE of the atmosphere and discuss imposing nonconvective and eddy-size restrictions. In Section 4.3, I present calculations of three-dimensional atmospheric MAPE under varying restrictions. For a discussion of the sensitivity of these calculations to major parameters, see Section 4.8. In Section 4.4, I relate the predicted ascent in nonconvective eddy-size restricted MAPE calculations to a WCB climatology and daily WCB activity. In Section 4.5, I discuss the results, present brief conclusions, and propose avenues for future work.

4.2 Calculating MAPE

Various exact methods to determine the minimum enthalpy state given an initial mean state of the atmosphere have been developed, although, as noted, they have to date considered only the two-dimensional zonal mean atmosphere. In this section, I describe the methods used to calculate the minimum enthalpy state of the three-dimensional atmosphere. I also discuss how to impose two extra constraints on the minimum enthalpy calculation. The first, nonconvective MAPE, restricts the release of convective instability, and the second, an eddy-size restricted MAPE, restricts parcel rearrangement to a distance equivalent to the characteristic eddy length scale.

4.2.1 Creating a Uniform Grid

To facilitate an optimized parcel rearrangement, the domain is divided into parcels of equal mass using a method for uniform grids on a sphere presented in Rosca [64]. Previously, for the atmosphere, the zonal-mean domain was divided into equal mass parcels by using uniform spacing in a cosine-weighted latitude coordinate to give equal area divisions in the horizontal, and uniform spacing in pressure [40, 48, 22, 23]. Some methods employ a staggered grid in pressure which reduces the problem to one dimension in pressure [40, 48, 22], but it is equally simple to employ consistent pressure coordinates in each column, which I do here. However, when cosine-weighted latitude coordinates were employed with the same number of longitudinal coordinates at each latitude for a three-dimensional calculation, grid cells acquired widely varying aspect ratios as the grid nears the polar regions. Instead, I employ the uniform grid described in full detail in 4.6 and equal divisions in pressure in each column. An example of such a grid can be seen in Figure 4-1.

4.2.2 Determining the Minimum-Enthalpy (Reference) State

Following Su and Ingersoll [80], but adapting to the atmosphere, I consider n parcels of equal mass M, each with an initial temperature (T), pressure (p), and relative humidity (r). The parcels can occur at s distinct pressure levels, each with a unique

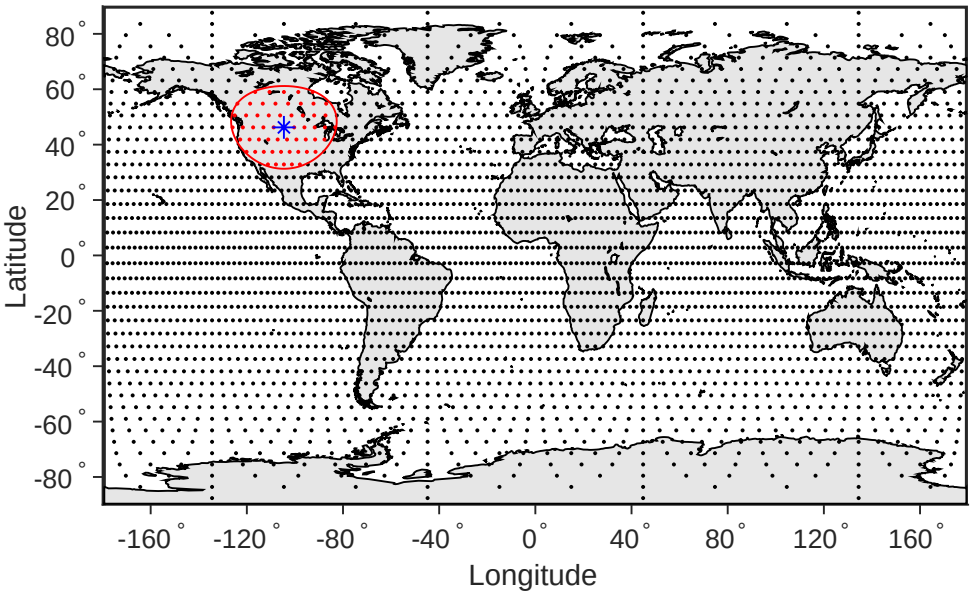

Figure 4-1: Uniform global grid example, created using the methodology introduced in Rosca [64]. The surface is divided into 3200 coordinates, with a 40×40 grid in each hemisphere. The red circle represents an example subdomain for the eddy-size restricted calculation with a radius of 15 arc-degrees (1670 kilometers), centered on the coordinate marked with a blue asterisk, and including all points colored in red.

pressure value (p_k^L), where $k = 1, 2, ..., s$. The number of parcels at each level is denoted by m_k, and m_k varies by level due to surface topography. Note that, by construction, $\sum_{k=1}^{s} m_k = n$. A matrix is defined which contains the enthalpy values of all parcels adiabatically and reversibly displaced to every pressure level, $\boldsymbol{h} = [h_{i,k}](i = 1, 2, ..., n; k = 1, 2, ..., s)$, where $h_{i,k}(T_i, p_i, r_i)$ is the enthalpy of parcel i at pressure p_k^L in joules per kilogram. In calculating the enthalpy of parcels at different pressures, I use the saturation vapor pressure formulae over ice and liquid described in Simmons et al. [75], but follow Wang and Randall [89] to merge ice and liquid phases. I then define the binary matrix $\boldsymbol{x} = [x_{i,k}](i = 1, 2, ..., n; k = 1, 2, ..., s)$ that maps the mean state onto the reference state, where $x_{i,k} = 0$ or 1, and $x_{i,k} = 1$ represents parcel i located at pressure p_k^L. Each rearrangement state has a unique $\boldsymbol{x}$ matrix, and the total enthalpy of the reference state is $M \sum_{i=1}^{n} \sum_{k=1}^{s} h_{i,k} x_{i,k}$. The sum over each row of $\boldsymbol{x}$ must equal one, to ensure that each parcel is only assigned one location in the rearrangement state, and the sum over each column of $\boldsymbol{x}$ must be the same as the number of parcels at the corresponding pressure level (m_k). Therefore, to solve for the reference state, one finds $\boldsymbol{x}$ which minimizes the total enthalpy given these conditions. The problem can be stated as follows:

$$\text{Given an } n \times s \text{ matrix } \boldsymbol{h}, \text{ find } n \times s \text{ matrix } \boldsymbol{x}, \text{ to minimize } \sum_{i=1}^{n} \sum_{k=1}^{s} h_{i,k} x_{i,k},$$
$$\text{where } x_{i,k} = 0 \text{ or } 1, \text{ subject to } \sum_{k=1}^{s} x_{i,k} = 1 \text{ for any } i \text{ and } \sum_{i=1}^{n} x_{i,k} = m_k \text{ for any } k \tag{4.1}$$

Su and Ingersoll [80] recognize that this problem belongs to the minimum-cost flow problem in applied mathematics, and solve it efficiently using the minimum-cost flow algorithm. This problem may also be formulated as an integer linear programming problem, and I solve it here using a standard implementation of the dual-simplex algorithm. To frame the problem for integer linear programming, the $\boldsymbol{h}$ and $\boldsymbol{x}$ matrices are vectorized to $\boldsymbol{h_{vec}}$ and $\boldsymbol{x_{vec}}$, and I minimize $\boldsymbol{h_{vec}} \cdot \boldsymbol{x_{vec}}$ over $\boldsymbol{x_{vec}}$, subject to the constraint that $\boldsymbol{A} \cdot \boldsymbol{x_{vec}} = \boldsymbol{b}$, $\boldsymbol{A}$ and $\boldsymbol{b}$ being a matrix and vector, respectively, that express the constraints in (4.1).

The minimum enthalpy state is also solved for using the divide-and-conquer algorithm described in Stansifer et al. [79]. While the divide-and-conquer algorithm is slower than the integer linear programming approach, it more easily accommodates the nonconvective condition imposed on the parcel rearrangement described below. The divide-and-conquer algorithm is a recursive algorithm that builds a low-enthalpy reference state by dividing the atmospheric domain into smaller subdomains. At each division, the pressure-derivative of enthalpy in the middle of the subdomain is used to order parcels within that subdomain from top to bottom, and then the top and bottom halves are assigned to new subdomains. I use the same moist thermodynamic formulation as for the integer linear programming implementation described above.

4.2.3 Nonconvective Condition

As discussed above, a reference state may be calculated under the condition that parcels originating in a given column may not change their vertical ordering, thereby restricting the release of convective instability. While the reference pressure for the minimum enthalpy state of the zonal-mean atmosphere for the moist MAPE calculation shows a convective "bubble" that ascends discontinuously to the upper troposphere, in a nonconvective calculation the reference pressure is always continuous, as seen in Figure 2-2. A similar area of low-latitude ascent in the moist MAPE calculation can be seen in Figure 4-2 of this chapter, resolved in latitude and longitude. The nonconvective MAPE is defined here as the difference between the integrated enthalpy of the mean state and the enthalpy of the reference state restricted in this way. I define the convective MAPE as the difference between the MAPE and the nonconvective MAPE.

To calculate nonconvective MAPE using the divide-and-conquer algorithm, the algorithm is simply modified such that at each step of the recursion, parcels from a given initial latitude may not change their vertical ordering in the reordering of the subdomain. This ensures a continuous reordering in which parcels may not "leapfrog" in pressure over parcels from the same initial column, and the reference pressure is a monotonic function of pressure in a given column. It is also possible in some but

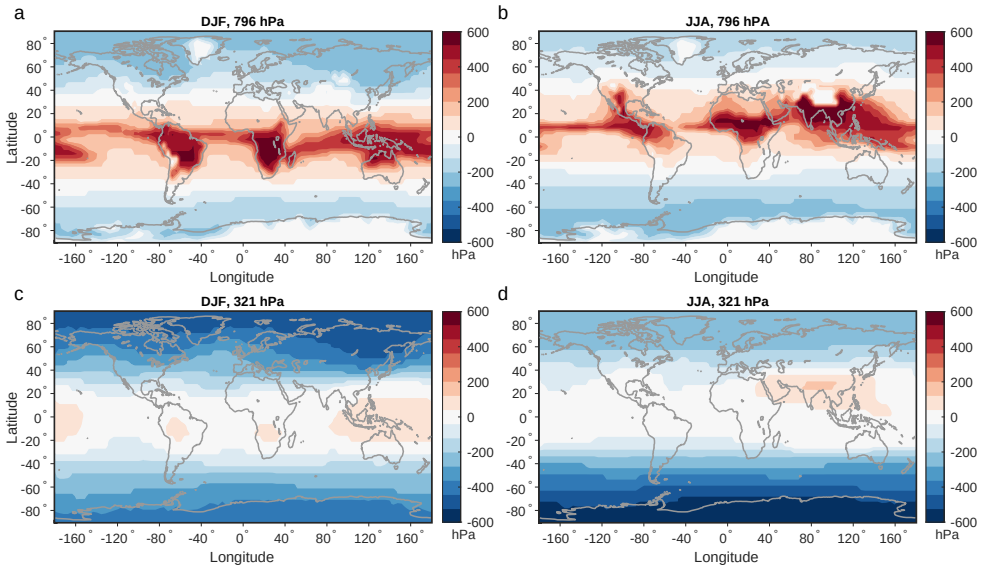

Figure 4-2: Visualization of three-dimensional MAPE calculation. Shown are the differences in original pressure and reference pressure for parcels originating at 796 hPa (a, b) and 321 hPa (c, d) for DJF (a, c) and JJA (b, d). MAPE is calculated using 3200 equal-area surface coordinates (a 40×40 grid in each hemisphere), and 15 evenly spaced pressure levels from the surface to 50 hPa. Positive values imply ascent from the mean state to the reference state, and negative values imply descent from the mean state to the reference state.

not all cases to calculate the nonconvective MAPE using integer linear programming, which I describe in Section 4.7. Here, the divide-and-conquer algorithm is used when calculating the nonconvective MAPE for its consistent performance.

4.2.4 Eddy-Size Restriction

Here, I define a local MAPE framework under the restriction that a parcel may not be displaced horizontally by a distance greater than the characteristic length scale of baroclinic eddies in the atmosphere. Su and Ingersoll [80] define an eddy-size restricted MAPE for the ocean in which a single global minimum is found given this constraint on individual parcels, and plot the available potential energy density. When this approach is used for the atmosphere, the global optimization is dominated by ascent in the tropics. Instead, here a series of MAPE calculations are performed within domains restricted by the eddy length scale. This approach captures the local energy available to extratropical cyclones on the eddy length scale, but does not account for the horizontal energy fluxes into and out of these systems, in particular so-called downstream development [11].

The atmosphere is divided into parcels of equal mass as before, using a uniform grid on the sphere and equal divisions in pressure. At each gridpoint, only parcels that fall within a horizontal distance less than some defined eddy length scale, l, are included in the MAPE calculation. The MAPE at a given coordinate is defined as the MAPE over the subdomain centered on that coordinate. An example of such a subdomain is shown in Figure 4-1. I consider both MAPE and its nonconvective and convective components of each subdomain, and all information about each individual calculation is recorded, including the MAPE value and the reference pressure of the parcels included within that calculation.

4.2.5 Data

The following MAPE calculations and comparisons to meteorological fields are performed using the ERA-Interim reanalysis dataset, a global atmospheric reanalysis pro-

duced by the European Center for Medium-Range Weather Forecasts [17]. Monthly temperature, relative humidity, wind, and surface pressure data are used at a horizontal grid spacing of 0.75° by 0.75°, and are used for all calculations on time scales longer than one month. Six-hourly temperature, relative humidity, wind, and surface pressure are accessed at a horizontal grid spacing of 2.5° by 2.5° for calculations on shorter time scales. Unless otherwise noted, all fields are from 1979 to 2018 and data at pressure levels below surface pressure are removed.

In addition, I use the WCB climatology developed by Madonna et al. [42] based on Lagrangian trajectories calculated from ERA-Interim wind data, which has been extended in time since publication to cover the time period 1979-2018. WCB trajectories are identified as strongly ascending air parcels (600 hPa in 2 days) near extratropical cyclones.

4.3 Three-Dimensional MAPE of the Atmosphere

4.3.1 MAPE of the Mean Atmosphere

The climatological seasonal MAPE over 1979-2018 can be seen in Table 4.1 for the northern and southern extratropical regions (20° -90° latitude), as well as the global domain. To calculate the three-dimensional MAPE, the global domain is divided into equal-mass parcels using 3200 equal-area coordinates (a 40×40 grid in each hemisphere), and 15 evenly spaced pressure levels from the surface to 50 hPa. The results are generally similar beyond a resolution of about 800 surface coordinates and 10 pressure levels. The coordinates in this global grid that fall within the domains of interest are used to calculate the MAPE. A zonal-mean MAPE on the same domain is also calculated, in which all temperature and humidity values are replaced by the zonal mean values at that latitude and pressure.

As expected, the three-dimensional MAPE is always larger than the zonal-mean MAPE, as it accounts for both zonal-mean and eddy components (4.1). The difference between the three-dimensional MAPE and the zonal-mean MAPE, which can be

Table 4.1: Extratropical and global seasonal MAPE values in J kg^{-1} for 1979-2018. Zonal-mean MAPE is calculated by replacing all values for temperature and humidity at a given latitude and pressure with the zonal-mean values at that latitude and pressure. Difference is calculated as the change from three-dimensional MAPE to the zonal-mean MAPE, as a percentage of the three-dimensional MAPE. All MAPE values are calculated using integer linear programming.

Season	Domain	MAPE	Zonal-Mean MAPE	Difference (%)
DJF	20°-90° N	373.6	335.3	-10.2
	20°-90° S	301.2	284.1	-5.6
	90° S -90° N	480.4	452.8	-5.7
MAM	20°-90° N	303.0	285.5	-5.8
	20°-90° S	333.0	324.7	-2.5
	90° S -90° N	450.6	435.9	-3.3
JJA	20°-90° N	215.2	166.8	-22.5
	20°-90° S	361.0	351.1	-2.8
	90° S -90° N	433.8	407.6	-6.1
SON	20°-90° N	324.8	305.7	-5.9
	20°-90° S	341.8	330.1	-3.4
	90° S -90° N	443.2	423.3	-4.5

interpreted as the contribution to overall MAPE that comes from zonal asymmetries, is always largest in the Northern Hemisphere extratropics, with particularly large contributions in DJF and JJA. Figure 4-2 shows the difference between the original pressure of parcels and their reference pressures on two levels for the three-dimensional MAPE calculation in JJA and DJF. The zonally-varying pattern is characterized by tropical and subtropical ascent and extratropical descent. Tropical and subtropical ascent is strongest at the lower levels in the summer hemisphere and over land, and extratropical descent is strongest at the upper levels in the winter hemisphere.

Nonconvective MAPE and convective MAPE are presented in Table 4.2, calculated using the divide-and-conquer algorithm, but on a lower resolution domain due to the computational intensity. Here, the global domain is divided into equal mass parcels using 800 equal-area coordinates (a 20×20 grid in each hemisphere), and 15 evenly spaced pressure levels from the surface to 50 hPa. The MAPE values in the three-dimensional calculation and the zonal-mean calculation (not shown) using divide and conquer are very similar to those from the higher-resolution, exact calculation using

Table 4.2: Extratropical seasonal full, nonconvective, and convective MAPE values in J kg^{-1} for 1979-2018. All MAPE values are calculated using divide-and-conquer algorithm at lower resolution than Table 4.1 (see text for details). Convective fraction shown in parentheses as a percentage of MAPE.

Season	Domain	MAPE	Nonconvective MAPE	Convective MAPE
DJF	20°-90° N	372.5	366.9	5.7 (1.5%)
	20°-90° S	300.7	285.2	15.4 (5.1%)
MAM	20°-90° N	303.8	296.1	7.7 (2.5%)
	20°-90° S	333.2	318.8	14.4 (4.3%)
JJA	20°-90° N	216.7	197.3	19.4 (9.0%)
	20°-90° S	359.1	353.4	5.7 (1.6%)
SON	20°-90° N	326.1	309.8	16.4 (5.0%)
	20°-90° S	341.4	335.8	5.6 (1.7%)

integer linear programming in Table 4.1. Convective MAPE is largest in Northern Hemisphere JJA, when it is also the largest percentage of overall MAPE. The convective MAPE in Southern Hemisphere DJF, Southern Hemisphere MAM, and Northern Hemisphere SON are comparable, and larger than the remaining seasons and hemispheres. The relative breakdowns between convective and nonconvective MAPE in the zonal mean (not shown) are again very similar.

4.3.2 Eddy-Size Restricted MAPE

Next the eddy-size restriction is imposed on the MAPE calculation. Using the same grid as before, the global domain is divided into equal-mass parcels using 3200 equal-area coordinates (a 40×40 grid in each hemisphere), and 15 evenly spaced pressure levels from the surface to 50 hPa. Each subdomain is centered on one surface coordinate and has a radius of 15 arc-degrees (1670 kilometers). This radius was chosen as generally representative of the length scale of midlatitude eddies, and this resolution was chosen for its relative speed and accuracy. For a discussion of the eddy-size restricted MAPE sensitivity to key parameters, see Section 4.8.

The eddy-size restricted three-dimensional MAPE of the climatological (1979-2018) atmosphere is shown in Figure 4-3. Local values of MAPE represent the energy

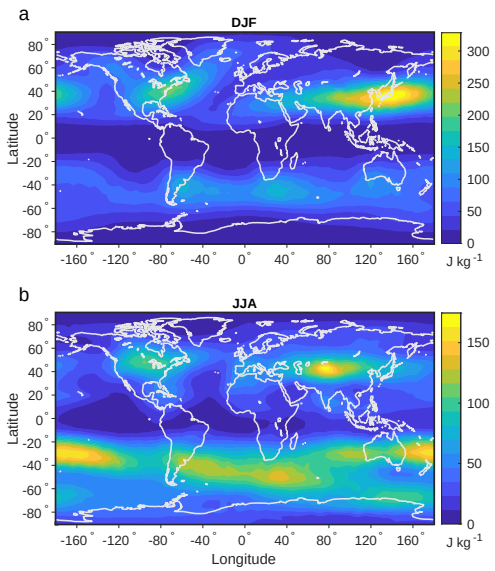

Figure 4-3: Seasonal eddy-size restricted MAPE of the 1979-2018 climatological atmosphere for December-January-February (a, DJF) and June-July-August (b, JJA). MAPE is calculated on subdomains of radius 15 arc-degrees (1670 kilometers) centered on 3200 equal-area surface coordinates (a 40×40 grid in each hemisphere), and 15 evenly spaced pressure levels from the surface to 50 hPa.

available for local parcel rearrangement at the eddy length scale, and thus baroclinically unstable regions. The baroclinically unstable regions occur, as expected, most strongly in the extratropical regions. Land-sea boundaries on the eastern sides of continents are particular hotspots. Northern Hemisphere winter shows the highest overall values in the Western Pacific, while Southern Hemisphere winter has more consistently high values across the domain.

The reference pressure may be examined for each subdomain for insight into the characteristics of these rearrangements. For example, the difference between the original pressure of a parcel and the reference pressure of the same parcel can be considered the ascent or descent that gives rise to the potentially largest energy release on the eddy length scale. In the eddy-size restricted approach, the parcels above each surface coordinate are included in multiple MAPE calculations for subdomains that overlap with that surface coordinate, and the maximum ascent of any parcel over all subdomains that include that surface coordinate can be thought of as the maximum

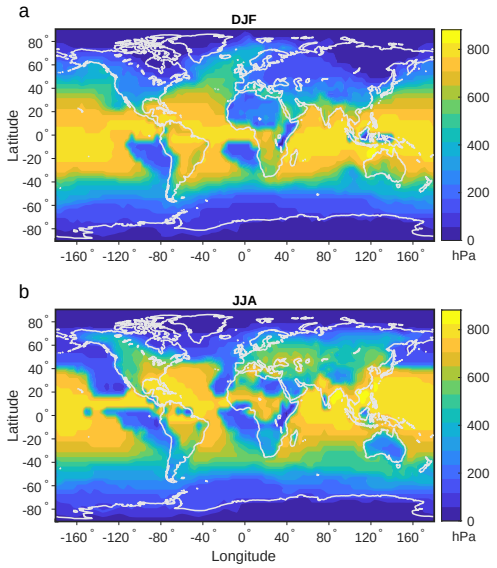

Figure 4-4: Maximum potential ascent in the seasonal eddy-size restricted MAPE of the 1979-2018 climatological atmosphere for December-January-February (a, DJF) and June-July-August (b, JJA). MAPE is calculated as in Figure 4-3. Maximum potential ascent is calculated at each coordinate as the maximum difference between pressure and reference pressure for any parcel in the column over all the MAPE calculations that include that column.

potential ascent due to baroclinic instability. Figure 4-4 shows distinct patterns of maximum potential ascent in each season, with maximum values near the equator, and the highest values over land outside of the tropics in the summer hemisphere. This is largely potential convective ascent, and below the nonconvective and convective components are examined independently.

4.3.3 Nonconvective and Convective Eddy-Size Restricted MAPE

Nonconvective MAPE

The nonconvective eddy-size restricted MAPE is also calculated using the same grid and subdomain dimensions as the full eddy-size restricted MAPE, but using the divide-and-conquer algorithm rather than integer linear programming. As the nonconvective MAPE restricts convective reordering of parcels, and therefore does not

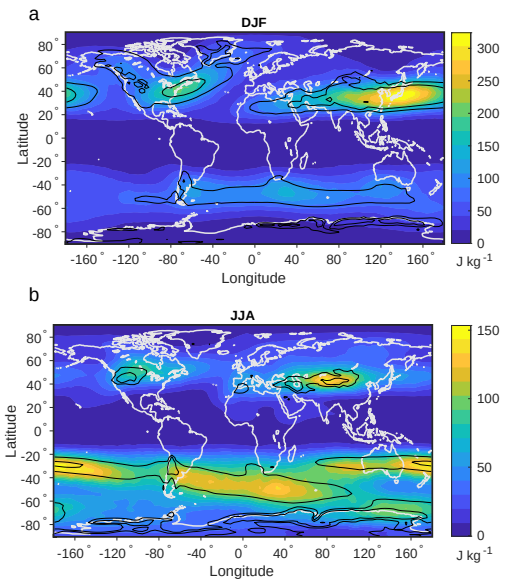

Figure 4-5: Seasonal nonconvective eddy-size restricted MAPE (color contours) and Eady growth rate (Equation 4.2) averaged over 500-750 hPa (black contours) of the 1979-2018 climatological atmosphere for December-January-February (a, DJF) and June-July-August (b, JJA). MAPE is calculated using the same domains as in Figure 4-3, without permitting convection. Black contours are 0.5 day^{-1} and 0.7 day^{-1}.

permit generation of kinetic energy associated with convective instability, it is expected to follow large-scale eddy activity more closely. Figure 4-5 demonstrates that the overall pattern and magnitudes of MAPE and nonconvective MAPE in Figure 4-3 are generally similar in each season, while the nonconvective MAPE is always equal or smaller in magnitude.

When compared to a standard metric of baroclinic instability, the Eady growth rate, nonconvective MAPE is shown to capture very similar structural features of the baroclinicity of the atmosphere. The Eady growth rate, σ, is defined as:

$$\sigma = 0.31 \frac{f}{N} \left\| \frac{\partial \mathbf{u_h}}{\partial z} \right\| \tag{4.2}$$

where f is the Coriolis parameter, N is the Brunt-Väisälä buoyancy frequency, $\mathbf{u_h}$ is the horizontal wind, and z is height. Here, the average Eady growth rate over the 500-750 hPa levels is used. This suggests that the eddy-size restricted nonconvective MAPE is a useful metric of baroclinicity and is complementary to the Eady growth

rate, but includes moisture.

Convective MAPE

The convective eddy-size restricted MAPE is also calculated, defined above as the difference between full eddy-size restricted MAPE and nonconvective eddy-size restricted MAPE (Figure 4-6). The full eddy-size restricted MAPE calculated using the divide-and-conquer algorithm gives some negative values near the equator, which is physically impossible, but is known to occur in certain cases with the divide-and-conquer algorithm [25] (see Appendix C, Section 4.8.3, Figure 4-14). Thus, integer linear programming is used to calculate the full eddy-size restricted MAPE, but results are similar regardless of approach (see Section 4.8.3). The convective eddy-size restricted MAPE is interpreted as a local measure of the energy available for convection associated with baroclinic eddies in the atmosphere. To compare it to known metrics of convection in the atmosphere, the convective available potential energy (CAPE) of six-hourly atmospheric temperature and humidity fields is calculated, using the same moist thermodynamics as in the MAPE calculation. CAPE is defined as the positive energy released by a surface air parcel lifted through the atmosphere from the level of free convection to the level of neutral buoyancy [20].

The 95^{th} percentile of six-hourly CAPE is plotted in Figure 4-6 over the same time period as the climatological convective MAPE, comparing a quantity derived from instantaneous values to a quantity derived from the mean state of the atmosphere. Figure 4-6 demonstrates that in some ways convective MAPE follows similar contours as higher percentiles of CAPE, but exhibits a local minimum near the equator which is not present in CAPE. This is possibly due to the distinction that convective MAPE represents the convection associated with large-scale circulations driven by horizontal temperature gradients, which are also minimized near the equator. Though there is a strong signal of convective maximum potential ascent near the equator, this does not seem to contribute to the convective MAPE centered at the equator. When the maximum potential ascent is reported at the center of the domain in which it occurs, instead of the location at which it occurs, a strong tropical signal of potential ascent

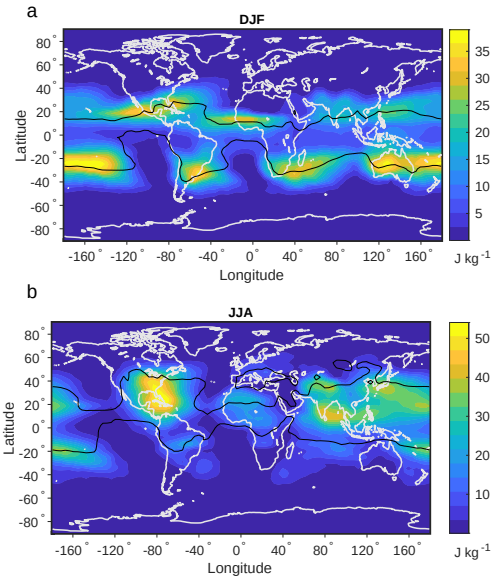

Figure 4-6: Seasonal convective eddy-size restricted MAPE (color contours) of the climatological atmosphere and 95^{th} percentile of six-hourly CAPE (black contours) in 1979-2018 for December-January-February (a, DJF) and June-July-August (b, JJA). Convective MAPE is calculated as the difference in MAPE and nonconvective MAPE, using the same domains as in Figure 4-3. Black contours are 1500 J kg^{-1}.

still exists. However, large displacements in the vertical do not imply large generation of kinetic energy if the buoyancy is low, explaining how convective MAPE values can remain small in that region. More work is needed to specifically connect convective MAPE to instantaneous atmospheric convection.

4.4 Application to Warm Conveyor Belts

4.4.1 Climatological Maximum Potential Ascent and WCBs

The potential ascent determined by a local MAPE framework should provide insight into WCB activity, as WCBs represent atmospheric ascent associated with extratropical cyclones. High resolution modeling experiments suggest that, while some WCBs trajectories may include convective ascent, the more common, winter-type WCBs are mostly nonconvective and slantwise in nature [59, 46, 47]. Therefore, it seems more likely that potential ascent from nonconvective MAPE rather than full MAPE would

relate to WCB activity. Figure 4-7 shows the maximum potential ascent at each coordinate, as in Figure 4-4, but for the nonconvective MAPE described in Section 4.3.3. The large signal of ascent in equatorial regions from Figure 4-4 does not appear in Figure 4-7, suggesting that signal is indeed dominated by convection. A spatial pattern of nonconvective ascent emerges that reaches local maxima in the extratropics. This pattern of maximum potential ascent is compared to the locations of WCB starting points, identified as the first point of the 48-hour ascent in the Madonna et al. [42] climatology. The maximum potential ascent predicted by the climatological atmosphere is comparable to but somewhat smaller than the WCB ascent threshold of 6×10^4 Pa, but larger values of maximum potential ascent are common on shorter timescales, as discussed below. With the climatological frequency of WCB starting point activity overlaid on these contours in Figure 4-7, it is clear that the regions of higher maximum potential ascent in the nonconvective MAPE of the climatological atmosphere cohere significantly with the regions of heightened WCB activity. WCB activity is measured in relative frequency as the percentage of timesteps in which a WCB originates at a given location. Thus, using simply thermodynamic properties of the atmosphere, regions of potential WCB activity can be identified.

4.4.2 Daily Maximum Potential Ascent and WCBs

The general match between the maximum potential ascent in the eddy-size restricted nonconvective MAPE of the climatological atmosphere and climatological WCB activity raises questions about the ability of this approach to predict WCB activity on shorter timescales. To investigate this, the eddy-size restricted nonconvective MAPE and reference pressures are calculated using mean temperature and humidity values on individual days (the average of four six-hourly fields) in a randomly chosen year, 1985, and compared to the total WCB activity over the same time periods. Only one year is examined due to computational expense, but the results for the entire year shown in Figure 4-9 are similar to the results for individual seasons (not shown). Figure 4-8, which shows 4 randomly-chosen example days chosen near the beginning of each season, illustrates that areas of one or more WCB starting points (it is not

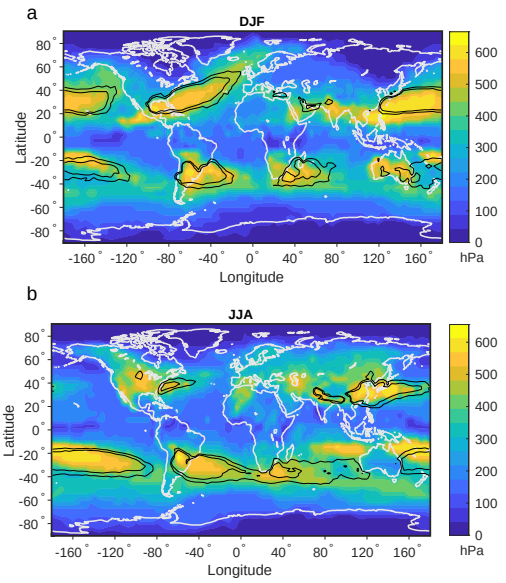

Figure 4-7: Maximum potential ascent in the seasonal eddy-size restricted nonconvective MAPE of the 1979-2018 climatological atmosphere (color contours) and WCB starting point climatological frequency (black contours) for December-January-February (a, DJF) and June-July-August (b, JJA). Nonconvective MAPE is calculated as in Figure 4-5. Maximum potential ascent is calculated at each coordinate as the maximum difference between pressure and reference pressure for any parcel in the column over all the nonconvective MAPE calculations that include that column. Black contours are 1% and 2%, representing the percentage of six-hourly time steps in which an identified WCB begins at that location in the Madonna et al. [42] climatology

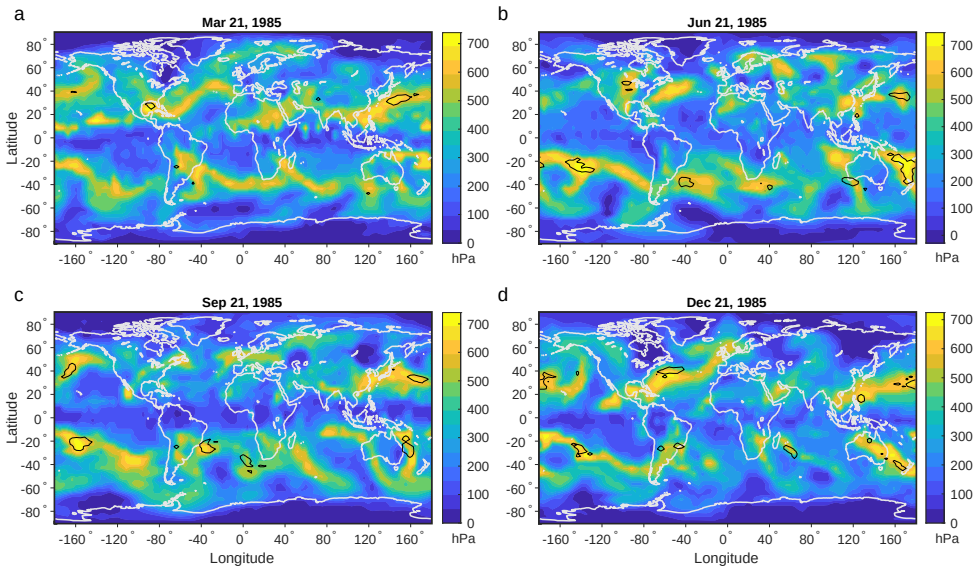

Figure 4-8: Maximum potential ascent in the eddy-size restricted nonconvective MAPE (color contours) and WCB starting points (black contours) for example days in the year 1985. Eddy-size restricted nonconvective MAPE is calculated using the same domains as Figure 4-5. Maximum potential ascent is calculated as in Figure 4-7. Black contours are areas of at least one WCB starting point on a given day in the Madonna et al. [42] climatology.

uncommon for multiple WCBs to start at the same location on a given day) tend to fall in areas of large maximum potential ascent. However, large maximum potential ascent does not directly predict WCB starting points, because WCB activity is also modulated by synoptic meteorology on a given day, and the presence, or lack thereof, of extratropical cyclones.

High values of maximum potential ascent appear to be a necessary but insufficient condition for WCB activity. To illustrate this, the maximum potential ascent in daily eddy-size restricted nonconvective MAPE calculations from 1985 are linearly interpolated to the same grid as the WCB climatology, and all values over every day and every coordinate are collected. The median of the maximum predicted ascent over the global domain is 330 hPa, but the median maximum predicted ascent in regions where at least one WCB starting point occurs is 570 hPa, and the probability density functions of maximum predicted ascent for these two groups are very distinct (Figure 4-9a). Figure 4-9b shows the probability of WCB formation above a given level of

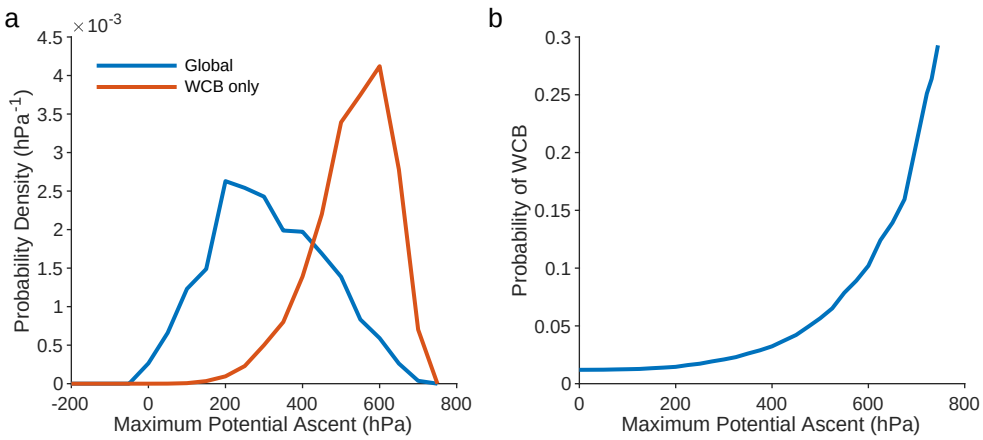

Figure 4-9: Statistical relation of WCB starting points to maximum potential ascent from daily eddy-size restricted nonconvective MAPE calculations in the year 1985. (a) Probability density functions of the maximum potential ascent in all grid cells and days for the entire domain (global) and the domain restricted to incidences of at least one WCB starting point (WCB only), and (b) probability of at least one WCB starting point in all grid cells and days above a given maximum potential ascent. The probability of WCB activity in the whole extratropics (20° to 90°) is 0.02. See text for details.

maximum predicted ascent. In 1985, over 10% of grid cells with maximum potential ascent above 600 hPa have at least one WCB starting point, and over 20% of grid cells with maximum potential ascent above 700 hPa have at least one WCB starting point. Furthermore, the probability of WCB formation increases monotonically and very nonlinearly with maximum predicted ascent. This indicates that maximum potential ascent from daily eddy-size restricted nonconvective MAPE calculations can already predict with some skill the formation of WCBs, and in conjunction with synoptic meteorological fields, may have value in weather forecasting and further understanding of WCBs and the potential effects of climate change. As an indication that such an approach may be successful, in a small domain over which cyclones occur with roughly 30% frequency in a cyclone climatology [92] (160° to 190° in longitude and 40° to 60° N in latitude), roughly 50% of grid cells with maximum potential ascent over 700 hPa have at least one WCB starting point, compared to 8% probability of WCB activity over all maximum potential ascent values in the small domain. Future work could build on this approach with an analytical approximation of WCB potential.

4.5 Discussion and Conclusions

Here, I have calculated the exact three-dimensional moist MAPE of the atmosphere for the first time, and introduced a new methodology to restrict the horizontal distance of parcel rearrangements to the characteristic length scale of extratropical cyclones. In conjunction with preexisting methods to limit the release of convective instability in MAPE calculations, I show that this methodology provides useful insights about the dynamics of extratropical cyclones.

The non-restricted three-dimensional MAPE calculation provides a more accurate accounting of the energy available to extratropical cyclones than previous two-dimensional, zonal mean calculations, by including zonal temperature and moisture gradients and better accounting for topography. The eddy-size restricted calculation identifies regions that are baroclinically unstable, as measured by the Eady growth rate. By examining the difference in pressure and reference pressure of individual calculations, the eddy-size restricted calculation also characterizes thermodynamic potential for ascent. The nonconvective component of the eddy-size restricted MAPE similarly identifies regions corresponding to baroclinic instability, and the maximum potential ascent in those calculations removes the convective ascent in the tropics. The spatial pattern of the convective component of the eddy-size restricted MAPE, i.e. the difference in the full and nonconvective MAPE, also shows similarities to traditional measures of convection, with the key difference that the tropical maximum is removed, suggesting that it may capture the convection associated only with large-scale circulation.

The present work demonstrates that the maximum potential ascent, as determined by the nonconvective eddy-size restricted MAPE of the atmosphere, is related to WCB activity, both in the climatological atmosphere and on individual days. This is a new connection between the mean state of the atmosphere and high-frequency dynamic events. WCBs are crucial components of extratropical cyclones and everyday weather in the midlatitudes. They contribute to cloud formation, precipitation, and play important roles in atmospheric chemistry. The maximum potential ascent

in nonconvective eddy-size restricted MAPE calculations of the climatological atmosphere skillfully identifies regions of heightened WCB activity. Furthermore, as demonstrated across individual days, regions of high maximum potential ascent are more likely to form WCBs than other regions. This approach is useful for understanding the thermodynamic precursors to WCB activity, and may complement or supplement forecasting efforts. Future work should investigate the combination of synoptic meteorology and thermodynamically predicted maximum potential ascent for skillful prediction of WCB activity, as well as the factors determining the maximum potential ascent, in pursuit of an analytical approximation of WCB potential. These techniques should also be applied to simulations of climate change to help determine the potential WCB response.

4.6 Appendix A: Uniform Grid Methodology

To create a uniform grid on a sphere, I follow the methodology introduced in Rosca [64]. The general strategy is to create an equally spaced grid on a square, and then to project it onto each hemisphere by first using a bijection that maps squares onto disks and preserves areas, and then an equal-area projection from the disk to the sphere. The square is of edge e, and the sphere of radius r, where $e = r\sqrt{2\pi}$. Further details and proof of this methodology can be found in Rosca [64].

The grid on the square is created using an identical set of Cartesian coordinates in x and y. For convenience, I define L such that $e = 2L$, and N, the number of divisions. The spacing, d, is then e/N, and the coordinate grids start at $-L + d/2$ and extend with a spacing of d to $L - d/2$. To project this grid onto the Southern Hemisphere and preserve area, I then apply the following formulas to project (a, b), a set of x and y coordinates, into (A, B, C), a set of x, y, and z coordinates.

1. For $0 \leq |b| \leq |a| \leq L$,

$$(A,\, B,\, C) = \left(\frac{2a}{\pi}\sqrt{\pi - \frac{a^2}{r^2}}\cos\frac{b\pi}{4a},\ \frac{2a}{\pi}\sqrt{\pi - \frac{a^2}{r^2}}\sin\frac{b\pi}{4a},\ \frac{2a^2}{\pi r} - r \right); \qquad (4.3)$$

2. For $0 \leq |a| \leq |b| \leq L$,

$$(A,\, B,\, C) = \left(\frac{2b}{\pi} \sqrt{\pi - \frac{b^2}{r^2}} \sin \frac{a\pi}{4b},\ \frac{2b}{\pi} \sqrt{\pi - \frac{b^2}{r^2}} \cos \frac{a\pi}{4b},\ \frac{2b^2}{\pi r} - r \right). \tag{4.4}$$

For the Northern Hemisphere, the formulas are the same as in Equations 4.3 and 4.4, except the formula for C is of opposite sign. These Cartesian coordinates can be easily transformed to Gaussian coordinates on a sphere to give latitude and longitude on a sphere of radius r.

An example of such a grid, which I employ in the analysis and created with 40×40 grids in each hemisphere, can be seen in Figure 4-1.

4.7 Appendix B: Imposing a Nonconvective Condition on Integer Linear Programming Approach to MAPE Calculation

To calculate nonconvective MAPE using the integer linear programming approach, one method is to introduce a new set of linear restrictions that ensures that the reference state position of each parcel i is below or at the same level as the reference state position of each parcel j, where j was originally directly above i in the same column. I accomplish this by introducing an $n \times (n \cdot s)$ matrix, $\tilde{\boldsymbol{A}}$, and an $n \times 1$ vector of zeros, $\tilde{\boldsymbol{b}}$, and impose the restruction that $\tilde{\boldsymbol{A}} \cdot \boldsymbol{x_{vec}} \leq \tilde{\boldsymbol{b}}$. Each row, r_i in matrix $\tilde{\boldsymbol{A}}$ includes pressure assignment values in negative numbers for corresponding parcel i, positive values of the pressure assignments for parcel j, and zero everywhere else, such that the values in the vector $\tilde{\boldsymbol{A}} \cdot \boldsymbol{x_{vec}}$ are the resulting differences in pressure in the reference state between each parcel and the parcel originally immediately above it in the mean state. In many cases, this formulation quickly and efficiently finds the nonconvective reference state. However, in some cases with high convective MAPE, the calculation becomes unstable or takes significantly longer to find the reference state. Thus, I generally employ the divide-and-conquer approach to calculating nonconvective MAPE,

and demonstrate below that, while inexact, it is sufficiently accurate in most cases to be of use. Developing a fast, stable, and exact method to calculate the nonconvective MAPE is a potential avenue for future work.

4.8 Appendix C: Calculation Sensitivities for Eddy-Size Restricted MAPE

4.8.1 Resolution Sensitivity

At very low resolutions, the eddy-size restricted MAPE is not able to capture the characteristic pattern of MAPE (Figure 4-10a) or maximum potential ascent (Figure 4-11a). However, at resolutions beyond roughly 800 grid boxes, or a 20×20 grid in each hemisphere, the results converge, and the characteristic patterns and magnitudes of these two quantities are very similar (see Figure 4-10b, Figure 4-10c, Figure 4-11b, and Figure 4-11c).

4.8.2 Eddy Size Sensitivity

Unlike resolution, as the radius of the subdomains used to calculate eddy-size restricted MAPE increases, the results do not converge. Indeed, one would expect the magnitude of MAPE to increase as the domain increases in size, consistent with previous work on MAPE. However, the characteristic pattern of regions that are most baroclinically unstable does appear to converge after a radius of roughly 10 arc-degrees, although the magnitude continues to increase as the radius increase (Figure 4-12). Interestingly, the pattern of maximum potential ascent seems to converge at a larger radius, with noticeable differences between the 10 arc-degrees and 15 arc-degree calculations, but similar patterns of maximum potential ascent for the 15 arc-degree and 20 arc-degree calculations (Figure 4-13).

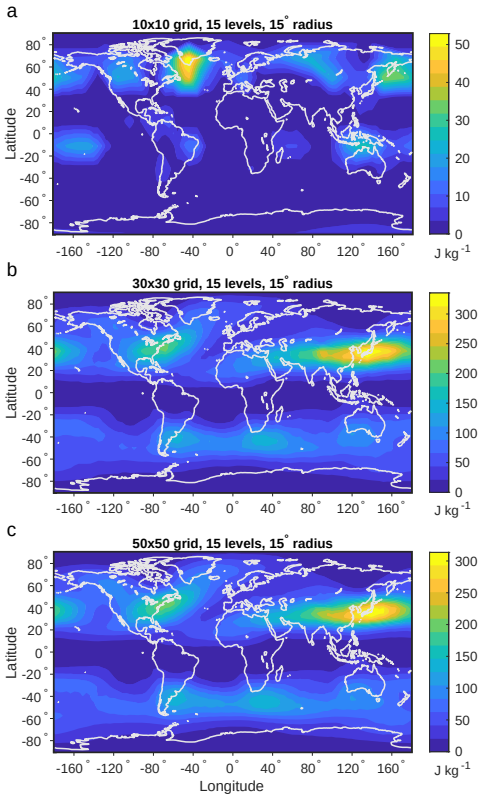

Figure 4-10: Eddy-size restricted MAPE of the 1979-2018 DJF climatological atmosphere for grids of varying surface resolution, 15 pressure levels, and subdomains of radius 15 arc-degrees (1670 kilometers). (a) 200 surface coordinates, or 10×10 grid in each hemisphere, (b) 1800 surface coordinates, or 30×30 grid in each hemisphere, and (c) 5000 surface coordinates, or 50×50 grid in each hemisphere.

4.8.3 Calculation Method Sensitivity

In most of the atmosphere, and in particular in nearly all of the extratropics, the divide-and-conquer algorithm and the integer linear programming approach to calculating full eddy-size restricted MAPE give nearly identical values for MAPE and maximum potential ascent (see Figure 4-14 and Figure 4-15). However, in some regions in the tropics and subtropics with low overall MAPE, the divide-and-conquer algorithm can be very inaccurate, as a fraction of the exact MAPE given by the integer linear programming. Indeed, in some extreme cases, it returns a negative value for MAPE (black contours in Figure 4-14), which is physically impossible but

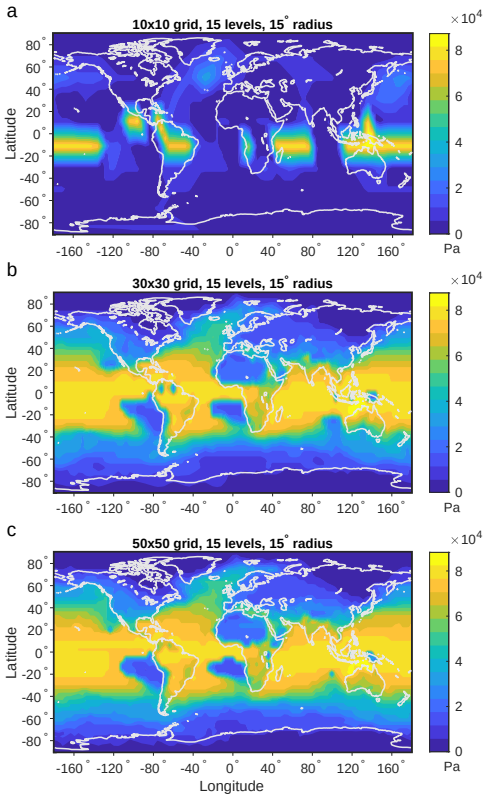

Figure 4-11: Maximum potential ascent in eddy-size restricted MAPE of the 1979-2018 DJF climatological atmosphere for grids of varying surface resolution, 15 pressure levels, and subdomains of radius 15 arc-degrees (1670 kilometers). (a) 200 surface grid boxes, or 10×10 grid in each hemisphere, (b) 1800 surface grid boxes, or 30×30 grid in each hemisphere, and (c) 5000 surface grid boxes, or 50×50 grid in each hemisphere.

known to occur in certain cases with the divide-and-conquer algorithm [25]. Figure 4-14 demonstrates this phenomenon for an example season, DJF, and differences are similar across all seasons. Similarly, in some areas in the tropics, the exact MAPE predicts large maximum potential ascent that is not captured by the divide-and-conquer algorithm (4-15). These inaccuracies do not affect the conclusions of this chapter.

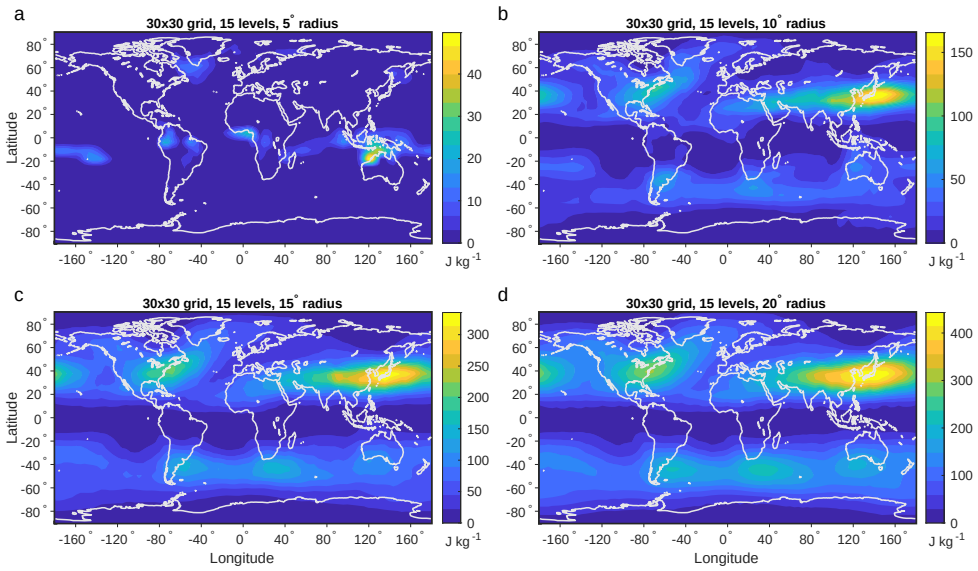

Figure 4-12: Eddy-size restricted MAPE of the 1979-2018 DJF climatological atmosphere using subdomains of varying radii, 1800 surface coordinates (a 30×30 grid in each hemisphere), and 15 pressure levels. (a) 5 arc-degree (560 km) subdomain radii, (b) 10 arc-degree (1110 kilometers) subdomain radii, (c) 15 arc-degree (1670 kilometers) subdomain radii, and (d) 20 arc-degree (2230 kilometers) subdomain radii.

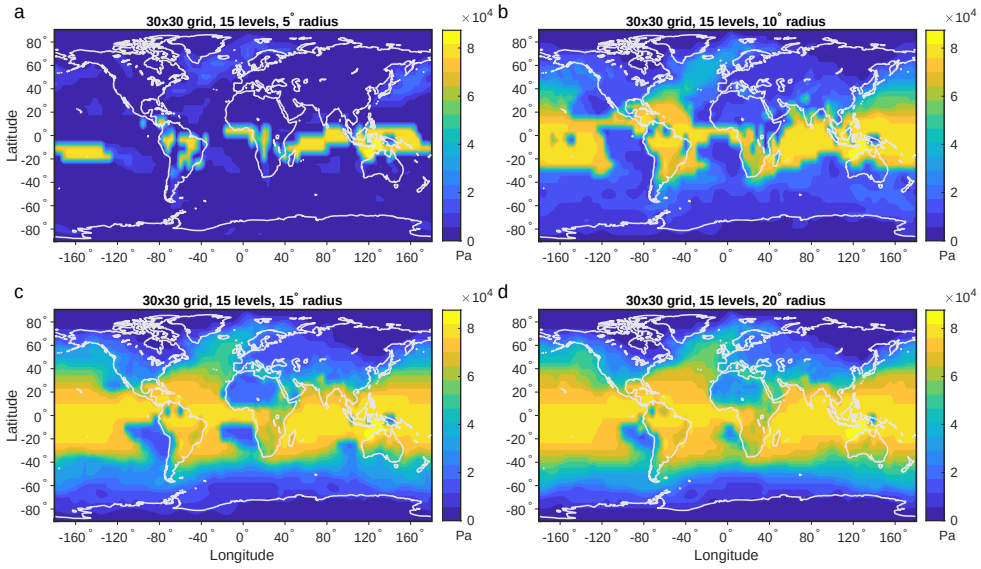

Figure 4-13: Maximum potential ascent in eddy-size restricted MAPE of the 1979-2018 DJF climatological atmosphere using subdomains of varying radii, 1800 surface coordinates (a 30×30 grid in each hemisphere), and 15 pressure levels. (a) 5 arc-degree (560 km) subdomain radii, (b) 10 arc-degree (1110 kilometers) subdomain radii, (c) 15 arc-degree (1670 kilometers) subdomain radii, and (d) 20 arc-degree (2230 kilometers) subdomain radii.

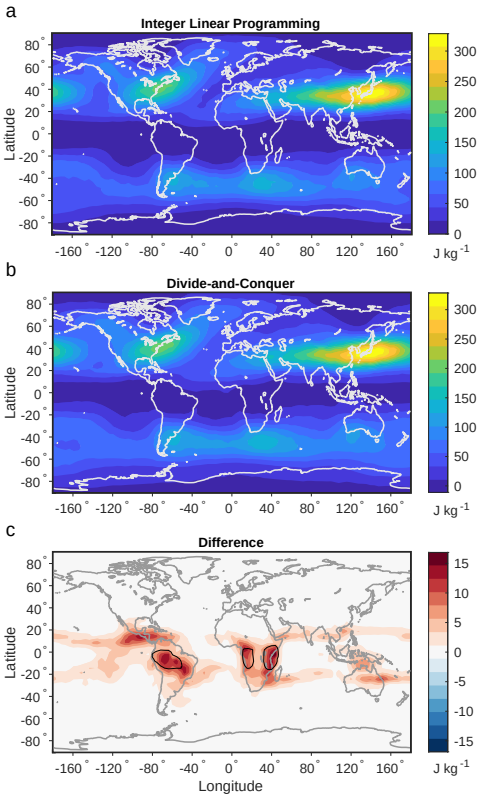

Figure 4-14: Calculation method sensitivity for the eddy-size restricted MAPE of the 1979-2018 climatological atmosphere for December-January-February (DJF). Shown is MAPE calculated using the exact integer linear programming approach (a), MAPE calculated using the approximate divide-and-conquer approach (b), and the difference, reported as the value calculated with integer linear programming minus the value calculated with divide-and-conquer algorithm at each cell (c). MAPE is calculated as in Figure 4-3. Black contours in (c) indicate regions where the MAPE values calculated with divide-and-conquer algorithm are below zero.

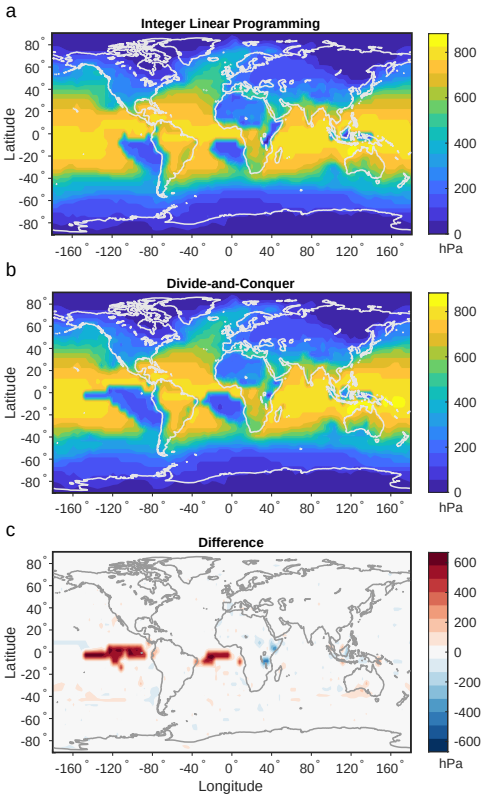

Figure 4-15: Calculation method sensitivity for the maximum potential ascent in eddy-size restricted MAPE calculations of the 1979-2018 climatological atmosphere for December-January-February (DJF). Shown is maximum potential ascent calculated using the exact integer linear programming approach (a), maximum potential ascent calculated using the approximate divide-and-conquer approach (b), and the difference, reported as the value calculated with integer linear programming minus the value calculated with divide-and-conquer algorithm at each cell (c). MAPE is calculated as in Figure 4-3

Chapter 5

Closing Remarks

5.1 Summary of Key Results

The results from the three main research chapters of this thesis demonstrate that certain high frequency weather phenomena in the Earth's extratropical regions can be linked to the mean state of atmosphere. In each chapter, I made progress in understanding some high frequency phenomenon, or change therein, through the thermodynamic characteristics and MAPE of the atmosphere.

In Chapter 2, I began with the observation that in Northern Hemisphere summer, the extratropical circulation weakened while extratropical convection strengthened during the satellite era [15, 12, 93]. Previous work showed the sign of changes in meridional temperature gradients to be consistent with the weakening storm tracks [12], but the magnitude of changes were not consistent, and these analyses did not account for changes in the static stability or moisture. The main result of this chapter is to quantitatively connect these observed changes in weather to changes in the temperature and humidity of the atmosphere consistent with the highest quality observations. Furthermore, by constructing idealized atmospheres for the Northern Hemisphere summer, and demonstrating that convective MAPE is relatively more sensitive than nonconvective MAPE to changes in mean surface temperature in the extratropical region, I make a physical argument for how convective precipitation and storm track strength can diverge in intensity.

In Chapter 3, I began with the observation that even in complex solar geoengineering simulations that aim to minimize changes in the meridional temperature gradient, the storm track still weakens in both hemispheres compared to a baseline climate [76]. It was originally thought that the changes in temperature in these simulations were too small to induce such large changes in storm track intensity, and that changes in moisture from geoengineering or changes in radiative cooling in extratropical cyclones due to increased CO_2 concentrations may have been causing the decrease [76]. This chapter demonstrates conclusively using MAPE that, while the magnitudes of temperature changes are small, the consistent temperature gradient changes at different vertical levels work in concert to influence the storm tracks with similar magnitudes as in the global warming case, at least in the Northern Hemisphere. I also demonstrate that proposed partial geoengineering may have little effect on the storm track in the Northern Hemisphere in the presence of increasing greenhouse gas concentrations. These results imply that extratropical weather, and its impact on the rest of the climate system, would be significantly different in a geoengineered climate.

Finally, in Chapter 4, I began with the observation that MAPE as it is traditionally calculated in the zonal mean atmosphere, does not capture the zonally-varying pattern of mass redistribution or available potential energy. By performing the first exact three-dimensional calculations of MAPE, I demonstrate the relative contributions of the zonally-varying and zonal-mean components of temperature and humidity to the overall MAPE, and identify major areas of ascent in the calculation. Furthermore, by introducing an eddy-size restriction, I produce an estimate of local MAPE on the eddy length scale, as well as identify the potential for ascent on the eddy length scale that is larger in higher latitudes than in the global calculation because the tropical convective signal does not dominate the optimization. I show that this potential ascent on the eddy length scale relates to WCB activity, with implications for extreme precipitation and winds. As a thermodynamic identifier for specific synoptic phenomena, I believe the tool will be useful in studying how potential future climate changes may affect weather in the extratropics.

5.2 Future Research

Large questions remain to be answered in the connection between the mean climate and extratropical circulation, in parts inspired by, and in parts tangential to the results of this thesis. This future work could be separated into two major categories: further theoretical advances and further applications of the tools developed here.

The results of Chapters 2 and 4 inspire a more thorough empirical approach to connecting convective MAPE to specific sub-daily timescale convective phenomena in the atmosphere, in the same style that EKE is shown to relate to nonconvective MAPE. Idealized climate modeling could be employed to study the empirical relation between convection and convective MAPE, and its spatial distribution, over forced climate changes. Chapter 2 also leaves open the question of how MAPE and EKE are related over shorter timescales in the Northern Hemisphere, or whether they are related at all under unforced variability. A baroclinic annular mode has been identified in the Southern Hemisphere in which EKE and baroclinic instability enter into a coupled oscillation on a 20-30 day timescale [83], and similar modes have been identified in the Northern Hemisphere [2], which may help define the relation between MAPE and EKE over different timescales and unforced variability.

The results of Chapter 3 inspire further theoretical investigation in the field of geoengineering. The interesting and nonintuitive results from Chapter 3 suggest that there may be some fundamental limit to the ability of solar geoengineering to minimize changes to the meridional temperature gradients and storm track strength [41]; simple energy balance models and idealized modeling experiments again could be employed to test these limits, or an idealized solar geoengineering scheme with minimal possible effects on the storm track could be developed.

The results of Chapter 4 suggests that it may be interesting to explore the calculation of MAPE with further dynamical constraints; for instance, a MAPE calculation that conserves potential vorticity may provide even more insights into the potential for specific meteorological phenomena like WCBs. A simplified theory for WCB potential may be possible using the MAPE framework presented in Chapter 4, similar

to the maximum potential intensity for tropical cyclones formalized in Emanuel [21].

Finally, it would also be of interest to apply the techniques developed in Chapter 4 to the time periods and experiments studied in Chapters 2 and 3, in particular to the Atlantic and Pacific storm tracks separately: Does the three-dimensional MAPE cohere with EKE over the same temporal scales? How does the zonally-asymmetric component vary in time and with climate changes? Also, spatial variability in baroclinic regions and regions of potential WCB formation could be compared to variability in cyclone and WCB activity. The changes in three-dimensional MAPE and the patterns of maximum potential ascent in high resolution global warming simulations would be interesting to investigate as well. Finally, the eddy-size constraint paradigm has the useful characteristic that rearrangements at different spatial scales can be investigated. At a size-limit of zero, the individual calculations simply represent the total potential energy available for convection, sometimes referred to as generalized CAPE (GCAPE); further investigation of the GCAPE of the climatological atmosphere may help provide insight into some of the outstanding questions about atmospheric convection, such as the mismatch between CAPE and observed lightning in the land-ocean contrast [63].

The advances presented in this thesis are meant to be complementary to other modes of investigation into the effects of changes in climate on extratropical circulation. Modeling of varying complexity, dynamic theory, and observations are all crucial to producing this important knowledge, and I enter these results in the hope that they may increase our understanding of the connections between climate and weather, and inspire future work that continues to do so. We study climate in the service of life on Earth, that we may make better decisions in our stewardship of this planet.

Bibliography

[1] V. Agard and K. Emanuel. Clausius-clapeyron scaling of peak CAPE in continental convective storm environments. *Journal of the Atmospheric Sciences*, 74(9):3043–3054, 2017.

[2] M. H. P. Ambaum and L. Novak. A nonlinear oscillator describing storm track variability. *Quarterly Journal of the Royal Meteorological Society*, 140(685):2680–2684, 2014.

[3] C. M. Ammann, W. M. Washington, G. A. Meehl, L. Buja, and H. Y. Teng. Climate engineering through artificial enhancement of natural forcings: Magnitudes and implied consequences. *Journal of Geophysical Research: Atmospheres*, 115:D22109, 2010.

[4] V. K. Arora, J. F. Scinocca, G. J. Boer, J. R. Christian, K. L. Denman, G. M. Flato, V. V. Kharin, W. G. Lee, and W. J. Merryfield. Carbon emission limits required to satisfy future representative concentration pathways of greenhouse gases. *Geophysical Research Letters*, 38:L05805, 2011.

[5] G. Bala, P. B. Duffy, and K. E. Taylor. Impact of geoengineering schemes on the global hydrological cycle. *Proceedings of the National Academy of Sciences of the United States of America*, 105(22):7664–7669, 2008.

[6] A. K. Betts and Harshvardhan. Thermodynamic constraint on the cloud liquid water feedback in climate models. *Journal of Geophysical Research-Atmospheres*, 92(D7):8483–8485, 1987.

[7] K. A. Browning. Organization of clouds and precipitation in extratropical cyclones. *Extratropical Cyclones: the Erik Palmen Memorial Volume*, pages 129–153, 1990.

[8] Amy H. Butler, David W. J. Thompson, and Ross Heikes. The steady-state atmospheric circulation response to climate change-like thermal forcings in a simple general circulation model. *Journal of Climate*, 23(13):3474–3496, 2010.

[9] J. L. Catto and S. Pfahl. The importance of fronts for extreme precipitation. *Journal of Geophysical Research-Atmospheres*, 118(19):10791–10801, 2013.

[10] J. L. Catto, L. C. Shaffrey, and K. I. Hodges. Can climate models capture the structure of extratropical cyclones? *Journal of Climate*, 23(7):1621–1635, 2010.

[11] E. K. M. Chang, S. Y. Lee, and K. L. Swanson. Storm track dynamics. *Journal of Climate*, 15(16):2163–2183, 2002.

[12] E. K. M. Chang, C. G. Ma, C. Zheng, and A. M. W. Yau. Observed and projected decrease in northern hemisphere extratropical cyclone activity in summer and its impacts on maximum temperature. *Geophysical Research Letters*, 43(5):2200–2208, 2016.

[13] P. Chylek, C. K. Folland, G. Lesins, M. K. Dubey, and M.Y. Wang. Arctic air temperature change amplification and the atlantic multidecadal oscillation. *Geophysical Research Letters*, 36, 2009.

[14] W. J. Collins, N. Bellouin, M. Doutriaux-Boucher, N. Gedney, P. Halloran, T. Hinton, J. Hughes, C. D. Jones, M. Joshi, S. Liddicoat, G. Martin, F. O'Connor, J. Rae, C. Senior, S. Sitch, I. Totterdell, A. Wiltshire, and S. Woodward. Development and evaluation of an earth-system model-HadGEM2. *Geoscientific Model Development*, 4(4):1051–1075, 2011.

[15] D. Coumou, J. Lehmann, and J. Beckmann. The weakening summer circulation in the northern hemisphere mid-latitudes. *Science*, 348(6232):324–327, 2015.

[16] A.G. Dai, J.H. Wang, P. W. Thorne, D. E. Parker, L. Haimberger, and X. L. Wang. A new approach to homogenize daily radiosonde humidity data. *Journal of Climate*, 24(4):965–991, 2011.

[17] D. P. Dee, S. M. Uppala, A. J. Simmons, P. Berrisford, P. Poli, S. Kobayashi, U. Andrae, M. A. Balmaseda, G. Balsamo, P. Bauer, P. Bechtold, A. C. M. Beljaars, L. van de Berg, J. Bidlot, N. Bormann, C. Delsol, R. Dragani, M. Fuentes, A. J. Geer, L. Haimberger, S. B. Healy, H. Hersbach, E. V. Holm, L. Isaksen, P. Kallberg, M. Koehler, M. Matricardi, A. P. McNally, B. M. Monge-Sanz, J. J. Morcrette, B. K. Park, C. Peubey, P. de Rosnay, C. Tavolato, J. N. Thepaut, and F. Vitart. The ERA-interim reanalysis: configuration and performance of the data assimilation system. *Quarterly Journal of the Royal Meteorological Society*, 137(656):553–597, 2011.

[18] Q. Ding, J. M. Wallace, D. S. Battisti, E. J. Steig, A. J. E. Gallant, H. J. Kim, and L. Geng. Tropical forcing of the recent rapid Arctic warming in northeastern canada and greenland. *Nature*, 509(7499):209–212, 2014.

[19] J. L. Dufresne, M. A. Foujols, S. Denvil, A. Caubel, O. Marti, O. Aumont, Y. Balkanski, S. Bekki, H. Bellenger, R. Benshila, S. Bony, L. Bopp, P. Braconnot, P. Brockmann, P. Cadule, F. Cheruy, F. Codron, A. Cozic, D. Cugnet, N. de Noblet, J. P. Duvel, C. Ethe, L. Fairhead, T. Fichefet, S. Flavoni, P. Friedlingstein, J. Y. Grandpeix, L. Guez, E. Guilyardi, D. Hauglustaine, F. Hourdin, A. Idelkadi, J. Ghattas, S. Joussaume, M. Kageyama, G. Krinner, S. Labetoulle, A. Lahellec, M. P. Lefebvre, F. Lefevre, C. Levy, Z. X. Li,

J. Lloyd, F. Lott, G. Madec, M. Mancip, M. Marchand, S. Masson, Y. Meurdesoif, J. Mignot, I. Musat, S. Parouty, J. Polcher, C. Rio, M. Schulz, D. Swingedouw, S. Szopa, C. Talandier, P. Terray, N. Viovy, and N. Vuichard. Climate change projections using the IPSL-CM5 earth system model: from CMIP3 to CMIP5. *Climate Dynamics*, 40(9-10):2123–2165, 2013.

[20] K. A. Emanuel. *Atmospheric convection*. Oxford University Press, New York, 1994.

[21] K. A. Emanuel. Sensitivity of tropical cyclones to surface exchange coefficients and a revised steady-state model incorporating eye dynamics. *Journal of the Atmospheric Sciences*, 52(22):3969–3976, 1995.

[22] C. G. Gertler and P. A. O'Gorman. Changing available energy for extratropical cyclones and associated convection in northern hemisphere summer. *Proceedings of the National Academy of Sciences*, 116(10):4105–4110, 2019.

[23] C. G. Gertler, P. A. O'Gorman, B. Kravitz, J.C. Moore, S. J. Phipps, and S. Watanabe. Weakening of the extratropical storm tracks in idealized solar geoengineering scenarios. *Geophysical Research Letters*, 47(e2020GL087348), 2020.

[24] L. Haimberger, C. Tavolato, and S. Sperka. Toward elimination of the warm bias in historic radiosonde temperature records - some new results from a comprehensive intercomparison of upper-air data. *Journal of Climate*, 21(18):4587–4606, 2008.

[25] B. L. Harris and R. Tailleux. Assessment of algorithms for computing moist available potential energy. *Quarterly Journal of the Royal Meteorological Society*, 144(714):1501–1510, 2018.

[26] B. J. Harvey, L. C. Shaffrey, and T. J. Woollings. Equator-to-pole temperature differences and the extra-tropical storm track responses of the CMIP5 climate models. *Climate Dynamics*, 43(5-6):1171–1182, 2014.

[27] M. Hieronymus and J. Nycander. Finding the minimum potential energy state by adiabatic parcel rearrangements with a nonlinear equation of state: An exact solution in polynomial time. *Journal of Physical Oceanography*, 45(7):1843–1857, 2015.

[28] B. J. Hoskins and P. J. Valdes. On the existence of storm-tracks. *Journal of the Atmospheric Sciences*, 47(15):1854–1864, 1990.

[29] P. J. Irvine, K. Emanuel, J. He, L. W. Horowitz, G. Vecchi, and D. Keith. Halving warming with idealized solar geoengineering moderates key climate hazards. *Nature Climate Change*, 9(4):295–299, 2019.

[30] P. J. Irvine, B. Kravitz, M. G. Lawrence, and H. Muri. An overview of the earth system science of solar geoengineering. *Wiley Interdisciplinary Reviews: Climate Change*, 7(6):815–833, 2016.

[31] D. Ji, L. Wang, J. Feng, Q. Wu, H. Cheng, Q. Zhang, J. Yang, W. Dong, Y. Dai, D. Gong, R. H. Zhang, X. Wang, J. Liu, J. C. Moore, D. Chen, and M. Zhou. Description and basic evaluation of beijing normal university earth system model (BNU-ESM) version 1. *Geoscientific Model Development*, 7(5):2039–2064, 2014.

[32] W. M. Kim and Y. S. Choi. Long-term change of the atmospheric energy cycles and weather disturbances. *Climate Dynamics*, 49(9-10):3605–3617, 2017.

[33] R. L. Korty and T. Schneider. A climatology of the tropospheric thermal stratification using saturation potential vorticity. *Journal of Climate*, 20(24):5977–5991, 2007.

[34] B. Kravitz, K. Caldeira, O. Boucher, A. Robock, P. J. Rasch, K. Alterskjaer, D. B. Karam, J. N. S. Cole, C. L. Curry, J. M. Haywood, P. J. Irvine, D. Y. Ji, A. Jones, J. E. Kristjansson, D. J. Lunt, J. C. Moore, U. Niemeier, H. Schmidt, M. Schulz, B. Singh, S. Tilmes, S. Watanabe, S. T. Yang, and J. H. Yoon. Climate model response from the geoengineering model intercomparison project (GeoMIP). *Journal of Geophysical Research: Atmospheres*, 118(15):8320–8332, 2013.

[35] B. Kravitz, D. G. MacMartin, M. J. Mills, J. H. Richter, S. Tilmes, J. F. Lamarque, J. J. Tribbia, and F. Vitt. First simulations of designing stratospheric sulfate aerosol geoengineering to meet multiple simultaneous climate objectives. *Journal of Geophysical Research: Atmospheres*, 122(23):12616–12634, 2017.

[36] B. Kravitz, A. Robock, O. Boucher, H. Schmidt, K. E. Taylor, G. Stenchikov, and M. Schulz. The geoengineering model intercomparison project (GeoMIP). *Atmospheric Science Letters*, 12(2):162–167, 2011.

[37] E. M. Leibensperger, L. J. Mickley, and D. J. Jacob. Sensitivity of US air quality to mid-latitude cyclone frequency and implications of 1980-2006 climate change. *Atmospheric Chemistry and Physics*, 8(23):7075–7086, 2008.

[38] E. N. Lorenz. Available potential energy and the maintenance of the general circulation. *Tellus*, 7(2):157–167, 1955.

[39] E. N. Lorenz. Available energy and maintenance of a moist circulation. *Tellus*, 30(1):15–31, 1978.

[40] E. N. Lorenz. Numerical evaluation of moist available energy. *Tellus*, 31(3):230–235, 1979.

[41] N. J. Lutsko, J. T. Seeley, and D. W. Keith. Estimating impacts and trade-offs in solar geoengineering scenarios with a moist energy balance model. *Geophysical Research Letters*, 47(9), 2020.

[42] E. Madonna, H. Wernli, H. Joos, and O. Martius. Warm conveyor belts in the ERA-interim dataset (1979-2010). Part I: climatology and potential vorticity evolution. *J Clim*, 27(1):3–26, 2014.

[43] M. P. McCarthy, P. W. Thorne, and H. A. Titchner. An analysis of tropospheric humidity trends from radiosondes. *Journal of Climate*, 22(22):5820–5838, 2009.

[44] K. E. McCusker, D. S. Battisti, and C. M. Bitz. Inability of stratospheric sulfate aerosol injections to preserve the West Antarctic Ice Sheet. *Geophysical Research Letters*, 42(12):4989–4997, 2015.

[45] J. C. Moore, A. Rinke, X. Y. Yu, D. Y. Ji, X. F. Cui, Y. Li, K. Alterskjaer, J. E. Kristjansson, H. Muri, O. Boucher, N. Huneeus, B. Kravitz, A. Robock, U. Niemeier, M. Schulz, S. Tilmes, S. Watanabe, and S. T. Yang. Arctic sea ice and atmospheric circulation under the GeoMIP G1 scenario. *Journal of Geophysical Research: Atmospheres*, 119(2):567–583, 2014.

[46] A. Oertel, M. Boettcher, H. Joos, M. Sprenger, H. Konow, M. Hagen, and H. Wernli. Convective activity in an extratropical cyclone and its warm conveyor belt - a case-study combining observations and a convection-permitting model simulation. *Quarterly Journal of the Royal Meteorological Society*, 145(721):1406–1426, 2019.

[47] A. Oertel, M. Boettcher, H. Joos, M. Sprenger, and H. Wernli. Potential vorticity structure of embedded convection in a warm conveyor belt and its relevance for large-scale dynamics. *Weather and Climate Dynamics*, 1(1):127–153, 2020.

[48] P. A. O'Gorman. Understanding the varied response of the extratropical storm tracks to climate change. *Proceedings of the National Academy of Sciences*, 107(45):19176–19180, 2010.

[49] P. A. O'Gorman. The effective static stability experienced by eddies in a moist atmosphere. *Journal of the Atmospheric Sciences*, 68(1):75–90, 2011.

[50] P. A. O'Gorman and T. Schneider. Energy of midlatitude transient eddies in idealized simulations of changed climates. *Journal of Climate*, 21(22):5797–5806, 2008.

[51] A. H. Oort, S. C. Ascher, S. Levitus, and J. P. Peixoto. New estimates of the available potential energy in the world ocean. *Journal of Geophysical Research-Oceans*, 94(C3):3187–3200, 1989.

[52] Y. F. Pan, L. M. Li, X. Jiang, G. Li, W. T. Zhang, X. Y. Wang, and A. P. Ingersoll. Earth's changing global atmospheric energy cycle in response to climate change. *Nature Communications*, 8, 2017.

[53] O. Pauluis. Sources and sinks of available potential energy in a moist atmosphere. *Journal of the Atmospheric Sciences*, 64(7):2627–2641, 2007.

[54] J. P. Peixoto and A. H. Oort. *Physics of climate*. American Institute of Physics, New York, 1992.

[55] S. Pfahl, E. Madonna, M. Boettcher, H. Joos, and H. Wernli. Warm conveyor belts in the ERA-interim dataset (1979-2010). Part II: Moisture origin and relevance for precipitation. *Journal of Climate*, 27(1):27–40, 2014.

[56] S. Pfahl and H. Wernli. Quantifying the relevance of atmospheric blocking for co-located temperature extremes in the northern hemisphere on (sub-)daily time scales. *Geophysical Research Letters*, 39, 2012.

[57] S. J. Phipps, L. D. Rotstayn, H. B. Gordon, J. L. Roberts, A. C. Hirst, and W. F. Budd. The CSIRO Mk3L climate system model version 1.0-part 1: Description and evaluation. *Geoscientific Model Development*, 4(2):483–509, 2011.

[58] D. A. Randall and J. Wang. The moist available energy of a conditionally unstable atmosphereâĂă. *J Atmos Sci*, 49(3):240–255, 1992.

[59] S. Rasp, T. Selz, and G. C. Craig. Convective and slantwise trajectory ascent in convection-permitting simulations of midlatitude cyclones. *Mon Weather Rev*, 144(10):3961–3976, 2016.

[60] J. H. Richter, S. Tilmes, A. Glanville, B. Kravitz, D. G. MacMartin, M. J. Mills, I. R. Simpson, F. Vitt, J. J. Tribbia, and J. F. Lamarque. Stratospheric response in the first geoengineering simulation meeting multiple surface climate objectives. *Journal of Geophysical Research: Atmospheres*, 123(11):5762–5782, 2018.

[61] K. Riemann-Campe, K. Fraedrich, and F. Lunkeit. Global climatology of convective available potential energy (CAPE) and convective inhibition (CIN) in era-40 reanalysis. *Atmospheric Research*, 93(1-3):534–545, 2009.

[62] A. Robock, A. Marquardt, B. Kravitz, and G. Stenchikov. Benefits, risks, and costs of stratospheric geoengineering. *Geophysical Research Letters*, 36(19):L19703, 2009.

[63] D. M. Romps, A. B. Charn, R. H. Holzworth, W. E. Lawrence, J. Molinari, and D. Vollaro. CAPE times P explains lightning over land but not the land-ocean contrast. *Geophysical Research Letters*, 45(22):12623–12630, 2018.

[64] D. Rosca. New uniform grids on the sphere. *Astronomy & Astrophysics*, 520:4, 2010.

[65] R. D. Russotto and T. P. Ackerman. Changes in clouds and thermodynamics under solar geoengineering and implications for required solar reduction. *Atmospheric Chemistry and Physics*, 18(16):11905–11925, 2018.

[66] R. D. Russotto and T. P. Ackerman. Energy transport, polar amplification, and ITCZ shifts in the GeoMIP G1 ensemble. *Atmospheric Chemistry and Physics*, 18(3):2287–2305, 2018.

[67] E. K. Schneider. On the amplitudes reached by baroclinically unstable disturbances. *Journal of the Atmospheric Sciences*, 38(10):2142–2149, 1981.

[68] T. Schneider and C. C. Walker. Scaling laws and regime transitions of macroturbulence in dry atmospheres. *Journal of the Atmospheric Sciences*, 65(7):2153–2173, 2008.

[69] J. A. Screen and I. Simmonds. The central role of diminishing sea ice in recent Arctic temperature amplification. *Nature*, 464(7293):1334–1337, 2010.

[70] J. T. Seeley and D. M. Romps. Why does tropical convective available potential energy (CAPE) increase with warming? *Geophysical Research Letters*, 42(23):10429–10437, 2015.

[71] T. A. Shaw, M. Baldwin, E. A. Barnes, R. Caballero, C. I. Garfinkel, Y. T. Hwang, C. Li, P. A. O'Gorman, G. Riviere, I. R. Simpson, and A. Voigt. Storm track processes and the opposing influences of climate change. *Nature Geoscience*, 9(9):656–664, 2016.

[72] T. A. Shaw and A. Voigt. Tug of war on summertime circulation between radiative forcing and sea surface warming. *Nature Geoscience*, 8(7):560–U105, 2015.

[73] S. C. Sherwood, W. Ingram, Y. Tsushima, M. Satoh, M. Roberts, P. L. Vidale, and P. A. O'Gorman. Relative humidity changes in a warmer climate. *Journal of Geophysical Research-Atmospheres*, 115, 2010.

[74] S. C. Sherwood and N. Nishant. Atmospheric changes through 2012 as shown by iteratively homogenized radiosonde temperature and wind data (IUKv2). *Environmental Research Letters*, 10(5), 2015.

[75] A. J. Simmons, A. Untch, C. Jakob, P. KÃěllberg, and P. UndÃĺn. Stratospheric water vapour and tropical tropopause temperatures in ECMWF analyses and multi-year simulations. *Q J R Meteorol Soc*, 125(553):353–386, 1999.

[76] I. R. Simpson, S. Tilmes, J. H. Richter, B. Kravitz, D. G. MacMartin, M. J. Mills, J. T. Fasullo, and A. G. Pendergrass. The regional hydroclimate response to stratospheric sulfate geoengineering and the role of stratospheric heating. *Journal of Geophysical Research: Atmospheres*, 124:Advance online publication, 2019.

[77] M. S. Singh, Z. M. Kuang, E. D. Maloney, W. M. Hannah, and B. O. Wolding. Increasing potential for intense tropical and subtropical thunderstorms under global warming. *Proceedings of the National Academy of Sciences of the United States of America*, 114(44):11657–11662, 2017.

[78] M. S. Singh and P. A. O'Gorman. Influence of entrainment on the thermal stratification in simulations of radiative-convective equilibrium. *Geophysical Research Letters*, 40(16):4398–4403, 2013.

[79] E. M. Stansifer, P. A. O'Gorman, and J. I. Holt. Accurate computation of moist available potential energy with the Munkres algorithm. *Quarterly Journal of the Royal Meteorological Society*, 143(702):288–292, 2017.

[80] Z. Su and A. P. Ingersoll. On the minimum potential energy state and the eddy size-constrained APE density. *Journal of Physical Oceanography*, 46(9):2663–2674, 2016.

[81] R. Tailleux. Available potential energy density for a multicomponent Boussinesq fluid with arbitrary nonlinear equation of state. *Journal of Fluid Mechanics*, 735:499–518, 2013.

[82] K. E. Taylor, R. J. Stouffer, and G. A. Meehl. An overview of CMIP5 and the experimental design. *Bulletin of the American Meteorological Society*, 93(4):485–498, 2012.

[83] D. W. J. Thompson and E. A. Barnes. Periodic variability in the large-scale southern hemisphere atmospheric circulation. *Science*, 343(6171):641–645, 2014.

[84] P. D. Thompson. Large-scale dynamic-response to differential heating - statistical equilibrium states and amplitude vacillation. *Journal of the Atmospheric Sciences*, 44(8):1237–1248, 1987.

[85] S. Tilmes, J. H. Richter, B. Kravitz, D. G. MacMartin, M. J. Mills, I. R. Simpson, A. S. Glanville, J. T. Fasullo, A. S. Phillips, J. F. Lamarque, J. Tribbia, J. Edwards, S. Mickelson, and S. Ghosh. CESMI(WACCM) stratospheric aerosol geoengineering large ensemble project. *Bulletin of the American Meteorological Society*, 99(11):2361–2371, 2018.

[86] K. E. Trenberth and A. Dai. Effects of Mount Pinatubo volcanic eruption on the hydrological cycle as an analog of geoengineering. *Geophysical Research Letters*, 34(15), 2007.

[87] K. E. Trenberth and D. P. Stepaniak. Covariability of components of poleward atmospheric energy transports on seasonal and interannual timescales. *Journal of Climate*, 16(22):3691–3705, 2003.

[88] G. K. Vallis. Atmospheric and oceanic fluid dynamics: Fundamentals and large-scale circulation, 2nd edition. *Atmospheric and Oceanic Fluid Dynamics: Fundamentals and Large-Scale Circulation, 2nd Edition*, pages 1–946, 2017.

[89] J. Wang and D. A. Randall. The moist available energy of a conditionally unstable atmosphere. part ii. further analysis of GATE data. *J Atmos Sci*, 51(5):703–710, 1994.

[90] J. H. Wang, L. Y. Zhang, A. G. Dai, F. Immler, M. Sommer, and H. Voemel. Radiation dry bias correction of vaisala RS92 humidity data and its impacts on historical radiosonde data. *Journal of Atmospheric and Oceanic Technology*, 30(2):197–214, 2013.

[91] S. Watanabe, T. Hajima, K. Sudo, T. Nagashima, T. Takemura, H. Okajima, T. Nozawa, H. Kawase, M. Abe, T. Yokohata, T. Ise, H. Sato, E. Kato,

K. Takata, S. Emori, and M. Kawamiya. MIROC-ESM 2010: model description and basic results of CMIP5-20c3m experiments. *Geoscientific Model Development*, 4(4):845–872, 2011.

[92] H. Wernli and C. Schwierz. Surface cyclones in the ERA-40 dataset (1958-2001). Part I: Novel identification method and global climatology. *Journal of the Atmospheric Sciences*, 63(10):2486–2507, 2006.

[93] H. Ye, E. J. Fetzer, S. Wong, and B. H. Lambrigtsen. Rapid decadal convective precipitation increase over eurasia during the last three decades of the 20th century. *Science Advances*, 3(1), 2017.

[94] J. Yuval and Y. Kaspi. The effect of vertical baroclinicity concentration on atmospheric macroturbulence scaling relations. *J Atmos Sci*, 74(5):1651–1667, 2017.